University of Belgrade
Faculty of Physics

Zohra Ali Mohamed Gebrel

Synthesis and Magnetic Properties of Pure and Substituted Yttrium Cuprates and Manganites

Doctoral Dissertation

Belgrade, 2013

Univerzitet u Beogradu
Fizicki Fakultet

Zohra Ali Mohamed Gebrel

Sinteza i magnetne osobine čistih i dopiranih itrijumovih manganita i kuprata

doktorska disertacija

Beograd, 2013

Komisija:

Mentor:

Dr. Jovan Blanuša, viši naucni saradnik Instituta za nuklearne nauke „Vinca“

Univerziteta u Beogradu

Potpis

_____

Clanovi:

Prof. Dr. Zoran Radovic, redovni profesor Fizickog Fakulteta Univerziteta u Beogradu

Potpis

_____

Prof. Dr. Milan Kneževic, redovni profesor Fizickog Fakulteta Univerziteta u Beogradu

Potpis

_____

Dr. Vojislav Spasojevic, naucni savetnik Instituta za nuklearne nauke „Vinca“

Univerziteta u Beogradu

Potpis

_____

Acknowledgments

I would like to express my gratitude to my supervisor, Dr. Jovan Blanusa, whose expertise, understanding, and patience, attention to detail, hard work, added considerably to my graduate experience. I would also like to thank him for his forbearance and understanding during some of the more difficult periods of my lab work. Without whose motivation and encouragement I would not have considered a graduate career in material science.

A very special thanks goes out to the other members of my committee, Dr. Vojislav Spasojevic, and Dr. Vladan Kusigerski for the assistance they provided at all levels of the research project. I would like to thank Dr. Prof. Dr. Zoran Radović from the Faculty of physics for taking time out from his busy schedule to read my thesis.

Finally, I would like to acknowledge my husband who supported me during my time here. Without whose love, encouragement and editing assistance, I would not have finished this thesis. I would also like to thank my mother for the support she provided me through my entire life and in particular.

Izvod

Doktorska disertacija posvećena je proučavanju sinteze, strukture i magnetnih osobina kuprata i manganita itrijuma. Kristalna struktura uzoraka ispitivana je rendgenskom difrakcijom (XRD). Određivanje strukturnih parametara je urađeno pomoćue Ritveldove pune profilne metode uz primenu softverskog paketa FULLPROF. Magnetne osobine ispitivane su merenjem magnetizacije pomoću SQUID magnetometra.

Dve nove, alternativne metode sinteze sagorevanjem, na bazi prekursora dobijenih glicin-nitratnom metodom i samorasprostirućim talasom sagorevanja (SHS), prvi put su uspešno primenjene za sintezu itrijum-kuprata $Y_2Cu_2O_5$ i opisane u ovom radu. Obe metode pokazale su se kao daleko superiornije u odnosu na standardni postupak keramičkog sinterovanja, pri čemu je jedna od njih (SHS) dovela do redukcije ukupnog vremena sinteze sa prosečnih 10 dana sinterovanja na svega 12 sati. Karakterizacija kristalne strukture i magnetih osobina ukazale su na veliki značaj termalnog drifta bakarnih jona, koji se može dovesti u direktnu vezu sa razlikama u ponašanju uzoraka dobijenih različitim termalnim tretmanom. Pokazano je da da se, pored fazne čistoće, i stepen termalnog drifta jona bakra takođe mora uzeti u obzir kao važan dodatni faktor prilikom sinteze itrijum-kuprata.

U okviru ove teze je takođe po prvi put ispitan i uticaj magnetnog razblaženja na nisko-temperaturske osobine $Y_2Cu_2O_5$. Utvrđeno je da delimična zamena bakra magnezijumom dovodi do relativno male ali merljive distorzije dva najvažnija puta izmenskih interakcija, što dalje dovodi do redukcije udela feromagnetne izmene sa povećanjem koncentracije Mg. Znatno veći uticaj supstitucije bakra magnezijumom primećen je u oblasti niskih temperatura gde se, uzrokovan kidanjem beskonačnih i formiranjem konačnih Cu-O lanaca, javlja jak paramagnetni doprinos i snižava Nelova temperatura. Uprkos tome, ukupni rezultati govore u prilog činjenici da se antiferomagnetno uređenje i metamagnetizam održavaju sve do 15% sadržaja Mg.

Drugi deo teze obuhvata ispitivanja vezana za mogućnost primene SHS metode u sintezi nanočestičnog heksagonalnog itrijum-manganita $YMnO_3$, kao i ispitivanje uticaja smanjenja veličine kristalita na njegove magnetne osobine. Menjajući uslove sinteze u dva

odvojena pristupa, dobijeni su uzorci $YMnO_3$ srednje veličine čestica oko 20 nm sa različitim udelom ortorombične faze. Mikrostrukturna, strukturna i magnetna karakterizacija pokazala je da kod svih uzoraka postoji jako izražen uticaj površinskih efekata na njihove magnetne osobine koji se, između ostalog, ogleda i u prisustvu ortorombične faze, čak i u slučaju kada je nije bilo moguće detektovati rendgenskom difrakcijom.

Abstract

This thesis is devoted to the study the synthesis, structure and magnetic properties of yttrium cuprate and yttrium manganite. The structure of the samples was investigated by x-ray diffraction (XRD). Investigation of structural parameters was performed by the Rietveld full-profile analysis method with the application of the FULLPROF software package and the magnetic properties were investigated by magnetization measurement using SQUID magnetometer.

For the first time, two alternative synthesis routes for $Y_2Cu_2O_5$ have been successfully applied, based on precursors obtained by glycine-nitrate and self-propagating high-temperature synthesis (SHS) combustion reactions. Both applied methods proved to be far superior over the standard ceramic sintering, with one of them (SHS) resulting in the reduction of overall synthesis time from 10 days to only 12 hours. The structure and magnetic characterization of obtained samples has shed some new light phenomenon of copper ion drift within the unit cell. It is demonstrated that differences in magnetic behavior can be directly correlated to the variable degree of copper displacement which, besides the phase purity, represents an additional important factor that has to be considered in the course of $Y_2Cu_2O_5$ preparation.

This work also represents the first study of the influence of magnetic dilution on low-temperature magnetic properties of $Y_2Cu_2O_5$. Partial Mg substitution for Cu was found to introduce small but detectable distortions in the two main intradimmer superexchange paths so that ferromagnetic correlations decrease with Mg concentration. More significant impact of Cu substitution was found in the low temperature region due to the breaking of infinite Cu-O chains. The formation of finite size chains introduces significant paramagnetic contribution and reduction in Néel temperature. Despite this, overall results give a strong indication that antiferromagnetic ordering as well as metamagnetism persists up to the 15% of the Mg content.

The second part of the thesis deals with possibilities to apply the SHS combustion in preparation of nanoparticle hexagonal $YMnO_3$, and with the investigation of size reduction influence on its magnetic properties. In two different experimental setups, samples with particle size down to 20 nm were successfully obtained, with the variable

ratio found between hexagonal and orthorhombic phase content. Magnetic properties of all samples are found to be considerably affected by surface effects, showing the small presence of orthorhombic phase even when it is being past undetected by XRD.

Table of contents

Introduction

After 30 years of limited activity, the field of linear magnetoelectrics and multiferroics research has been "revived" from 2000 onwards. Because the topic of multiferroics and magnetoelectrics involves both ferroelectric and magnetic properties of matter, it has attracted researchers from both backgrounds: magnetism and ferroelectricity. The multiferroics can be defined as the class of materials which exhibits two or more "ferroic" order parameters (i.e. ferroelectricity, ferromagnetism, ferroelasticity) simultaneously in a single phase. It is relatively easy to find coexistence of two of these ferroic orderings, but it is more difficult to have a large coupling between two of them [1].

The term multiferroic was introduced relatively late, in 1994 by H. Schmid [2]. In practice, most of the recent research has focused on materials that combine some form of magnetic order (ferromagnetic, antiferromagnetic, non-collinear, etc.) with ferroelectricity. Therefore, the term multiferroics is nowadays often used synonymous with magnetic ferroelectrics. Research on multiferroics (or magnetic ferroelectrics) is also closely related with research on the magneto-electric effect, which is the property that in certain materials a magnetic field induces an electric polarization and, conversely, an electric field induces a magnetization. Traditionally, one distinguishes between linear, quadratic, and higher order magneto-electric effects [3], but more recently the term "magneto-electric effect" is often miss-used to describe any form of cross-correlation between magnetic and (di-)electric properties (for example, when the application of an external magnetic field induces a phase transition between ferroelectric/nonferroelectric phases). It is important to point out, though, that not every magnetic ferroelectric exhibits a linear magneto-electric effect (in the original sense) and that not every material that exhibits a linear magneto-electric effect is also simultaneously multiferroic.

At the moment, a huge interest in multiferroic compounds such as $R_2Cu_2O_5$ and $RMnO_3$ exists. The $R_2Cu_2O_5$ is a matter of research since the beginning of '90-ties, mostly due to its intriguing metamagnetism. Recently, however, direct proofs had appeared in favor of a strong magneto-dielectric coupling, which now puts this material in the group of

multiferroics, the class that is currently in the focus of an enormous scientific interest. This renewed interest in $R_2Cu_2O_5$ as multiferroic material imposes an even bigger significance of quality sample preparation. Thus, there were several important reasons to choose this compound for this study: (1) the combination of a polar space group and magnetic Cu^{2+} ions makes it a potential multiferroic, (2) $Y_2Cu_2O_5$ shows two metamagnetic transitions that are still not investigated completely, emphasizing further analysis of its magnetic properties, and (3) the need for improvement of the preparation technique, due to the high correlation between magnetic properties and crystal structure parameters in $Y_2Cu_2O_5$ and very adverse conditions that must be met during its synthesis.

The hexagonal rare earth manganites with a chemical composition of $REMnO_3$ (RE^{3+} = Lu - Ho, Y) form one group of single-phase multiferroics. They attract a great deal of attention on the technological front due to potential spintronic applications and as four-state memory devices [4], because of their unusual interplay between the ferroelectric and magnetic properties. For their application, however, a better understanding of their fundamental properties is necessary. Recently, considerable experimental progress has been made in understanding the physical properties of hexagonal $YMnO_3$ in various ways. In order to examine the intrinsic magnetic transition of $YMnO_3$, we have developed a preparation technique for fabrication of nanoparticle of $YMnO_3$. The hexagonal $YMnO_3$ with space group $P_{63}cm$ has antiferromagnetic transition temperature at T_N=70 K and, at the same time, ferroelectric transition temperature at T_C =913 K [5-6] .

The objectives of this work are:

1- To apply the novel synthesis routes for the preparation of $Y_2Cu_2O_5$, and to investigate the relationships between its crystal structure and magnetic properties. In order to achieve this objective, we have performed three different methods of $Y_2Cu_2O_5$ synthesis, and investigated the differences in samples behavior related to its structure parameters. The first applied preparation method is solid state reaction, which was the only preparation method reported so far in the literature. This method is relatively easy to implement, but the contamination of Y_2O_3 represents the serious problem and cannot be avoided easily. The two additional synthesis methods applied in this work are representing the first usage of combustion methods in

$Y_2Cu_2O_5$ preparation, and in general, they are the first attempt to synthesize this material with methods other than solid state reaction. The second method concerns the glycine-nitrate process, which is a self- combustion method for powder synthesis. This method is characterized by the use of amino acetic acid (glycine) as a fuel and metal nitrates as an oxidizing agent for rapid rate synthesis. The advantage of this method is a significant reduction of the sintering time, while preserving the high purity of obtained $Y_2Cu_2O_5$ powder. The third method of synthesis applied in this thesis is also combustion method, offering the same advantages as glycine-nitrate, but by itself it represents a new modification of so called self-sustained high temperature synthesis (SHS), which has been modified to give the possibility of obtaining the high purity $Y_2Cu_2O_5$ in a very short time.

2- To investigate effects of magnesium substitution for copper in $Y_2Cu_2O_5$ ceramics by using a self- combustion method for powder synthesis. Low temperature magnetic properties of material substituted by nonmagnetic ion at Cu site were completely unexplored so far. The doped materials are in the form of $Y_2(Cu_{(1-x)}Mg_x)_2O_5$ with x=0.05, 0.1 and 0.15.

3- To synthesize the $YMnO_3$ as nanomaterial by modified self-sustained high temperature synthesis (SHS) method, and to characterize the obtained material from the structural and magnetic points of view. This represents the novel approach to the synthesis of nanoparticle $YMnO_3$, the attempts of which has been intensified during the last two years [7-8].

References

1. S.V. Kiselev, R.P. Ozerov, G.S. Zhdanov, Sov. Phys. Dokl. **7** (1962) 742 -744.
2. Schmid, Ferroelectrics, **162** (1994) 317.
3. Hans Schmid, Int. J. Magnetism **4** (1973) 337.
4. T. Katsufuji, S. Mori, M. Masaki, Y. Moritomo, N. Yamamoto, H. Takagi, Phys. Rev. B **64** (2001) 104419.

5. Bas B. van Aken, Auke Meetsma and Thomas T. M. Palstra, Acta Cryst. **C57** (2001) 230-232.
6. Munoz. A., Alonso. J. A,Martinez-Lope. M. J, Casais. M. T, Martinez. J. L, Fernandez-Diaz. M. T. Phys. Rev.B, **62** (2000) 94-98.
7. Tai-Chun Han, Wei-Lun Hsu, Wei-Da Lee, Nanoscale Research Letters, Vol 6, (2011), 201.
8. M.F. Zhang, J. M, Liu, Z. G. Liu, Qppl. phys. A, **79** (2004) 1753-1756.

1. Multiferroic materials

Multiferroic materials can be considered as being materials presenting at least three ferroic states. These ferroic states are ferroelasticity, ferroelectricity and ferromagnetism. Thus, as a logical definition to the term multiferroic, we could use the term multiferroic to any material presenting two of these three properties. However, the most interesting combination was thought to be materials presenting simultaneously ferroelectricity and ferromagnetism.

Mutual control of magnetism and electricity was first postulated by Pierre Curie in 1894 [1]. More than half a century later in 1959, the same concept was predicted theoretically by Dzyaloshinskii [2]. The first observation of such a phenomenon is the so-called linear magnetoelectric effect found in chromium oxide (Cr_2O_3) by Astrov in 1960.[2, 3] Since any dielectric quantity is symmetric and any magnetic quantity is antisymmetric under time reversal symmetry (*T*), the linear magnetoelectric effect only occurs in systems that break time reversal symmetry,for example, by a magnetic ordering. The search for multiferroics was very active in the 1960s and 1970s and several compounds have been found such as $BiMnO_3$, $BiFeO_3$, $YMnO_3$, $Pb(Fe_{2/3},W_{1/3})O_3$, $Pb(Fe_{1/2},Ta_{1/2})O_3$ and $Ni_3B_2O_{13}I$, but the search then declined, in large part because single-phase materials with both properties could not be widely produced and because of rather weak magnetoelectric coupling [4].

Also, a few others reported the magnetoelectric effect in the 70's [5-6]. In later years magnetoelectric materials received much less attention, probably due to the lack large responses of such materials in nature. Magnetoelectric coupling is closely related to "multiferroism". In 1994 the term multiferroics was coined by Schmid [7]. Almost four decades later, a renaissance began in the field of multiferroics due to the discovery of the magneto-electric effect in rare earth doped manganites and seminal paper on multiferroics by Nicola. A. Spaldin [8]. Figuer 1.1 schematically represents a relationship between multiferroic magnetoelectric materials.

Attention has recently been focused on a new class of multiferroics that exhibit magnetic frustration; examples include hexagonal $RMnO_3$, $CoCr_2O_4$ spinel, the Kagom´e staircase compound $Ni_3V_2O_8$, RMn_2O_5 and perovskite $RMnO_3$ (R=Tb,Dy,Y). In this class of materials the ferroelectricity is directly induced by the spin structure [9-10-11].

The hexagonal manganites $RMnO_3$ are one such rare example of the multiferroic materials with the coexistence of both ferroelectric and antiferromagnetic transitions. For example, $ErMnO_3$ shows an antiferromagnetic transition at T_N =77 K and a ferroelectric transition at T_C =588 K [12]. Therefore, the hexagonal manganites offer a unique window of opportunities of exploring a possible coupling between the two order parameters. In fact, these hexagonal manganites have been extensively investigated over the past few years and are the first real examples of multiferroic materials with a convincing demonstration of such a desirable coupling between ferroelectricity and magnetism [12-13]

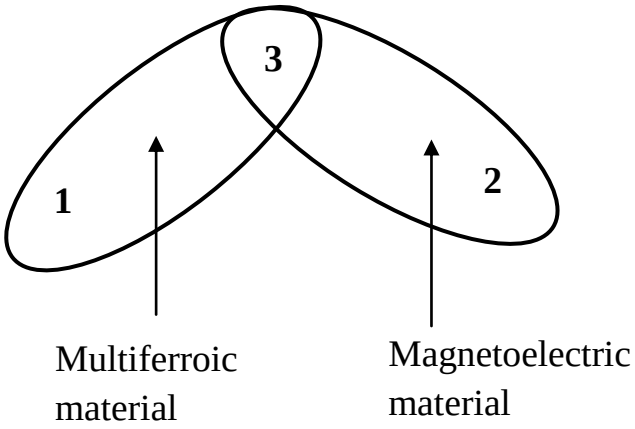

Figure 1.1: Relationship between multiferroic and linear magnetoelectric material Multiferroic materials (area 1) and (area 2) linear magnetoelectric materials, may overlap giving rise to an enhancement to the interplay between dielectric and magnetic properties (area 3)

There has been renewed interest in studying the perovskite-based multiferroic materials, such as rare earth manganites $TbMn_2O_5$, $YMnO_3$, $BiMnO_3$, $HoMnO_3$ etc., which have been shown to display large magnetoelectric effects. Although ferromagnetic multiferroics are preferred for applications, most of the multiferroics under investigation

are antiferromagnets such as $YMnO_3$ and $Y_2Cu_2O_5$. This is because very few ferromagnets are good insulators, an important requirement for ferroelectricity.

1.1 Application of multiferroics

Multiferroic materials have been the subject of intense study due to their potential applications in information storage process, spintronics, multiple-state memories, magnetoelectric sensors, etc. [14]. They are of remarkable importance because of their unique and strong coupling of electric and magnetic properties, giving rise to the simultaneous presence of more than one ferroic property. the *Functional* electronic and magnetic materials form an important part of modern technology. *For example*, ferroelectrics (materials with a spontaneous electric polarization that can be switched by an applied electric field) are widely used as tunable capacitors and form the basis of ferroelectric random access memory (Fe-RAM) for computers. On the other hand, the materials most widely used for recording and storing data, such as in the hard drive, are ferromagnetic (materials with a spontaneous magnetic polarization that can be reversed by a magnetic field). Multiferroic materials are interesting not only because they exhibit ferroelectric and magnetic properties but also due to the "magnetoelectric effect", by which an induced electrical polarization and magnetization can be controlled by applying a magnetic and electric field, respectively. This effect can potentially be exploited to allow the construction of novel spintronic devices such as tunneling magnetoresistance (TMR) sensors, spin valves with functionality that is tunable by an electric field [1], and multi-state memories in which data are written electrically and read magnetically [13]. However, in order to be useful for applications, the magnetoelectric coupling must be both large and active at room temperature.

In this chapter, we will mainly concentrate on the two of families of multiferroic compounds: the orthorhombic polar $R_2Cu_2O_5$ materials, which exhibit complex magnetic phase diagrams (metamagnetism), and the multiferroic hexagonal manganites.

1.2. $R_2Cu_2O_5$ compounds

The cupric oxides have been one of the most attractive and interesting subjects in physics since the discovery of high-temperature superconductivity in $RBa_2Cu_3O_7$ compounds (where R is a rare earth element). There has been also greatly increased interest in non-superconducting copper oxides [15-16-17]. Amongst these, $Y_2Cu_2O_5$ and its derivatives ($R_2Cu_2O_5$ with *R* = Sc, In, Tb, Lu and other rare earth elements) are especially interesting.

So far, three group of rear-earth copper oxides have been synthesized: R_2CuO_4 (R=La, Pr,Gd), $RCuO_3$ (R= La, Y) and $R_2Cu_2O_5$ (R=Tb, In, Sc,Y). The first group (R_2CuO_4) belongs to semiconductors, and become superconducting when the part of R^{+3} is substituted by Sr^{+2} or Ba^{+2}. Much effort has been concentrated on study of their magnetism [18]. The second group, $RCuO_3$, can be synthesized only under high pressure and high temperature [19]. The behavior of the third group ($R_2Cu_2O_5$) exhibits one of the most interesting effects exclusively found in this family of cuprates – metamagnetism. Namely, under sufficiently high external magnetic field they present striking anomalies indicating complex metamagnetic transition: one for In, Lu, Er, Ho and Dy, and two for Y and Sc and four for Yb [15, 17, 20]. The nature of these field-induced changes in the magnetic ordering remained unknown, as well as the magnetic ordering itself [15].

Although $Y_2Cu_2O_5$ shares some elements of the crystal structure with high-T_C $YBa_2Cu_3O_x$ superconductors (Cu-O chains), it was found to be a semiconductor material with high electrical resistivity, without superconducting properties [17]. Being the one of the most important contaminants during the preparation of the mentioned 123-type high-Tc superconductors, there was a natural interest to understand magnetic properties of this compound in order to evaluate the magnetic interactions in the related 90 K superconductors. However, after discovering metamagnetism in $Y_2Cu_2O_5$, the material itself has become the subject of considerable research interest worldwide during 1990's. The revived interest in $Y_2Cu_2O_5$ took place recently, after it was realized that the polarity of the space group Pna*21* could enable spontaneous polarization and, therefore, offers potentials for multifferoicity and magneto-dielectric coupling. The strong magneto-dielectric coupling in $Y_2Cu_2O_5$ was eventually proved recently [21].

All $R_2Cu_2O_5$ compounds are antiferromagnetically ordered at low temperatures with T_N ranging from 11K (Dy) to 30K (In). Most of them exhibit metamagnetic behavior below the Neel temperature [15, 20, 22] (Table 1).

Table 1.1. Magnetic properties of $R_2Cu_2O_5$ single crystals [13]:

R	***T_N(K)***	***Hc (T) at 4.5 K***	***Easy direction***
Y	11.5	2.4 and 4.6	b-axis
Tb	5.5 and 18,8		b-axis
Er	27	1.2	b-axis
Tm	17	0.05	$\perp$ b-axis
Yb	8.2 and 16	2.8	b-axis
Lu	19	4.1	b-axis

1.2.1. Crystal structure of $Y_2Cu_2O_5$

The crystal structure of $Y_2Cu_2O_5$ has been studied by means of x-ray diffraction [23, 24], powder neutron diffraction [25], and in 1995 Garcia et al studied the structural characterization of $R_2Cu_2O_5$ (R=Yb, Tm, Er, Y and Ho) oxides by netron diffraction [26] . It has been confirmed by several groups that the crystal structure of $Y_2Cu_2O_5$ is isostructural with $Ho_2Cu_2O_5$ [23, 27]. $Y_2Cu_2O_5$ compound crystallize in the polar orthorhombic space group P*n*a2_1 with cell parameters a= 10.814Å,b= 3.5000 c=12.480 Å, and Å [25-27]. The family of $R_2Cu_2O_5$ compounds includes those with rare-earth R^{3+} cations smaller then Gd, i.e. Tb, Dy, Ho, Y, Er, Tm, Yb, as well as with Lu, In, and Sc which all crystallize in the orthorhombic structure with P*n*a2_1 space group symmetry [25-27]. The most characteristic feature of the $Y_2Cu_2O_5$ crystallographic structure is the occurrence of zigzag copper chains along the a-axis (Figure 1.2). There are 2 non-equivalent crystallographic sites for both Cu and Y ions in the unit cell, with very similar oxygen coordination. There is a distorted square planar arrangement of four oxygen atoms ions within a distance of 1.9 Å around copper atoms, with the fifth oxygen atom at a distance of 2.7 Å forming a sort of a pyramid. The copper ions in two positions (Figure 1.2,

right) are coupled to form dimmers, which in turn form Cu_2O_5 zigzag chains along ***a***-axis. The Cu ions in adjacent chains are also connected along the b axis to form ab pseudoplanes. These pseudo–planes are separated by the Y ions, which have distorted octahedral oxygen coordination [23-27].

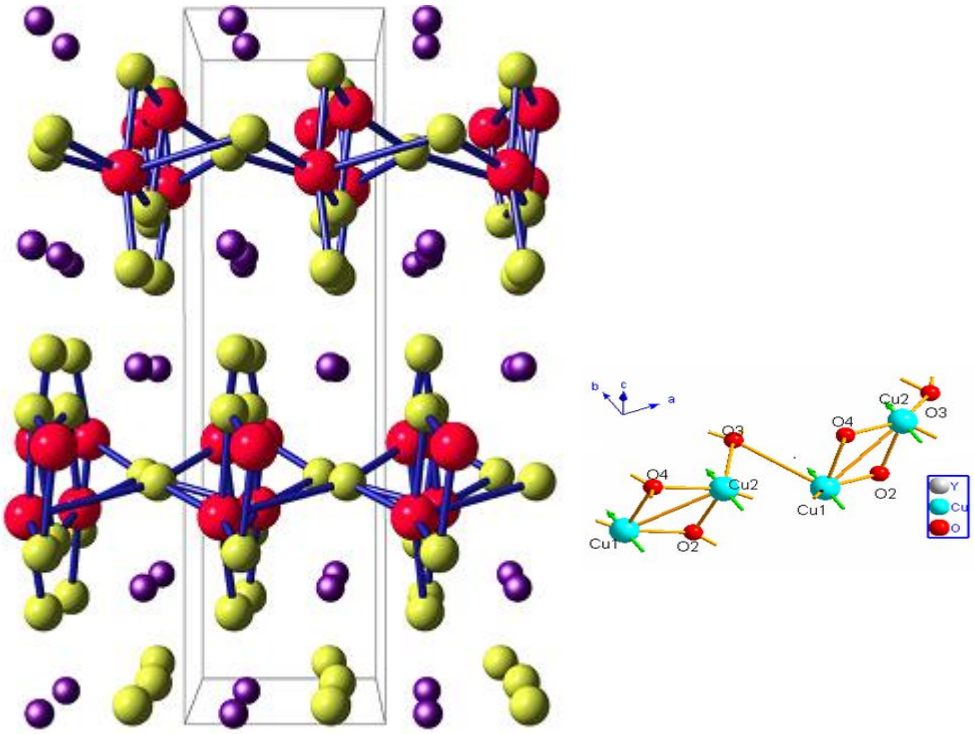

Figure 1.2. The crystal structure of $Y_2Cu_2O_5$ viewed along a-axis. Two horizontal CuO ***ab***-planes are visible. Six copper (red) chains are seen head-on. The rare earth ions (blue) are situated between CuO planes.

1.2.2. Magnetic properties of $Y_2Cu_2O_5$

The magnetic properties of $Y_2Cu_2O_5$ were first studied and discussed by Tro´c et al. [28] using powdered samples. This work was followed by Cheong et al. [17], who used needle-like single crystals. Additional powder studies on $Y_2Cu_2O_5$ and other $R_2Cu_2O_5$ have been made by several other groups [15, 20]. These investigations showed that $Y_2Cu_2O_5$ orders antiferromagnetically at T_N = 13 K although the specific heat indicates a peak at 10.5 K [17, 29]. The investigations also showed that the b-axis of the orthorhombic crystal structure is the spin easy axis and that the ferromagnetic Curie-Weiss temperature is 38.5 K

[15, 17] which suggests that there are strong ferromagnetic interactions in this compound. The effective paramagnetic moments are about 2.16 μ_B and 1.98 μ_B (Bohr magnetons) for applied magnetic fields parallel and perpendicular to the b-axis, respectively. Under very week external magnetic field $Y_2Cu_2O_5$ exhibit a second magnetic transition at about 6 K. According to the work presented in 1994 by R.Horyn et al [30], the 6 K anomaly is also sensitive to hydrogen introduced into structure. The intensity of 6 K anomaly exhibits a strong dependence on temperature and sintering time.

R.Horyn et al. [30] have also offered an explanation for the 6 K anomaly appearance by investigating the sensitivity of the anomaly to time- and temperature-dependent heat treatment, where they placed a hypothesis on the possibility of a thermally activated displacement of Cu^{+2} ions leading to a creation of the new Cu-O coordination polyhedron - trigonal bipyramid. X-ray analysis of powder samples has revealed that the crystal structure of $Y_2Cu_2O_5$ can accept two different coordination polyhedra for Cu^{+2} ions, for which selective occupation of any of them have only minor influence on diffraction pattern, thus occurring hardly distinguishable through X-ray powder diffraction. Mutual interaction of Cu^{2+}-ions, occupying both polyhedra, is the most probable reason for the 6 K anomaly to occur [30].

The most striking phenomenon in $Y_2Cu_2O_5$ is that a metamagnetic transition occurs when a magnetic field is applied parallel to the b-axis. This phenomenon was first observed by Cheong et al. [17] in applied fields up to 5 T. At 4.2 K, a metamagnetic transition with an induced moment equal to 1/3 of the saturation moment occurs at the field of 2.84 T (Bc$_1$). The induced moment remains constant until Bc$_2$ = 4.71 T where the magnetisation increases again at and continues to increase linearly until the saturation moment B_S = 7.3 T is reached. Other members of the family, except for R = Tb and Tm, have various numbers of metamagnetic transitions; the highest number of transitions (five transitions below 12 T) is found in $Yb_2Cu_2O_5$ [15]. However, due to the lack of large single crystals and the high critical fields, neutron diffraction studies to determine the magnetic structures of the field induced phases have been carried out only for $Y_2Cu_2O_5$ [31].

Magnetic properties of other members of $R_2Cu_2O_5$ family are interesting as well. For example, the magnetic studies of $Tb_2Cu_2O_5$ have been presented in Refs. [32–33]. The

magnetic susceptibility of this compound containing two magnetic ions follows the Curie–Weiss law with a negative value of Curie–Weiss temperature Θ = –10 K. Transition to the antiferromagnetic phase was reported to take place in the 17–21.5 K temperature range. An additional anomaly of magnetic susceptibility was observed in the 5–8 K range. In 1996 Popova et al [34] investigated the magnetic properties of $In_2Cu_2O_5$ and $Sc_2Cu_2O_5$ that crystallize in the *Pna*$_{21}$ space group were studied by means of high resolution Fourier transform spectroscopy of the rare earth probe. Magnetic ordering in $In_2Cu_2O_5$ at 29 K and in $Sc_2Cu_2O_5$ at 16 K has been confirmed by this method. The most probable magnetic structure in an ordered state of $In_2Cu_2O_5$ is suggested to be the same as in $R_2Cu_2O_5$ with R = Y, Lu, Er, Tb. Namely, ferromagnetically ordered **ab** planes coupled antiferromagnetically with copper magnetic moments aligned along the crystal ***b***-axis [34]. The magnetic properties of the $Dy_2Cu_2O_5$ compound have been also investigated previously [15, 35]. Its susceptibility follows the Curie–Weiss law almost exactly down to the transition temperature T_N = 11 K, with a negative value of the Curie–Weiss temperature Θ = –18 K (antiferromagnetic interaction) [35]. Very similar behavior was found for $Er_2Cu_2O_5$ [15,35], for which the susceptibility follows the Curie–Weiss law exactly down to the transition temperature of T_N = 27K, with a negative value of the Curie–Weiss temperature Θ = −4 K [35].

1.2.3. Effects of substitutions in $Y_2Cu_2O_5$

There is only few studies made so far on the influence of Y ions replacement in yttrium cuprate by other transition metals or alkaline. Compositional series of solid solutions of $(Y_{1-x}R_x)_2Cu_2O_5$ -type, where R rare earth ions, have been the subject study of only a few papers [36 - 44]. The structure and magnetic properties of $(In_xY_{1-x})_2Cu_2O_5$ compounds were reported in the temperature range between 77 K and room temperature [39]. The influence of the substitution of Y by In on the structure and magnetic property of $Y_2Cu_2O_5$ were studied in 1994 by Qiang Su et al. They have found that In and Y can be substituted by each other in any ratio to make new compounds $Y_{2-x}In_xCu_2O_5$ ($0 \leq x \leq 2$). The XRD analysis revealed that the $Y_{2-x}In_xCu_2O_5$ keeps the orthorhombic structure but the space group has been changed. The lattice parameters do not change linearly with the

change of In^{3+} concentration, so Vegards's law is not obeyed. The magnetic susceptibilities for various In^{3+} concentration show similar behavior they obey Curie-Weiss' law above 160K and 180K, with θ (Weiss constant) ranging between 38 K and 45 K. The effective magnetic moments μ_{eff} were found to decrease with the increase of the concentration of In^{+3} in Y_{2-x} $In_2Cu_2O_5$ [39]. In 1995 Horyn et al. have studied the magnetic properties of $Y_2Cu_2O_5$ and $Y_{2-x}Gd_xCu_2O_5$ with x=0.6. The antifferomagnetic transitions in $Y_2Cu_2O_5$ and $Y_{2-x}Gd_xCu_2O_5$ were found at 12.8 K and 6 K, respectively [43].

Within samples with $(Ca_xY_{1-x})_2Cu_2O_5$ composition, where x = 0.05, 0.1 and 0.2, a phase with incommensurate modulated structure has been found [44]. That phase becomes the main phase within the $(Ca_{0.2}Y_{0.8})_2Cu_2O_5$ sample. In another report [38], solid solutions $(Tb_xY_{1-x})_2Cu_2O_5$ were successfully synthesized within the whole range of the terbium concentrations $0 < x < 1$ by the solid-state reaction. It was found that the substitution of large ion (Tb^{+3}) for a smaller (Y^{+3}) makes the structure less stable and lowers the decomposition temperature. In 2007, Typek [37] studied the competing magnetic interactions in $(Dy_{0.375}Y_{0.625})_2Cu_2O_5$, showing that $(Dy_{0.375}Y_{0.625})_2Cu_2O_5$ is antiferromagnetic below T_N=11 K and displays many signs of low dimensional magnetism. Thermogravimetry and (EPR) at room temperature had been used to study $(Er_xY_{1-x})_2Cu_2O_5$. In 2007 Typek reported that all Copper spin dynamics in $(Er_{0.5}Y_{0.5})_2Cu_2O_5$ solid solution has been investigated by electron paramagnetic resonance (EPR) technique. The temperature dependence of the EPR integrated intensity of the resonance line has showed a pronounced maximum at temperature and has vanished at the transition to the antiferromagnetic ordering at T_N=11 K. The temperature at which the EPR integrated intensity reaches maximum was different for the heating and cooling runs. Clear maximum of χ_{EPR} is observed during the cooling run at 38 K. The appearance of maximum of the integrated intensity at temperature different than T_N is a clear manifestation of a low dimensional magnetic system. The sample was cooled down below T_N, where the EPR signal was reduced to zero and further was heated up. This time the EPR signal started to grow in intensity with the temperature increase, but anyway it was significantly weaker than during the cooling run [40, 41].

1.3. Multiferroic rare earth manganites $RMnO_3$

Multiferroic manganites of the type $RMnO_3$ (R=rare-earth) have attracted a great deal of attention due to two main reasons: First, on the technological front multiferroics are promising materials for potential spintronic applications such as four-state memory devices [14]. For their application, however, a better understanding of their fundamental properties is necessary. Second, these materials belong to a class of complex oxides with various coupled ordering phenomena and rich phase diagrams [9].

These materials simultaneously exhibit ferroelectricity and antiferromagentic ordering of magnetic Mn ions. Generally, when prepared under ambient pressure, the rare-earth manganese oxides crystallize with crystal structures depending on the size of the *R* constituent. Rear-earth ionic (RE = Ho, Er, Tm, Yb, Lu, Y and Sc) which have small ionic radii *r* ($r_{R3+} < r_{Dy}$), crystallize in the hexagonal structure (space group: $P_{63}cm$) while manganites formed by (RE = La, Ce, Pr, Nd, Sm, Eu, Gd, Tb or Dy) , which have larger ionic radii ($r_{R3+} \geq r_{Dy}$) are orthorhombic with (space group Pnma) [45-46]. However, the orthorhombic perovskite structure can also be obtained for the small rare-earths by heating the corresponding hexagonal compounds under high pressure Rare-earth manganites of the perovskite-type structure $RMnO_3$ were discovered in the 1950s [47]. Many studies have been done on perovskite $RMnO_3$ because of their unusual properties, such as colossal magneto-resistance and charge ordering phenomena when hole doped by partially replacing R^{+3} by A^{+2} cations (R= Ca, Sr, Br) [48]. On the other hand, for the small rare-earth ions as Ho, Er, Tm, Yb, Lu, and Y, $RMnO_3$ crystallizes in hexagonal structure [46].

Hexagonal $RMnO_3$ has recently attracted a lot of interest because of the coexistence of ferroelectricity and antiferromagnetism. Such “multiferroic” materials in which ferroelectricity and ferromagnetism coexist are of interest with respect to the coupling between the ferroelectricity and ferromagnetism and their possible control [9].

1.3.1. Hexagonal $RMnO_3$ manganites

In the hexagonal phase of $RMnO_3$, each Mn ion is surrounded by three in-plane and two apical oxygen ions forming a MnO_5 trigonal bipyramid as showing in Figure (1). These MnO_5 blocks are two dimensionally connected with each other on their corners separated by a layer of R^{3+} ion [9, 50]. The MnO_5 bipyramids are corner linked to form a triangular lattice layer in the ab plane. In the ferroelectric phase, hexagonal $RMnO_3$ has a non-centrosymmetric $P6_3cm$ structure and the ferroelectric polarization appears along the c axis [45, 50]. The ferroelectric polarization originates from the tilting of MnO_5 trigonal

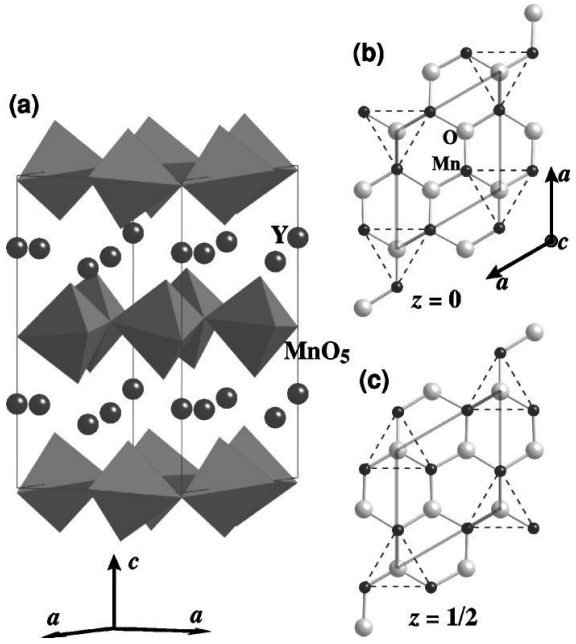

Figure 1.3. (a) Schematic representation of the crystal structure of hexagonal $YMnO_3$ and a representation of the MnO (ab) plane at (b) z=0 and (c) z=1/2. Black and gray spheres represent Mn and O, respectively. The rhombuses and the dotted triangles show the unit cell and the formation of Mn trimers, respectively [11]

bipyramids and the buckling of R layers [50].The tilting of the MnO_5 bipyramids also makes the triangular lattice weakly trimerized. As to the magnetic aspects, the Mn^{+3} spins align into an antiferromagnetic 120^0 structure due to geometric frustration in the triangular-lattice layers at low temperatures below T_N.

The hexagonal manganite YMnO3 is representative of $REMnO_3$ multiferroic materials exhibiting magnetic properties simultaneously. Hexagonal $YMnO_3$ crystallize in space group P_63cm with lattice parameters a=6.125 Å and c=11.41 Å. In $YMnO_3$, magnetic ordering within the manganese partial structure is switched on below the Neel temperature T_N=75 K [50, 51], and coexists with the ferroelectric ordering. The magnetic ordering is dominated by antiferromagnetic intralayer Mn-O-Mn superexchange interactions. Weaker interlayer interactions Mn-O-O-Mn guarantee long range magnetic order. On account of the anisotropy, the magnetic dipoles are oriented parallel to the ab plane with a so-called 120 structure. This structure is typical for frustrated magnetic system of classical spins and is a consequence of the triangular network [51]. The orientation of the Mn spins with respect to the crystal axes a and b occurs according to the pattern a shown in Figure 1.3 (b,c).[51] In this projection neighboring spins on line of layer b (z=0) and layer c (z=1/2) are parallel and coplanar. On the basis of these results (electric dipole moment parallel to the c axis and magnetic dipoles perpendicular to the c axis) in one case it is ferromagnetic and in the other case antiferromagnetic, for which the moments alternate in sign from the z=0 to the z=1/2 layer [50-51].

All $RMnO_3$ compounds exhibit antiferromagnetic ordering with the paraelectric-antifferroelectric transition temperatures ranging from 70K to 140 K [50- 52]. For the hexagonal non-perovskite manganites $RMnO_3$ (*R*=Ho, Tm, Lu, and Y), the ferroelectric Curie temperatures well above room temperature (T_C =600-990 K) [50]. With saturated polarization > 5.6 $\mu C/cm^2$ and the Néel temperatures in the range 73– 124 K are reported [53-57]. To the contrary, the orthorhombic manganites have the ferroelectric Curie temperature lower than the Néel temperature and very low remnant polarization (<0.2 $\mu C/cm^2$). The existence of ferroelectricity in these orthorhombic compounds was attributed to lattice modulation accompanied by the antiferromagnetic order. Systems belonging to the hexagonal class undergo a ferroelectric transition far above the ordering of the Mn^{3+} spins. Such magnetic ordering occurs in both structures; however, ferroelectricity is possible only for the hexagonal phase which has the non-centrosymmetric phase group $P6_3cm$. Although hexagonal manganites have been studied for many years [6], very recently there has been a resurgence of interest in these materials [52-58]. Most hexagonal $REMnO_3$ compounds can

exhibit two transitions, i.e., a very high-temperature (T_{FE} ≈ 900 K) ferroelectric distortion and a low-temperature (≈100 K) magnetic ordering. The development of two order parameters is a rarity in oxides [53-58].

Table 2.2: Lattice parameters and magnetic ordering temperatures of hexagonal RMnO3

	a (Å)	c(Å)	T_N (K)	Reference
$InMnO_3$	5.869	11.47	120	[53]
$ScMnO_3$	5.833	11.17	130	[54,55]
$YMnO_3$	6.148	11.44	72	[55,56]
$DyMnO_3$	6.182	11.45	57	[57]
$HoMnO_3$	6.142	11.42	76	[58,54]
$ErMnO_3$	6.112	11.40	79-81	[58,54]
$TmMnO_3$	6.092	11.37	84-86	[58]
$YbMnO_3$	6.062	11.36	87-89	[57-58]
$LuMnO_3$	6.046	11.41	90	[55,56]

1.3.2. Orthorhombic $RMnO_3$ manganites

The structure of orthorhombic *R*MnO_3 compounds can be considered as an orthorhombically distorted cubic perovskite structure. The distortion from the ideal cubic structure arises from two sources [59, 60]. The first is the mismatch of the *R*-O and Mn-O equilibrium bond lengths which is adjusted by cooperative rotation of the MnO_6 octahedra. The rotation increases with decreasing *R* ion radius. The second reason for the lattice distortion is a deformation of the MnO_6 octahedra due to the orbital ordering characteristic of the Jahn-Teller effect of Mn^{3+} cations [61]. The degree of orbital ordering slightly increases from La to Tb and then remains almost unchanged for the last terms of the series. Details of orbital and magnetic ordering in a series of orthorhombic *R*MnO_3 compounds have been studied by Tachibana et al.[59] and Kimura et al.[61] as a function of the *R* ionic radius. For materials with orthorhombic structure, the ground state of undoped $RMnO_3$ is of long-range antiferromagnetic (AFM) order. When doped, the compound has a rich phase diagram resulting from the interplay among spin, charge, and orbital degrees of freedom. In the case of concentration of A in the regime $0.22<x<0.5$, it becomes ferromagnetic (FM)

through the double-exchange process. On the other hand, one can also make materials that have spin glass (SG) as the low temperature ground state due to the competition between the FM double-exchange interaction and the AFM superexchange interaction. In the $RMnO_3$ perovskite structure, the Mn^{3+} d^4 levels are split by the oxygen octahedral crystal field into a lower-energy t_{2g} triplet and a higher-energy eg doublet, which are filled according to Hund's rules giving rise to the electron configuration $t^3_{2g}e^1$ g. The Jahn–Teller character of the Mn^{3+} cations lies at the origin of the strong distortion of the MnO_6 octahedra and it leads to an orbital ordering in the *a–c* plane (space group *Pnma*). This Jahn– Teller distortion is present for all the $RMnO_3$ compounds; the distortion slightly increases from La to Tb and remains nearly unchanged for Ho, Er and Y [59, 61].

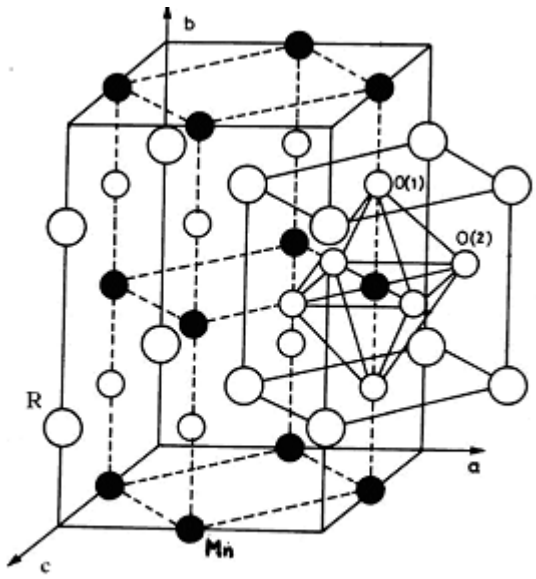

Figure 1.4 : Orthorhombic structure of $RMnO_3$

$YMnO_3$ is the most experimentally studied member of the hexagonal $RMnO_3$ group. It has also been the main subject of theoretical first-principles studies of the fundamental physical properties the $RMnO_3$ compounds, since the empty 4f shell of the Y^{3+} ion makes $YMnO_3$ a convenient system for application of the pseudo potential-based methods. In addition to being fundamentally important, $YMnO_3$ has attracted a good deal of interest as a

multiferroic material for applications in magnetic storage media and spintronics, since the electrical and magnetic orders in $YMnO_3$ were shown to be coupled. The coupling was found to originate from an interaction between magnetic and electric domain walls.

References

1. P. Curie, J. Phys., 3(Ser. III) (1894) 393–415.
2. Dzyaloshinskii I. E., Sov. Phys. JETP, 10 (1960) 628.
3. D. N. Astrov. Zh.Exp. Teor. Phys. JETP, 11 (1960) 708–709.
4. B. B. Van Aken, T. T. M. Palstra, A. Filippetti, and N. A. Spaldin, Nature Materials, 3 (2000) 164.
5. Hans Schmid, Int. J. Magnetism, 4 (1973) 337-361.
6. G. A. Smolenskii, I. E. Chupis, Ferroelectromagnets. Usp. Fiz. Nauk, 137 (1982) 415–448.
7. L. Schmid, Ferroelectrics, 162 (1994) p.317.
8. N. A. Hill, J. Phys. Chem. B, 104 (2000) 6694-6709.
9. Bernd Lorenz, Review Article, Condensed Matter Physics, (2013) , Article Id 497073, 43pages.
10. B. Fu, Wayne Huebner, Mladen F, Trubelja and Vladimir S Stubican, J.Mater. Res, 9(10) (1994) 2645-2653.
11. Jyoti Ranjan Sahu, Anirban Ghosh, A. Sundaresan, C.N.R. Rao, Materials Research Bulletin 44 (2009) 2123–2126.
12. J. Park, U. Kong, s. I. Choi, J. G. Park, C. Lee, W. Jo. Appl.Phys. A, 74 (2000) 5802-5804.
13. C. Ederer, N.A. Spaldin, Phys. Rev. B, 71 (2005) 060401.
14. W. Eerenstein, N. D. Mathur, and J. F. Scott, Nature 442 (2006) p.759.
15. J.L. Garica-Munoz and X. Obradors, Physical Review B, 51 (1995) 6594-6601.
16. Wen-Jye Jang, Masashi Hasegawa, Tong Rong Zhao, Humihiko Takei, Masafumi Tamura, Minoru Kinoshita. Journal of Crystal Growth, 141 (1994) 153-158.
17. S-W. Cheong, J. D. Thompson, Z. Fisk, K. A. Kubat-Martin, and E. Garcia, Physical Review B, 38(10) (1988) 7013-7015.

18. Baba-Kishi K. Z., Camps R. A. and Thomas P. A., J. Phys.: Condens. Matter, 2 **(**1990) 5085.
19. M. Atjomand , D.J. Machin, J. Chem. Soc. Dalton (1975), 1061-1066.
20. H. Ushiroyama, K. Kita, S. Kimura, H. Ohta, M. Motokawa, Physica B, 201 (1994) 95-98.
21. U. Adem, G. Nenert, Arramel, N. Mufti, G.R. Blake, and T.T.M. Palstra, Eur. Phys. J. B, 71 (2009) 393-399.
22. R. Troc, J. Klamut, Z. Bukowski,R, Horyn, J. Stepien-Damm, Physica B, 154 (1989) p.189.
23. Kimizuka N, Takayama E and Horiuchi S, J. Solid State Chem., 42 (1982) 322–324.
24. Lambert U and Eysel W, Powder Diffraction, 1 (1986) 45–50.
25. Fjellvag H, Karen P and Kjekshus A Acta Chem. Scand. A, 42 (1988) 144–147.
26. J. L. Garcia- Munoz and J. Rodrguez-Carvajal, Journal of Solid State Chemistry, 115 (1995) 324-331.
27. R. Famery, F. Queyroux, Mater. Res. Bull., 24 (1989) 275–281.
28. R. Tro´c, Z. Bukowski, R. Hory´n and J. Klamut, Phys. Lett. A, 125 (1987) 22.
29. V. V. Moshchalkov, N. A. Samarin, I. O. Grishcnenko, B. V. Mill and Y. Zoubkova, J.Magn. Magn. Mater., 90-91 (1990) p.553.
30. R. Horyn, J. Klamut, M.Wolcyrz. A. Wojakowski, A.J. Zaleski, Physica B, 205 (1995) 51-58.
31. M. Motokawa, K. Kita, H. Shibazaki, H. Ohta, W. J. Jang, M. Hasegawa, H. Takei, Physica B, 211 (1995) 165-167.
32. Moshchalkov V.V, Samarin N.A, Grishchenko I.O, J. Magn. Magn. Mater., 90–91 (1990), p.533.
33. Aride J, Flandrois S, Taibi m, Boukhari A, Drillon M, soubeyroux l. J, Solid State Commun., 72 (1989) p.459.
34. M.N. Popova, S.A. KIimin, R. Trocb and Z. Bukowski, Solid State Communications, 102(1) (1997) 71-75.
35. R. Troc, J. Klamut, Z. Bukowski, R. Hory´n and J. Stepien-Damm, Physica B, 154 (1989) p.189.

36. J. Typek and N. Guskos, Rev. Adv. Mater. Sci., 12 (2006) 106-111.
37. J. Typek, Phys. Stat. Sol., 244 (2007) 1102-1108.
38. J. Typek, J. Kostrzewa, N. Guskos, Materails Science-Poland, 23(4) (2005) 929-938.
39. Qiang Su, Xueqiang Cao and Hongyan Wang, Journal of solid state Chemistry, 111 (1994) 310-314.
40. J. Typek and N. Guskos, Material Science, Poland, 24(4) (2006) 901-912.
41. J. Typek, Journal of Alloys and compounds, 440 (2007) 26-29.
42. Qiang Su, Xueqiang Cao and Hongyan Wang, J. Mater. Chem., 4(3) (1994) 417-420.
43. Horyn, J. Klamut, M. Wotcyrz, A. Wojakowski, A.J. Zaleski. J. Magnetism and Magnetic Materials 140-144 (1995) 1575-1576.
44. Fenng. C. N, Lovett. D R, J.Phys.: Condens. Matter, 10 (1998) 3497-3507.
45. Abalgasim Alqat, Zohra Gebrel, Vladan Kusigerski, Vojislav Spasojevic, Marian Mihalik, Mutus Mihalik, Jovan Blanusa, Ceramic International, 39 (2013) 3183-3188.
46. Gilleo M A, Acta Crystallogr., 10 (1957) p.161.
47. Yakel H, Koehler W. C, Bertaut E. F and Forrat .F Acta Crystallogr., 16 (1963) p.957.
48. Munoz. A, J. A. Alonso, M. T. Casais, M. J. Martinez Lope, and M. T. Fernadez Dia, J. Phys: Condens. Matter, 14 (2002) 3285-3294.
49. Kusters R. M, Singleton J, Keen D. A, McGreevy. R and Hayes .W, Physica B, 155 (1989) 362.
50. Zhou J. S., Goodenough J. B., Gallardo-Amores J. M., Moran E., Alario-Franco M. A., Caudillo R., Phys. Rev. B 74 (2006) 014422, 7 pages.
51. J. P. Rivera, Eur. Phys. J. B., Vol 71, (2009) 299-313.
52. W. C. Koehler, H. L. Yakel, E. O. Wollan, and J. W. Cable. Physics Letters, 9 (1964) p.93.
53. J.E.Greedan,M. Bieringer, J. F. Britten, D.M. Giaquinta, andH. C. zur Loye, J. Solid State Chem., 116 (1995) 118–130.

54. W. C. Koehler, H. L. Yakel, E.O.Wollan, and J.W. Cable, Phys. Lett., 9 (1964) 93–95.
55. D. G. Tomuta, S. Ramakrishnan, G. J. Niewenhuys, and J. A. Mydosh, , J. Phys., Vol 13, No 20, (2001), 4543–4552.
56. T. Katsufuji, M. Masaki, A. Machida, Phys. Rev. B, 66 (2002) 341–348.
57. N. Kamegashira, H. Satoh, and S. Ashizuka, Materials Science Forum, 449-452 (2004) 1045–1048.
58. F. Yen, C. de la Cruz, B. Lorenz , E. Galstyan, Y.Y. Sun, M. Gospodinov, C.W. Chu, , J. Mater. Res., 22 (2007) 2163–2173.
59. Makoto Tachibana, Tomotaka Shimoyama, Hitoshi Kawaji, Tooru Atake, and Eiji Takayama-Muromachi, Phys. Rev. B, 75 (2007) 144425.
60. J. A. Alonso, M. J. Martínez-Lope, and M. T. Casais, M. T. Fernández-Díaz, Inorg. Chem., 39(5) (2000) 917-923.
61. T. Kimura, S. Ishihara, H. Shintani, T. Arima, K. T. Takahashi, K.Ishizaka, and Y. Tokura, Phys. Rev. B, 68 (2003) p.403.

2. Magnetic materials

All materials exhibit some kind of magnetic response when placed in an external magnetic field, or in other words, all existing materials are in fact “magnetic”. In practice, however, this term is reserved only for materials composed of atoms or molecules with intrinsic magnetic moments, or sometimes more strictly, only for those showing spontaneous magnetization without the presence of external field.

Nevertheless, depending on their behavior in the presence of the field, all materials can be roughly divided into four categories: diamagnetics, paramagnetics, ferromagnetics and antiferromagnetics. All existing materials will exhibit diamagnetic response to the external magnetic field. This simplest form of magnetic behavior is induced by the field (and thus can exist only in the presence of the field). It manifests itself through the generation of a small magnetic moment aligned opposite to the field direction. The bigger the number of electrons (heavier atomic species), the larger diamagnetic moment is generated. In materials without intrinsic magnetic moments this is the only existing type of magnetic behavior.

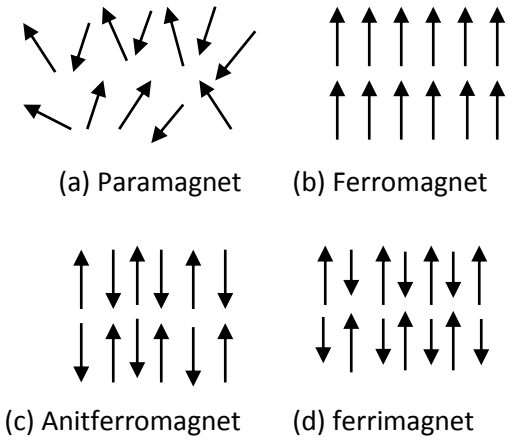

Figure 2.1: Different types of magnetic ordering

In the case when material consists of atoms with unpaired electron spins (incompletely filed electron shells), the intrinsic magnetic moment exists. The origin of this

intrinsic magnetism lies in the orbital and spin angular momentum of electrons. Each unpaired electron in an atom has both spin and orbital magnetic moment, and these combine to produce a total magnetic moment for electron, atom, and finally, an overall magnetic moment for the substance. The actual way in which atomic moments combine to form the final magnetic state in some material, will depend on the type and strength of their mutual interactions. At sufficiently high temperature, thermal energy overrides these interactions and magnetic moments will form disordered state known as paramagnetism (Figure 2.1a). However, below some critical temperature moments will order either parallel or antiparallel to each other, thus forming either ferromagnetic (Figure 2.1b) or antiferromagnetic (Figure 2.1c) ordered state. Ferrimagnetism (Figure 2.1d) is a special case of antiferromagnetic ordering in which magnetic moments in two sublattices are of different magnitude.

Magnetic materials are mostly based on transition elements with incompletely filled *d*-orbital, or rare earth elements with incompletely filled *f*-orbital, or on combinations of both in various compounds and alloys. Both groups of elements are characterized by the existence of intrinsic magnetic moment of an atom. However, the nature of their moments in solid state compounds differs since they differently interact with a crystal or ligand field. In that matter, magnetic moments of transition metals are spin-only, due to a strong interaction with crystal field, and consequently, due to the complete freezing of an electron orbital momentum [1]. In rare earth elements, the effect of the orbital motion of the electrons is not cancelled, and hence both spin and orbital motion contribute to the magnetic moment.

Before discussing the different types of magnetism we need to clear up the definition which is used to categories the types of magnetism -magnetic susceptibility.

2.1. Magnetization and magnetic susceptibility

The response of a material to an applied magnetic filed H, is given by magnetic induction B, as

$$B = \mu_0 (H + M) \text{ or simply } B = \mu_0 H \text{ (in SI system)} \qquad (2.1)$$

where M is the magnetization of the material, μ is the material dependent characteristic called magnetic permeability and μ_0 is the permeability of free space. In SI system, μ has dimensions of (H m^{-1}), and μ_0 is 4 $\pi \times 10^{-7}$ H m^{-1} .

The susceptibility indicates how responsive a material is to an applied magnetic field. Magnetic susceptibility is defined as the magnetization of a material per unit applied field. It describes the magnetic response of a substance to an applied magnetic field. If M is the magnetization and H the applied magnetic field, then the relationship between the magnetization induced in a material M and the external field H is given by Eq 2.1, the magnetic susceptibility, denoted by χ

$$\chi = \frac{M}{H} \qquad (2.2)$$

In the case that M is not parallel to H, χ is a tensor.

2.2. Types of Magnetism

Diamagnetism

In diamagnetic materials the magnetic susceptibility is negative. Usually its magnitude is of the order of -10^{-6} to -10^{-5}. The negative value of the susceptibility means that in an applied magnetic field diamagnetic materials acquire the magnetization, which is pointed opposite to the applied field. In diamagnetic materials the susceptibility nearly has a constant value independent of temperature Figure 2.2.

Owing to the weak magnetic capability, diamagnetic materials do not find wide range of applications, apart from the newly explored applications in the magnetic field induced alignment of liquid crystals [2]. Nevertheless, the use of these materials in the scientific applications and research is of great importance, as most of the superconductors are diamagnetic.

Paramagnetism

Paramagnetism is observed when the spin and orbital dipole moments of the electrons in each atom do not cancel but add vectorially to give the atom a net dipole moment μ. These dipole moments are randomly oriented in the absence of external magnetic field. Hence the net magnetic dipole moment of the material is zero. However when the sample is placed in an external magnetic field the dipole moments tend to align

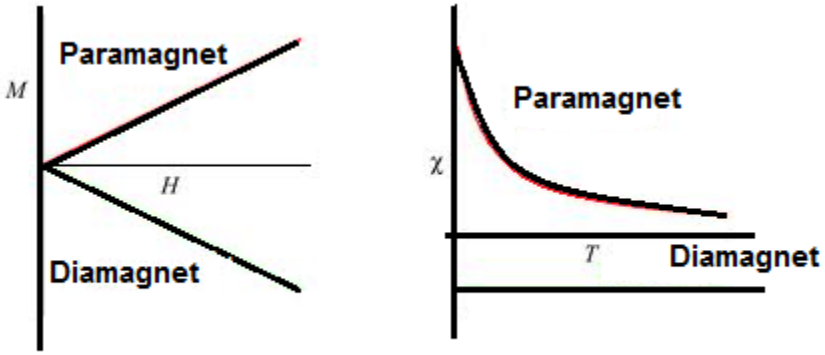

Figure 2.2. Comparison of paramagnetic and diamagnetic in response to magnetic field and temperature

with the field, which give the sample a net magnetic moment.

In paramagnetic materials χ is positive - that is, for which M is parallel to H. The susceptibility is however is also very small: 10^{-3} to 10^{-5}, although paramagnetism can be several orders of magnitude larger than diamagnetism. As temperature increases, paramagnetic substance decreases as shown in Figure 2.2. Example of the paramagnetic materials is substances which contain ions of transition elements, rare earth elements.

Magnetic susceptibility is defined as the magnetization of a material per unit applied field. It describes the magnetic response of a substance to an applied magnetic field. An atom that has an angular momentum quantum number J will have 2J + 1 equally spaced energy levels in a magnetic field. The magnetic moment m is given by

$$m = NgJ\mu_B B_J(x) \tag{2.3}$$

where μ_B is the electron's Bohr magneton with a value of 9.27×10^{-21} emu and the parameter gJ is the spectroscopic splitting factor. A *g*-value is a dimensionless quantity which characterizes the magnetic moment and gyromagnetic ratio of a particle or nucleus. For a free ion, this factor is given by

$$gJ = 1 + \frac{J(J+1) + S(S+1) - L(L-1)}{2J(J+1)} \tag{2.4}$$

where S is the total spin angular momentum, L is the total orbital angular momentum and J is the total angular momentum. The variable

$$x = \left[\frac{gJ\mu_B H}{kT} \right]$$

and BJ(*x*) is the Brillouin function given by

$$B_J(x) = 1 + \frac{2J+1}{2J}\coth\left[\frac{(2J+1)x}{2J}\right] - \frac{1}{2J}\coth\left[\frac{x}{2J}\right] \tag{2.5}$$

where coth(*x)* is the hyperbolic contangent of *x*, H is the magnetic field and N is the mole number for the sample.

At relatively low fields and not too low temperatures we can expand the coth in (2.3) assuming that $x << 1$, so that

$$\coth(x) \approx \frac{1}{x} + \frac{x}{3}$$

We can then find for the susceptibility:

$$\chi = \frac{m}{H} = \frac{Ng_J^2\mu_B^2 J(J+1)}{3kT} = \frac{Ng_J^2\mu_B^2}{3kT} = \frac{C}{T} \tag{2.6}$$

C is the Curie constant and this equation is called the Curie law. From these equations and depending on the value of χ we can describe the different types of magnetism.

Ferromagnetism

Unlike paramagnets, ferromagnetism exhibit a net magnetic moment in the absence of an applied magnetic field. The magnetic susceptibility of ferromagnetism is positive and quite large also its decreases with rise of temperature as shown in Figure 2.3 and above a certain temperature called the Curie temperature a ferromagnetic substance behaves as if it were paramagnetic.

$$\chi = \frac{C}{T - T_C}$$

where Tc represents Curie temperature

Ferromagnetism related to the property exhibited by certain metals, alloys and compounds of the transition (iron group), rare-earth and actinide elements

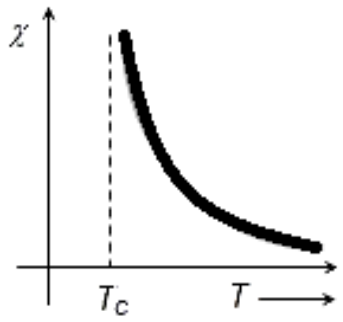

Figure 2.3. χ-T curve is shown
(for Curie-Weiss Law)

Antiferromagnetism

In antiferromagnetism materials, the interaction between the magnetic moments tends to align adjacent moments antiparallel to each other. We can think of antiferromagnets as containing two interpenetrating and identical sublattices of magnetic ions. Antiferromagnetism susceptibility is small and positive. The susceptibility behaves

differently from ferromagnetism, because magnetization couples directly to magnetic field, but staggered magnetization doesn't. The ferromagnetic χ diverges at T_c, but the antiferromagnetic χ merely has change of slope at T_N (Néel temperature). Also, below T_c the ferromagnetic χ is infinite, but the antiferromagnetic susceptibility goes to a constant. The temperature dependence of the susceptibility above the Néel temperature is also similar to that of paramagnet, and the susceptibility, obeys the Curie-Weiss law, as in equation (5) with a negative paramagnetic Curie temperature, Θ determines the true point of transition between paramagnetic and ferromagnetic behavior [4], but below T_N it decreases with decreasing temperature as in figure 2.4.

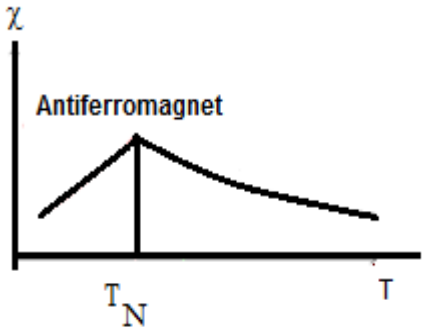

Figure 2.4. T_N in the curve of susceptibility versus temperature

$$\chi = \frac{C}{T - \Theta} \qquad (2.5)$$

Ferrimagnetism

A ferrimagnetic material is one in which the magnetic moments of the atoms on different sublattices are opposed as in antiferromagnetism; however, in ferrimagnetic materials, the opposing moments are unequal and a spontaneous magnetization remains [1]. This happens when the sublattices consist of different materials or ions. Ferrimagnetic materials are like ferromagnets in that they hold a spontaneous magnetization below

the Curie temperature, and show no magnetic order (i.e. paramagnetic) above this temperature.

2.3. Exchange interactions

Magnetic phenomena can be also roughly divided into two groups, “group A” and “group B”. In group A there is no interaction between the individual moments so each moment acts independently of the others. Diamagnetics and paramagnets belong to this group.

Group B consists of the magnetic materials most people are familiar with, like iron or nickel. Magnetism occurs in these materials because the magnetic moments couple to one another and form magnetically ordered states. The coupling, which is quantum mechanical in nature, is known as the exchange interaction and is rooted in the overlap of electrons in conjunction with Pauli's exclusion principle. Whether it is a ferromagnet, antiferromagnet of ferrimagnet the exchange interaction between the neighboring magnetic ions will force the individual moments into parallel (ferromagnetic) or antiparallel (antiferromagnetic) alignment with their neighbors. The three types of exchange which are currently believed to exist are: a) direct exchange, b) indirect exchange and c) superexchange.

2.3.1. The Heisenberg exchange interaction

The commencement of the successful theory of the ferromagnetism is found in the theory due to Weiss which proposes the use of an internal magnetic field (molecular field). This theory gives a good first approximation to the observed behavior of ferromagnetic material, but there was no realistic suggestion as to the physical origin of the internal magnetic field. Later, after the emergence of quantum mechanics, Heisenberg [8] suggested that the interaction which gives rise to the possibility of existence of ferromagnetism is the interaction. The exchange interaction is purely quantum mechanical n origin, and it arise because the wave function of a number of identical particles (such as electrons), must be antisymmertrical with respect to interchange of any two of the particles. Whenever two electron wave function overlap, the Pauli principle applies to the region of overlap. If the orbital wave function is symmetrical, then the spin must be antisymmetrical vice versa.

This leads to a correlation of the spin on the two electrons, which is all that is required to cause a magnetically ordered state. The correlation can be expressed in terms of energy. The interaction energy is proportional to s_1. s_2, where s_1 and s2 are the spin of the two electrons. Heisenberg suggested that the spin-spin exchange interaction may be represented by the following Hamiltonian :

$$H_{Heis}=-2J\ S_1.S_2 \qquad (2.6)$$

Where J is the exchange integral

In a solid each ion is surrounded by many neighboring ions and thus it is necessary to sum the exchange over all the electrons contributing to this energy so that

$$H_{Heis} = -\sum_{i \neq j} J_{ij}\ S_i . S_j \qquad (2.7)$$

Here J_{ij} is an exchange integral. The S_i and S_j are the vactor spin of ith and jth lattice ions respectively. The sum is over all pairs of lattice ions. $J>0$ leads to ferromagnetism and $J<0$ leads to antiferromagnetism.

The exchange interaction discussed above is appropriate for two neighboring atoms with direct overlap with their electron wave function, and therefore, is called direct exchange. This mechanism is not applicable in the magnetic cations of transition metal oxide as the neighboring cations are far apart from each other separated by an oxygen anion between them. Also, in the case of the 4f electrons (spins) of rare earth they are placed so deep onside the atomic core that their wave functions do not overlap with the wave function of neighboring atoms. The radii of the 4f electron shells are about 0.3 Å and 4f electrons are at the distance of 3 Å from neighboring atoms. In addition the 4f electrons are well screened by the 5s and d electrons.

2.3.2. Superexchange

Superexchange is an indirect exchange interaction between non-neighboring magnetic ions, which is mediated by a non-magnetic ion that is placed in between them. This interaction was first proposed by Kramers [9] in 1934 to the aim of finding an explanation for the

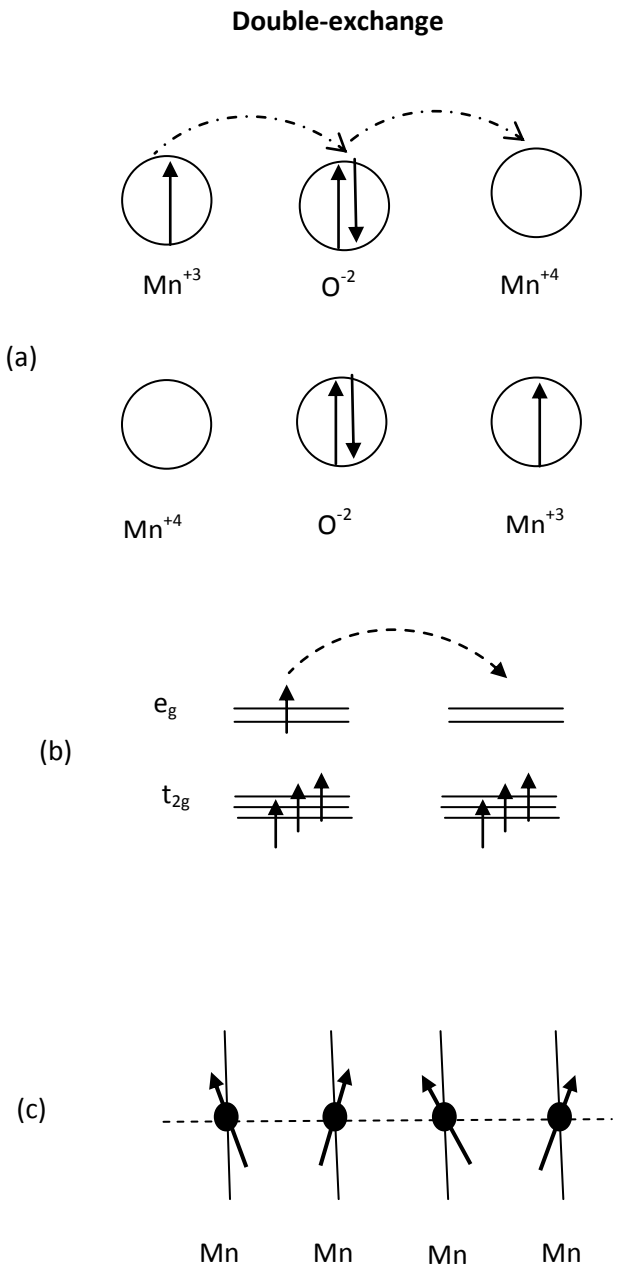

Figure 2.6. A sketch of double exchange mechanism.

magnetic properties observed in insulating transition metal oxides, in which the magnetic ions are so distant that a direct exchange interaction could not explain the presence of

magnetically ordered states, so the longer-range interaction that is operating in this case should be “super”.

Superexchange is a kinetic exchange that involves a virtual charge transfer. Superexchange specifically applied to manganite perovskites describes not only the spin-spin interactions between the orbitally non-degenerate, localized t^3_{2g} configuration, but also the interactions via localized e_g electrons. In 1950, Anderson [10], who is gave the first quantitative formulation showing that the superexchange favors antiferromagnetic order.

The superexchange and double exchange are two particularly important indirect interactions of electrons via an intermediary in complex transition metal oxide (CTMO). Both effects are strongly dependent on the magnetic moments of Mn ions, the overlap integral between orbitals of Mn and O ions, and the Mn-O-Mn bond angle in manganites.

2.3.3 Double Exchange (DE)

The theory of double exchange is concerned with the exchange process involving d-band carriers in mixed valence oxides. The double exchange phenomenon governs magneto-transport properties up to the changing carrier from Mn^{3+} to Mn^{4+} ion through oxygen atom. This kind of the electron exchange, first postulated by Zener [11], to explain the properties of $(La^{+3}_{1-x}\ A^{+2}_{x}\ )\ (Mn^{+3}_{1-x}\ Mn^{+4}_{x})O_3$, the theory of double exchange was formulated by Anderson and Hasegawa. The compound at the two ends of the series is an antiferromagnetic insulator. For x = 1/3, the compounds become ferromagnetic and metallic below the Curie temperature. This correlation can be qualitatively explained with the theory of double exchange [6].

In the $La_{1-x}A_xMnO_3$ (A=divalent ions), the substitution of divalent ions for the trivalent ions creates holes as Mn^{+4} ($t^3_{2g}e^0_g$) ions in the system. The e_g electrons are aligned parallel to the localized spin (core spin) t^3_{2g} by strong Hund’s coupling. The hopping of an electron between Mn^{3+} and Mn^{4+}sites is affected by the relative alignment of local spin, being maximal when localized spins are parallel and minimal when they are antiparallel. When the electrons hop from Mn^{3+} ($t^3_{2g}e^1_g$) to Mn^{4+} ($t^3_{2g}e^0$) by the double exchange mechanism, their spin alignment remains unchanged. This hoping process gives rise to

metallic conductivity and brings about ferromagnetism. The transfer of a hole occurs simultaneously from Mn^{4+} to O and from O to $Mn^{3+.}$

$$t^3_{2g}e^1_g - O - t^3_{2g}e^0_g \longleftrightarrow t^3_{2g}e^0_g - O - t^3_{2g}e^1_g$$

The sketch of the double exchange mechanism is shown in Figure 2.6. This involves two Mn ions and one O ion (Figure 2.6. (a)). The mobility of e_g electrons is improved if the localized spins are polarized (Figure 2.6. (b)). Spin-canted state, which appears as the interpolation between FM and AF states in some mean field approximations is shown in (Figure 2.6. (c)) [6]. In addition, if the localized spins are considered classical and with an angle θ between nearest neighbor ones, the effective hopping becomes proportional to $\cos(\theta/2)$. If $\theta=0$ the hopping is the largest, while if $\theta=\pi$, corresponding to antiferromagnetic background, than the hopping cancels.

References

1. Halliday, D., Resnick, R. and Walker, J.. Fundamentals of Physics (Extended), John Wiley & Sons Inc., (1997).
2. Nicola A. Spaldin, Magnetic materials Fundamentals and applications, Cambringe university press, (2003
3. Maignan . A, Sundaresan. A, Varadaraju. U, Raveah. B, J. Magnetism and Magnetic Materials, 184 (1998) 83-88.
4. Blundell. S. J., Magnetism in Condensed Matter, Oxford University Press, (2003).
5. Buschow. K. H. J and F. R. de Boer, Physics of Magnetism and Magnetic Materials, Kluwer academic publisher, (2003).
6. Dagotto. Elbio., Hotta. Takashi., Moreo. Adriana, Phys. Reports, 344 (2001) 1-153.
7. Tokura. Y, Tomioka. Y, J. Magnetism and Magnetic Materials, 200 (1999) 1-23.
8. W.Heisenberg, Z. Phys. Rev., 49 (1928) 619-636.
9. H. A. Kramers, Physica, 1 (1934) 182-192.
10. P. W. Anderson, Phys. Rev., 79 (1950) 350-356.
11. C. Zener, Phys. Rev., 82 (1951) 403-405.

3. Sample characterization techniques

The determination of the structure and magnetic properties of $Y_2Cu_2O_5$ [YCuO], and $Y_2(Cu_{(1-x)}Mg_x)_2O_5$ with x=0.0, 0.05 and 0.15 , systems, as well as of the nanoparticle $YMnO_3$ has been performed by the use of powder X-ray diffractometry (XRPD) and magnetic measurements performed at Phillips PW1050 diffractometer with Cu Kα radiation and Quantum Design MPMS XL-5 SQUID magnetometer, respectively. The data obtained by XRPD technique were analyzed by full profile Rietveld method [1], which is implemented trough the FullProf program [2].

Both experimental techniques, including the Rietveld method for crystal structure analysis are described in more details within the next three sections.

3.1. X-ray diffraction analysis

The properties of crystal structure of crystalline materials can be obtained by studying diffraction of three different types of radiation: x-rays, neutrons or electrons. The consequent diffraction methods based on these radiations are complementary since they all implement different scattering processes. Electrons are strongly scattered by electrostatic potential of an atom. X-rays are scattered by electron cloud, and have considerably higher penetration power than electrons. Neutrons are scattered both by atomic nucleus (nuclear scattering) and by unpaired electron spins (magnetic scattering). Therefore, these differences will make either of methods particularly convenient, depending on the form of the examined crystalline material. For example, the diffraction of electron beam will be highly usable in case of thin films, since electrons have low penetration power and can "see" only the surface area of the sample. On the other hand, the diffraction of X-rays or neutrons is much more convenient for bulk samples, and represents one of the most important, powerful and widely used analytical techniques available. Due to the magnetic scattering by unpaired electron spins, neutrons can be used for the determination of magnetic structure, which cannot be accessed directly by any other type of experiment. However, neutron diffraction measurements are expensive, not easily available, and demanding for large amounts of specimens (high penetration but low scattering power).

For the most of crystalline substances, the bulk properties of a powder or a polycrystalline solid, averaged throughout the sample are required; a single-crystal diffraction (when single crystals can be obtained), are usually of little interest except for the determination of unknown crystal structure or for studying of some other fundamental physical property. In general, powder diffraction frequently forms part of a wider investigation of physical, chemical or mechanical properties of materials. The structure information on the materials and samples investigated in this thesis is obtained by x-ray powder diffraction.

3.1.1. X-ray powder diffractometer

Considering the high cost of neutron diffraction and the limitations of electron scattering, it is understandable that the X-ray diffraction (XRD) is one of the most commonly used laboratory techniques to determine structural details of crystalline material. The wavelength of used X-rays is usually around 1-2 Å, which is in about the same scale as the spacing between atoms in crystalline solids. In that case crystals will behave like diffraction grating for X-rays, and may be viewed as the planes of atoms stacked on top of each other to form the ordered structure. These planes are separated by a gap commonly known as their "d-spacing" and X-rays, which show wave phenomena, can be diffracted by these planes. Figure (3.1) shows the schematic representation of a typical X-ray diffractometer in the so called theta-two theta configuration.

X-ray diffraction results from the interaction between X-rays and electron clouds of atoms in crystals. Depending on the atomic arrangement, interferences between the scattered rays can be constructive or destructive; they are constructive when the path difference between two diffracted rays differs by an integral number of wavelengths, which means that the successive diffracted rays are "in phase". This selective condition is described by the Bragg equation (3.1), also called "Bragg's law".

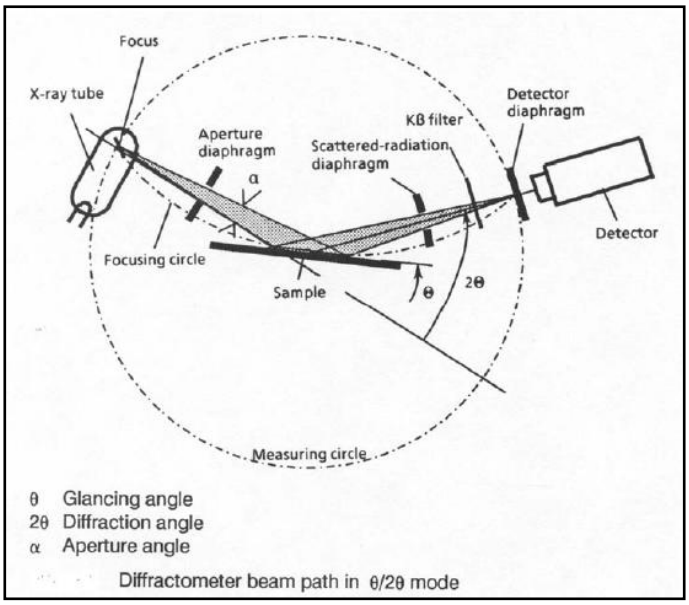

Figure 3.1: shows the schematic representation of x-ray diffractometer.

When incoming x-ray beam is directed at an angle θ to the sample, it is then reflected from many parallel crystal planes in the sample at the same angle (Figure 3.2). If the radiation reflected from the individual planes has differences of one or several full wavelengths, reflection maximum appears and this is called x-ray reflection spot. The application of X-ray light can be very useful to study the interaction with an atom and to try resolving the crystal structure based on their diffraction pattern. W.H Bragg and W.L Bragg have introduced the relation between the scattering angle (θ) and the distance among the lattice planes (d) of a crystal [3]:

$$2d \sin \theta = n\lambda \qquad (3.1)$$

where n is order of reflection (an integer), d is interplanar spacing, and θ is the Bragg angle.

Refining the lattice parameters of the unit cell from X-ray powder diffraction data requires knowing how to assign the Miller indices (*h k l*) to each diffraction peak, a process known as indexing the pattern. The Miller indices relate the peak positions or *d*-spacing to the lattice parameters by an equation specific to the crystal system. For example, in a structure with an orthorhombic unit cell the relationship is expressed in equation (3.2)

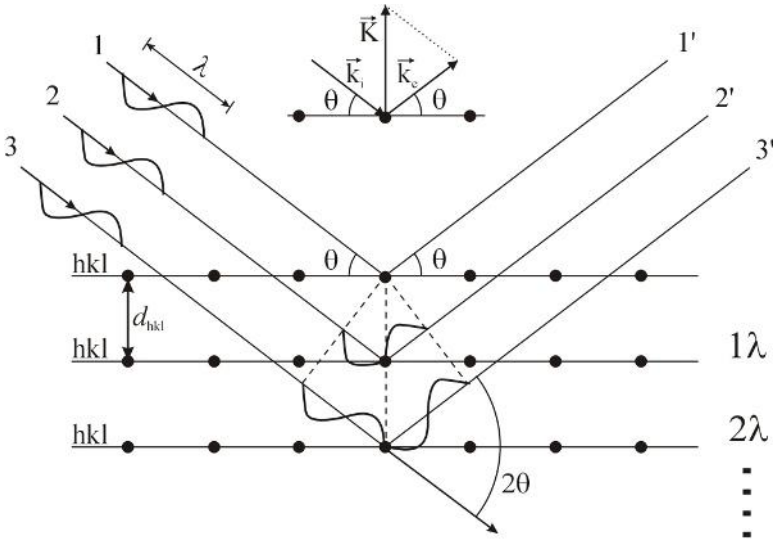

Figure 3.2: Schematic illustration of fundamental process in XRD measurement.

$$\frac{1}{d_{hkl}^2} = \frac{h^2}{a^2} + \frac{k^2}{b^2} + \frac{l^2}{c^2} \tag{3.2}$$

where *a*, *b*, and *c* are the lattice parameters of the unit cell and *hkl* are the Miller indices identifying the repeating planes causing the diffraction peak with spacing d_{hkl}.

While the diffraction peaks positions determine the geometry of crystal lattice, the intensities of the peaks are related to what kinds of atoms are placed within the planes. This is simply due to the fact that scattering intensities for X-rays are directly related to the number of electrons in the atom.

The control of the x-rays beam collection suffers from the constraint that lenses and other refractive elements are not as easily available as those used for visible light. For this reason the beam conditioning in θ / 2θ diffractometers is mostly performed by slits and apertures and may be termed shadow-casting optics. In addition, powder diffractometers have to deal with the divergent beam characteristic that is emitted by an x-ray tube.

Most systems operate in the so-called Bragg–Brentano or para-focusing mode. In this configuration a focusing circle (FC) is defined as positioned tangentially to the sample surface (Fig.3.3). The focusing condition in the Bragg–Brentano geometry is obeyed when

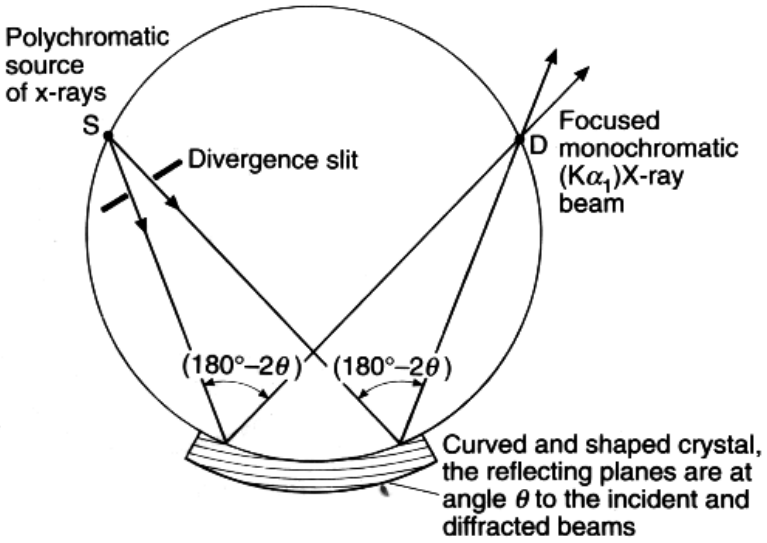

Figure 3.3: The principle of the x-ray monochromator

the x-ray source and detector are positioned on the goniometer circle where it intersects the focusing circle. True focusing would indeed occur only for a sample that is bent to the radius of the focusing circle ($R_{FC)}$. Since ($R_{FC)}$ differs for various scattering angles 2 θ, true focusing cannot be obtained in a θ / 2θ scan and the arrangement is thus termed para-focusing geometry [4].

3.2 The Rietveld method

The analysis of the crystal structures of higher symmetry crystals is rather simple, having in mind that the peaks are well resolved and integrated intensities could easily be obtained for further refinement. However, with more complex compounds and of a lower symmetry (polycrystalline), the overlap of peaks is usually so severe that their separation becomes practically impossible. Historically, in an attempt to overcome this problem, firstly the resolution of the diffraction experiment was increased [5]. This proved to be of appreciable value, especially for structure determination. For structure refinement, however, the

increase of resolution certainly resulted in a better defined profile, but often not to such an extent that the peaks were completely resolved. The solution then was to refine the structure by using not only single intensities as data but also groups of overlapping intensities [6]. This peak profile fitting procedure only works for relatively simple structures which yield diffraction patterns with minimal peak overlap.

The full profile Rietveld method emerged somewhat later, in the late sixties 1967, and used for refinement of crystal structures from powder diffraction patterns collected experimentally by x-ray or neutron powder diffraction data.

To refine the structure parameters it is necessary that the experimental diffraction data are collected with good statistics, as well as to know the space group in which the investigated material crystallizes. Refinement itself is an iterative process in which the structural parameters (unit cell parameters, fractional atomic coordinates, occupancy parameters), and profile parameters (parameters which describe the Bragg reflections by introducing analytical functions) have been refined. Therefore, the initial model requires assigning approximate values of these parameters. Different computer programs, used to refine the crystal structure, are based on Rietveld method. In this thesis, the Fullprof program was used [2]. In the Rietveld's method, each count of diffraction patterns is considered separately. It means that the program calculates the intensities at each step and compares with the experimentally obtained one. Such method is advantageous over classical methods which are based on refinement of the integrated intensities of individual Bragg reflections, and therefore, since it does not suffer from peak overlapping, there is no need to discard large portions of diffraction pattern.

The Rietveld method is the least squares method, based on minimizing the sum of squares of the differences of experimental, y_{exp}, and theoretical, y_{theory}, intensity at each point of the profile [7]. Quantity minimized is given by:

$$x^2 = \sum_i w_i \left(y_{i,obs} - S y_{i,cal} \right)^2 \tag{3.5}$$

Where, $y_{i,obs}$ is the observed intensity at the *i-th* step, $Y_{i,cai}$ the calculated intensity at the *i-th* step, $w_i = y_{i,obs}^{-1}$ is a weighting factor, *S* is the scale factor. Weighting factor is equal to the reciprocal value of the square of the standard deviation:

$$w_i = \frac{1}{\delta^2} = \frac{1}{y_{i,ob}} \tag{3.6}$$

or

$$w_i = \frac{1}{y_{i,cal}} \tag{3.7}$$

Scale factor, S is defined by the relation $y_{i,obs} = S\, y_{i,cal}$.

Theoretically calculated reflection intensity y_i, at an angle $2\theta_i$ consists of contributions from the baseline (background), b_i, and those of the reflection spectrum from the point $2\theta_i$. Total intensity at point 2θi can be represented as a product of the integral intensity, I_k, and the shapes of the reflectance functions Ω_k. Then the theoretical value of the intensity is as follows:

$$y_{i,teor} = b_i + \sum_k I_k \Omega_k (2\theta_i, 2\theta_k) \tag{3.8}$$

The shape of the diffraction line depends on several factors including: type of diffraction experiment, particle size, etc. The appropriate function that's a mixture of Gauss (G) and Lorentz function, such as Pseudo-Voigt function that we have used in our analysis:

$$pV(x) = \eta L(x) + (1-\eta) G(x) \tag{3.9}$$

with a mixing factor η,($0 \le \eta \le 1$),. The convoluted profile can take any shape between the pure Gaussian profile (η=0) and pure Lorentzian profile (η=1).

Gauss function:
$$G(x) = \frac{2}{H_G}\sqrt{\frac{\ln 2}{\pi}} \exp\left[-\frac{4\ln 2}{H_G^2} x^2\right] \tag{3.10}$$

Lorentz function: $$L(x) = \frac{2}{\pi H_L \left(1 + \frac{4}{H_L^2} x^2\right)} \quad (3.11)$$

The form of a Bragg reflection is very close to a Gaussian (a normal distribution curve) and the full width at half maximum (FWHM) of the reflection can be described with a polynomial of the form:

$$H^2 = U \tan\Theta + V \tan^2\Theta + W \quad (3.12)$$

Where H is the half width for a certain 2Θ value and U, V and W are refinable parameters, which can be varied in the least-square procedure.

The quality of the fit is expressed by the below given numerical agreement of reliability factors, and is also checked by plotting the difference between the observed and calculated profiled [6,7].

The profile R- factor $$R_p = \frac{\sum |Y_{i,obs} - Y_{i,cal}|}{\sum Y_{i,obs}} \quad (3.13)$$

The weighted Rp $$R_{wp} = \left[\frac{\sum w_i \left(Y_{i,obs} - Y_{i,cal}\right)^2}{\sum w_i Y_{i.obs}^2} \right]^{1/2} \quad (3.14)$$

The Bragg R-facor $$R_{Bragg} = \frac{\sum |I_{kobs} - I_{kcal}|}{\sum I_{Kobs}} \quad (3.15)$$

where R_p is the sum of the difference between the observed and calculated points. The R_{wp} is more accurate as it involves the weighted profile which gives more weight to the differences in peak intensity rather than the background. The R_{WP}-profile and R_p factors summarizes the profiles of all counts, while in the Bragg factor R_B is conducted by summing all the reflections that contribute to the intensity of the reflection under

consideration. R_{Bragg} is commonly quoted and gives information on the correctness of the crystal structure model

The expected R_F $R_{\exp} = \left[\frac{(N-P)}{\sum w_i Y_{i,obs}^2} \right]^{1/2}$ (3.15)

The goodness of fit $x^2 = \left(\frac{R_{wp}}{R_{\exp}} \right)^2 = \frac{\sum w_i (Y_{i,obs} - Y_{i,cal})^2}{N-P}$ (3.16)

where $I_{K,obs}$ is the observed integrated intensity of reflection k., N is the number of observation, and P is the number of parameters refined [8].

R_{exp} is the statistically expected R-value, and thus reflects the quality of data instead of the agreement with the structure refinements. The value x^2 is also used as a guide to the goodness of fit, the lower value of x^2 the better the fit is.

3.3 DC magnetic susceptibility measurement

All magnetization measurements in this work were performed using a Quantum Design XL-5 SQUID-based magnetometer, shown in Figure 3.4. The Magnetic Property Measurement System XL-5 SQUID (Superconducting Quantum Interference Device) is composed of a liquid-helium cooled SQUID that measures the changes in the magnetic flux as the sample moves through a superconducting detection coil. This device acts as a very sensitive magnetometer, since it can detect changes as small as one flux quantum which is equal to 2.07×10^{-15} Tm^2. The SQUID system at the Vinca Institute, allows measurements of the magnetic properties from around 2 K up to 400 K under magnetic fields up to 5T. The sensitivity of the measurement is 10^{-6}-10^{-8} emu (corresponding to 10^{-9}-10^{-11} Am^2 in SI units), depending on the setup.

A Superconducting Quantum Interference Device is a device that appeared with the development of superconducting materials and technology because of its sensitivity and quickly became one of the standard devices for measuring the magnetization, susceptibility,

Figure 3.4: Quantum Design XL-5 SQUID-based magnetometer

or magnetic fields. In addition to magnetic fluxes, other physical values can be measured if they can be adapted to the magnetic flux. Attainable sensitivities of flux densities (10^{-14} T) of electrical current (10^{-12} A) and of electrical resistance (10^{-12} Ω) reflect the high accuracy of a SQUID.

High sensitivity of the device is achieved by using superconductors, instead of ordinary semiconductors to build magnetic flux sensor. Superconducting current can be represented as a current of the pairs of electrons known as Cooper pairs [9]. Each Cooper pair can be considered as a single particle with a mass and charge twice of that of a single electron, which velocity is that of the center of mass of the pair. The important property of Cooper pairs is that they form a coherent wave package, and this is used to build a quantum interferometer, a sort of equivalent of Jung experiment in optics. Actually, the SQUID is an interferometer build with an aid of so called Josephson's junctions [10]. A Josephson junction is realized by interrupting a superconductor by a very thin insulating barrier. This weak link in the superconducting line will cause super current to change the phase of the wave package when tunneling through the junction. The function of the SQUID is to

measure the quantum mechanical phase difference of the Cooper pairs wave functions over a Josephson contact when the magnetic flux is penetrating the interferometer loop [9] (Figure 3.5). Depending on the number of Josephson's junction there are two different types of SQUID devices: AC (or RF) SQUID has only one Josephson's junction, while the DC-SQUID type has two Josephson's junction. In the DC-SQUID, the superconducting current is divided at the point A into two routes, X and Y, and then recombined at the point B. If the route Y is put in the magnetic field and the route X remains no changes, the difference in the phase of the Cooper's wave functions will be appeared at point B.

The intensity of the superconducting current J flowing through the barrier can be described by the equation [11]:

$$J = J_0 \sin\delta ,$$

where δ - is the phase difference, and J_0 – is the amplitiude of the Josephson current, (J_0 is very sensitive to the presence of magnetic field in Josephson junction). The relation between the phase difference, δ, and a voltage, U, inside the Josephson junction[11], is given by:

$$\delta = \delta_0 + \frac{2e}{\hbar}U$$

Superconducting current can flow through the Josephson junction's even when there is no voltage across the junction. Then the phase difference, δ is a constant in time, while the amplitude J_0 depends on the magnetic flux, Φ. If there is a magnetic flux inside the junction, the superconducting current is:

$$J = J_S \frac{\sin x}{x} ,$$

where $x = \frac{\pi\Phi}{\Phi_0}$; Φ - is the total magnetic flux in the junction, Φ_0 - is the quantum of flux ($\Phi_0 = h/2e \cong 2{,}0678\times10^{-15}$ Tm^2), and J_S – is the current which depends on the temperature and the structure of the junction, but not on the strength of the magnetic field [9]. By

measuring a superconducting current it is possible to measure a magnetic flux in a Josephson junction.

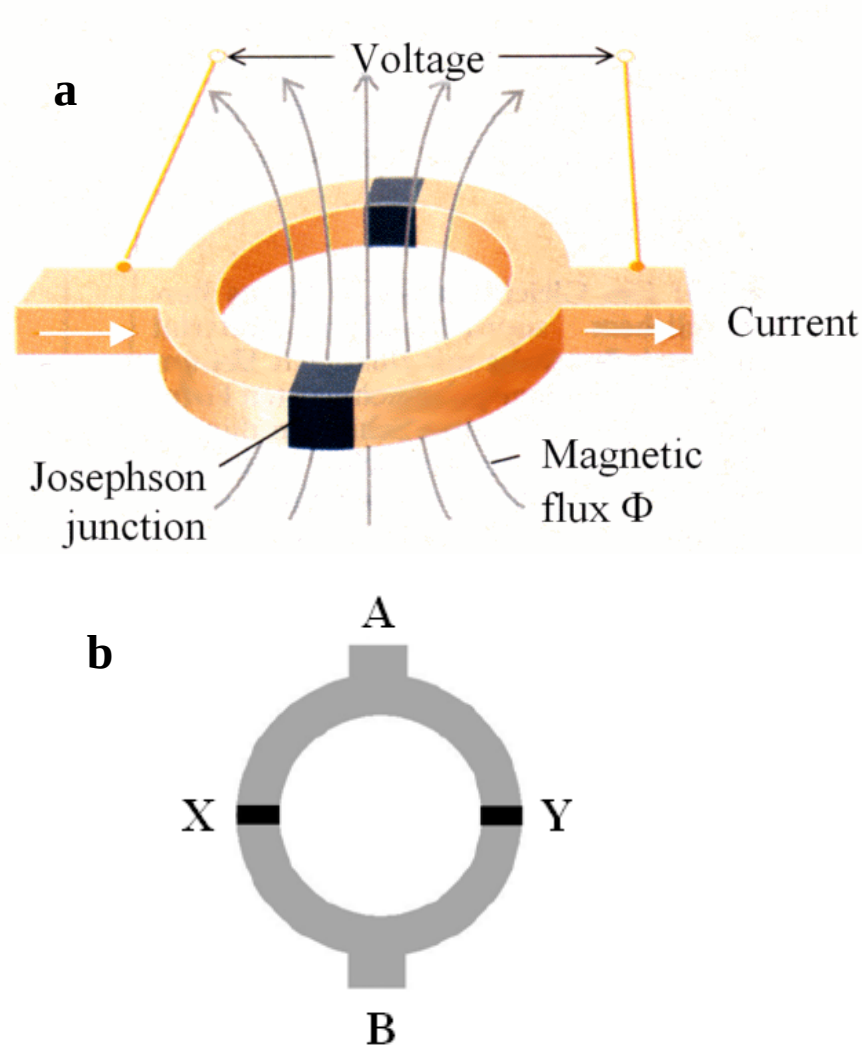

Figure 3.5. (a) The working principle of a SQUID, (b) superconducting circuit with two Josephson's junctions

3.3.1. Mounting the sample

An extreme care has to be taken while mounting the sample because this can have considerable influence on the measurement accuracy by several factors like size and the

shape of the sample. The powders are usually kept inside the gelatin capsules (which have a small diamagnetic signal). Before measuring, the gelatin capsules are weighted separately, so that the exact weight of the samples can be calculated from the difference between full and empty capsules. The necessary quantity of the sample depends on its magnetic response (ferromagnetic materials with high magnetization will demand smaller amounts), but the powder masses of around 40 mg are usually appropriate. The powder is pressed into the tube or the epoxy resign is used to glue the powdered samples to the capsule in order to prevent the movement of the sample particles due to a magnetic torque caused by strong magnetic fields during the measurements. The tube with the encapsulated powder is than mounted on the SQUID sample holder and inserted into the sample space.

3.3.2. Types of measurements

An important way to investigate the temperature behavior of a magnetic system is to compare the magnetization after having cooled the sample in zero field (ZFC) and after having cooled it in the measurement field (FC).

All of the measurements presented here are done after zero-field-cooling (ZFC) and field cooling (FC) conditions. In ZFC regime, the sample is cooled down below its transition temperature under no applied field. A field is then applied at the lowest temperature and the sample is measured upon heating. Inthe FC measurements, the sample is cooled down through the transition under an applied magnetic field. At the lowest temperature, the field applied during cooling is removed and the same field as used in the ZFC measurement is then applied while the sample magnetization is measured upon heating. The sample is heated up a constant rate. While the magnetization is measured during the sample is being cooled in zero field, the particles tend to magnetize along a preferential crystal direction in the lattice to minimize the magneto-crystalline energy. The net moment of the system will be zero, since the orientation of each crystal varies. This will still be the same when a small external field is applied. With an increase in the temperature, more disturbing energy is introduced into the system, so the magnetic moment will be disordered from the crystal direction and will align in the external field direction to minimize the magnitude.

References

1. R. A. Young, “The Rietveld Method”, Oxford University Press Inc., (1993).
2. Juan Rodriguze-Carvajal, , Physica B, Condensed Matter, 192 (1993) 55-69.
3. L. Azaroff, M. Buerger, “The Powder Method in X-ray Crystallography”, McGraw-Hill, (1958).
4. X-Ray Diffraction Crystallography: Introduction, Examples and Solved Problems, Yoshio Waseda., B. O. Nucl. Instrum. Method 44 (1996) 181-187.
5. Retveld, H. M, Acta Crystallogr., 20 (1996) 508.
6. H. M. Rietveld, J. Appl. Cryst., 2 (1969) p.65.
7. R. A. Young (editor): The Rietveld Method, Oxford Science Publication, (1996).
8. R. C. Jaklevic, John Lambe, A. H. Silver, and J. E. Mercereau, Physical Review Letters, 12(7) (1964) p.159.
9. L. P. Lévi, Magnetism and Superconducuctivity, Springer-Verlag, (2000).
10. M. Tinkham, Introduction to Superconductivity, McGrow-Hill, (1975).

4. Synthesis influence on magnetic properties of $Y_2Cu_2O_5$

The quality of samples depends to a great extent on the synthesis method used. Structure, surface morphology, grain growth, transport of electrons within material and magnetic properties depend on material synthesis. There are various methods available for the synthesis of both polycrystalline bulk and nano-materials like solid state reaction (SSR) route, sol-gel route, co-precipitation method, citrate decomposition route, nitrate decomposition route, etc. In this study we demonstrate the improved technique for the preparation of polycrystalline $Y_2Cu_2O_5$, since a classical sintering route represents an extremely slow and cumbersome process that usually takes more than 10 days to complete. We have successfully applied two alternative synthesis routes, based on precursors obtained by glycine-nitrate and SHS combustion reactions. The applied methods proved to be far superior over the standard ceramic sintering, with one of them (SHS) resulting in the reduction of overall synthesis time to only 12 hours. In addition, the substitution of Cu in $Y_2Cu_2O_5$ by Mg has been also done via SHS combustion reaction. The details of both applied combustion routes are described in this chapter. Another compound analyzed within this study was the nanoparticle $YMnO_3$, which was also prepared via modified SHS method.

As discussed in the first chapter, $Y_2Cu_2O_5$ is known as a "blue phase" that was initially discovered during the preparation of a high temperature superconductor $YBa_2Cu_3O_7$ [1]. Though not being a superconductor itself, this material has instantly attracted attention with its peculiar magnetic properties, particularly its metamagnetic behavior [1-4]. Recently, the discovery of it being a multiferroic with a strong magneto-dielectric coupling [5] aroused a new interest in $Y_2Cu_2O_5$.

The complex balance between ferro- and antiferromagnetic exchange interactions, which is the main cause of the specific magnetic behavior of $Y_2Cu_2O_5$, is closely related to the properties of its crystal structure. This structure (orthorhombic, space group $Pna2_1$) has been extensively studied by X-ray and neutron diffractions [6-9], and it could be most easily visualized through Cu_2O_8 dimmers, forming parallel zigzag chains along the ***a***-axis, while being separated by layers of Y. It is well known that some of the intriguing magnetic

properties of $Y_2Cu_2O_5$, like short range magnetic ordering [10], metamagnetic transitions [1-4], or magnetic anomaly at 6 K [11, 12], are closely related to this structure motif and therefore highly susceptible to the change of the structure parameters.

The renewed interest in $Y_2Cu_2O_5$ as a multiferroic material, and the high susceptibility of its physical properties to the change of the crystal structure parameters, imposes an even bigger significance on a quality sample preparation. This is actually hampered by the unfavorable thermodynamic phase equilibrium in the Y_2O_3-CuO system, which gives a low melting (and decomposing) temperature for $Y_2Cu_2O_5$ that sets between 1100°C - 1150°C [13, 14]. As a result, polycrystalline $Y_2Cu_2O_5$ samples are typically sintered at 900 °C -1100 °C in a cumbersome multi-step process, with a long sintering time and frequent regrinding. Despite such persistence, careful structure analysis of sintered samples frequently reveals a remanence of Y_2O_3 (and correspondingly, CuO), even in samples sintered for appreciably long time. For example, Garcia et al [7] observed as much as 3.6% of R_2O_3 impurity in $R_2Cu_2O_5$ (R=Y, Er, Tm, Ho and Yb) after the samples were sintered at 950°C for the total firing time of 12 days. So far, attempts to modify the ceramic synthesis route were scarce, and only Bhargava et al. [15] have reported a successful $Y_2Cu_2O_5$ preparation from a precursor mixture of yttrium and copper oxalates.

Here we introduce two alternative routes for the $Y_2Cu_2O_5$ synthesis. The first one starts from highly reactive precursor obtained by the glycine-nitrate (GN) method [16], and the second one is a modified self-propagated high temperature synthesis (SHS) [17-19]. The aim of this study was to establish a more efficient preparation method which reduces the synthesis time, and allows for obtaining the polycrystalline samples that are free from both cationic disorder and Y_2O_3 contamination. For the sake of comparison, a slightly modified standard solid state sintering (SSR) from Y_2O_3/CuO powder mixture was also considered.

4.1. Sample preparation

Three samples of $Y_2Cu_2O_5$ denoted as S1, S2 and S3 were synthesized by solid state reaction: from Y_2O_3-CuO mixture (S1 sample), from precursor powder obtained by the GN method (S2 sample), and from precursor powder obtained by using the modified SHS route

(S3 sample). The same aqueous solution of Y- and Cu- nitrates prepared from dried powders of Y_2O_3 and CuO (99.9% purity) was used in all applied methods for precursor preparation. The weight of the oxide powders was measured by a Ohaus GA200D balance with 10^{-5} g accuracy. The mixture of oxides was dissolved in boiling concentrated nitric acid, and the so-obtained nitrate solution was continuously stirred for 3 hours to achieve high homogeneity. The sintering process in all cases was always carried out in an O_2 flow to avoid formation of a parasitic $YCuO_2$ phase [14]. The sintering was conducted until the phase-purity of the samples was confirmed by X-ray diffraction.

The inductive coupled plasma optical emission spectrometry (ICP-OES) was used to check the chemical composition of final samples, by utilizing a Spectroflame-model P spectrometer operating at 2.5 kW and 27.12 MHz. X-ray powder diffraction (XRD) was used as a main tool for the characterization of the crystal structure and for determining the phase content of the final specimens, as well as for testing the samples between intermediate sintering steps. All of the diffraction patterns were collected at Philips PW-1710 diffractometer (Cu Kα, radiation; λ = 1,5406 Å). The data were collected from 10^0 up to 110^0 2θ angle, with a step size of 0.02^0, and a counting time of 12 s per step. The crystal structure of all samples was analyzed and refined by full-profile Rietveld method, using Fullprof program [20]. The magnetic properties of the samples were checked by using a Quantum Design MPMS-XL5 SQUID Magnetometer in direct current (DC) magnetic fields in the range 0 T≤ H ≤ 5 T, and at temperatures between 2 K and 300 K.

4.1.1. Standard solid state reaction (SSR)

In the most common approach to $Y_2Cu_2O_5$ sintering, the starting powder mixture is usually composed of mechanically homogenized, micron-grade powders of yttrium and copper oxides [7, 21]. In order to take advantage of the maximum homogenization and smaller grain size (increased powder reactivity), we used the oxide mixture obtained by thermal decomposition of the above described solution of Y- and Cu- nitrates. The solution was gradually evaporated until the nitrates were decomposed to oxides at 400 °C in air. Thus obtained mixture was ground and subsequently heated at 800 °C for 4 h in oxygen atmosphere. In the next step, the powder was pressed into a pellet under 0.4 t/cm^2 of

pressure, and heated at 900 °C for 10 hours, which was repeated twice, with intermediate grindings. This procedure was repeated five more times at 950°C for 10 h. The final S1 sample was obtained after the last sintering step at 1050°C for 10 h, resulting in 74 h of overall sintering time.

4.1.2. The glycine-nitrate method (GN)

For the S2 sample preparation, the precursor powder was obtained by a low-intensity combustion reaction between the mixture of Y- and Cu-nitrates and glycine. The applied procedure corresponds to the standard glycine-nitrate method [16], with the amount of glycine added to the nitrates solution in a 1:1 molar ratio. The solution was continuously stirred at room temperature for two hours and subsequently heated on a hot plate at 200 ^{0}C until the blue gel-like residue underwent self-ignition. After the smoking stopped, the remaining soft green–brown powder was ground in an agate mortar. This precursor powder was then heated at 800 ^{0}C for 3 h, reground, pressed into a pellet under 0.4t/cm^2, heated at 950 ^{0}C for 4 h, and at 1050 ^{0}C for 24 h, with several intermediate grindings. Overall, this method required about 31 h of sintering time to achieve the pure orthorhombic $Y_2Cu_2O_5$.

4.1.3. Modified self-propagated high temperature synthesis (SHS)

In this approach, a modification of the SHS combustion method [17-19] was used to obtain the precursor powder for the S3 sample. The selected type of the SHS route was the same as the modification recently applied in the single-step combustion synthesis of the nanoparticle $La_{0.7}Ca_{0.3}MnO_3$ reported in [17]. The basic goal of this specific SHS modification was to trigger a brief thermal decomposition of Y- and Cu-nitrates, as well as the subsequent formation of the final compound, by using the thermal energy from burning redox mixture (glucose + KNO_3). Since the molar ratio between the nitrates and redox mixture is freely adjustable, the temperature of the reaction could be easily tuned not to exceed 1000 ^{0}C, unlike in most other solid-state combustion routes [18, 19]. Thus, it was reasonable to assume that such concept could be also applied for the preparation of the $Y_2Cu_2O_5$ precursor.

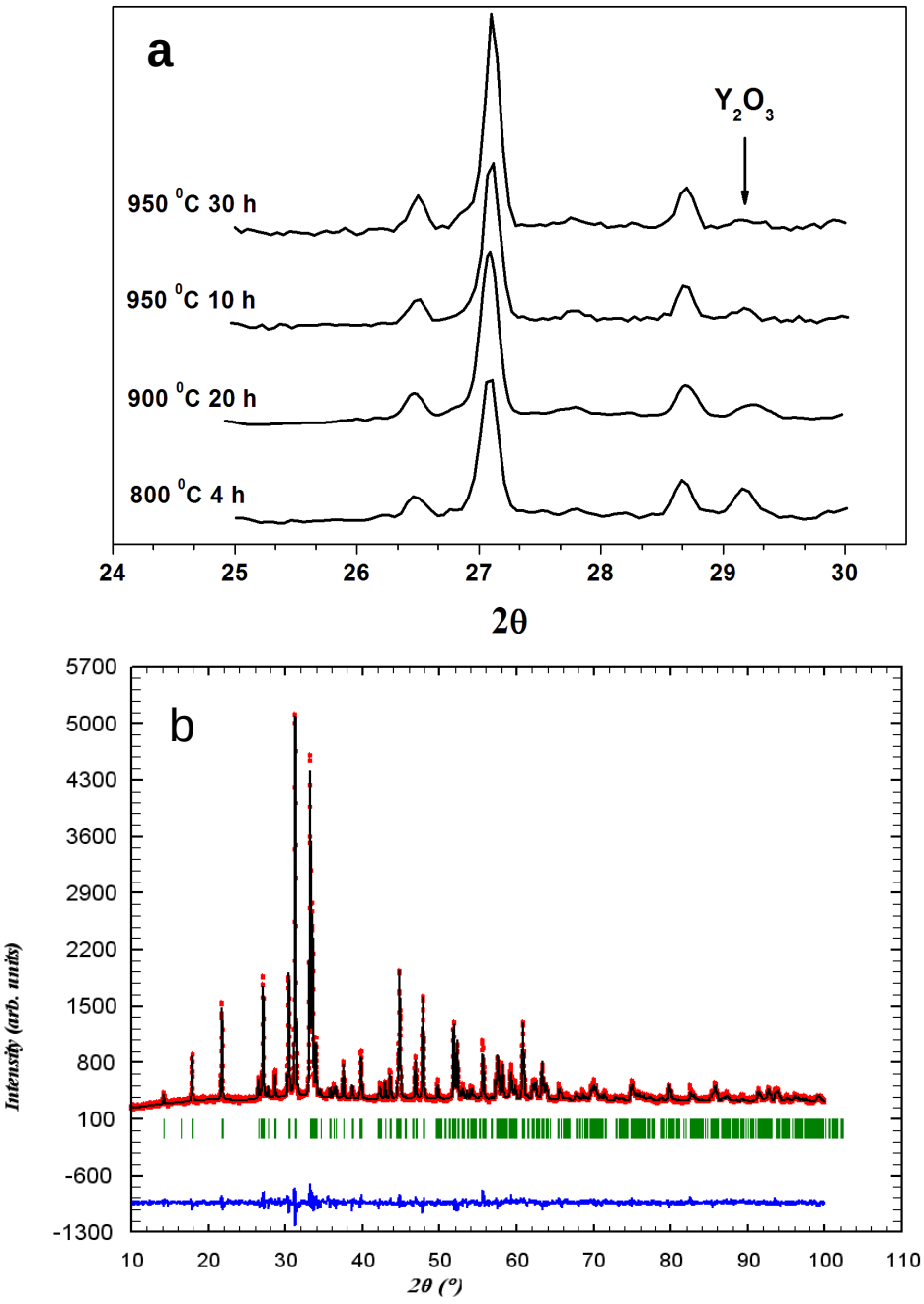

Figure 4.1. XRD analysis of the S1 sample prepared by SSR: **(a)** low-angle XRD patterns taken at different stages of heat treatment. The arrow shows the position of the most intense Y_2O_3 peak at 29.2º 2θ. **(b)** The Rietveld refinement of the diffraction pattern taken from the final specimen after 74 h of annealing. The dots and the line represent the observed and calculated patterns, respectively. Vertical bars indicate the peak positions corresponding to the $Y_2Cu_2O_5$ structure, while the bottom line represents the difference between the observed and calculated patterns.

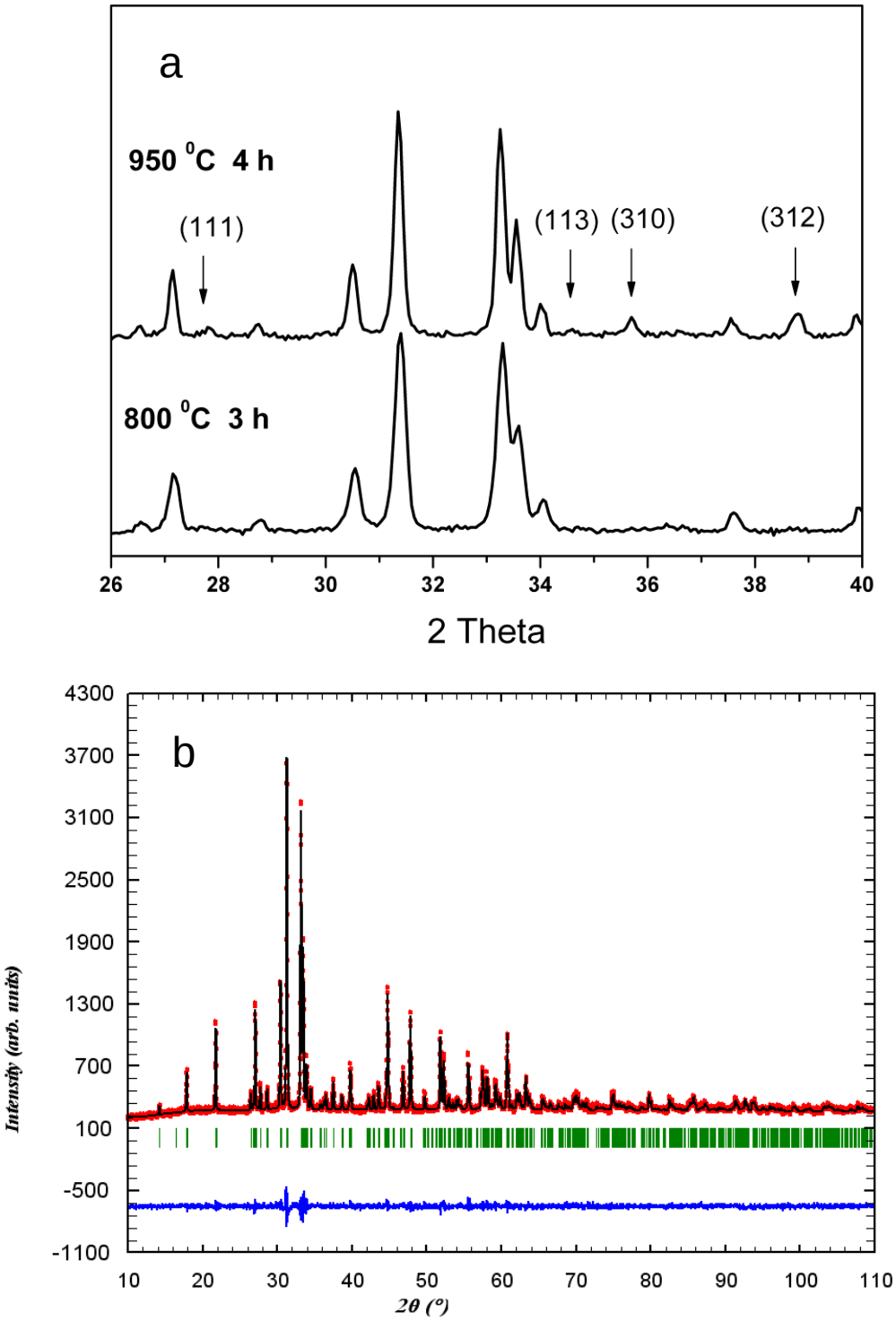

Figure 4.2. XRD analysis of the S2 sample prepared by GN route: **(a)** low-angle XRD patterns taken at different stages of heat treatment. The arrows denote the peaks that gradually develop with the annealing; **(b)** The Rietveld refinement of the diffraction pattern taken from the final specimen obtained after 31 h of annealing. The abbreviations have the same meaning as in Figure 4.1.

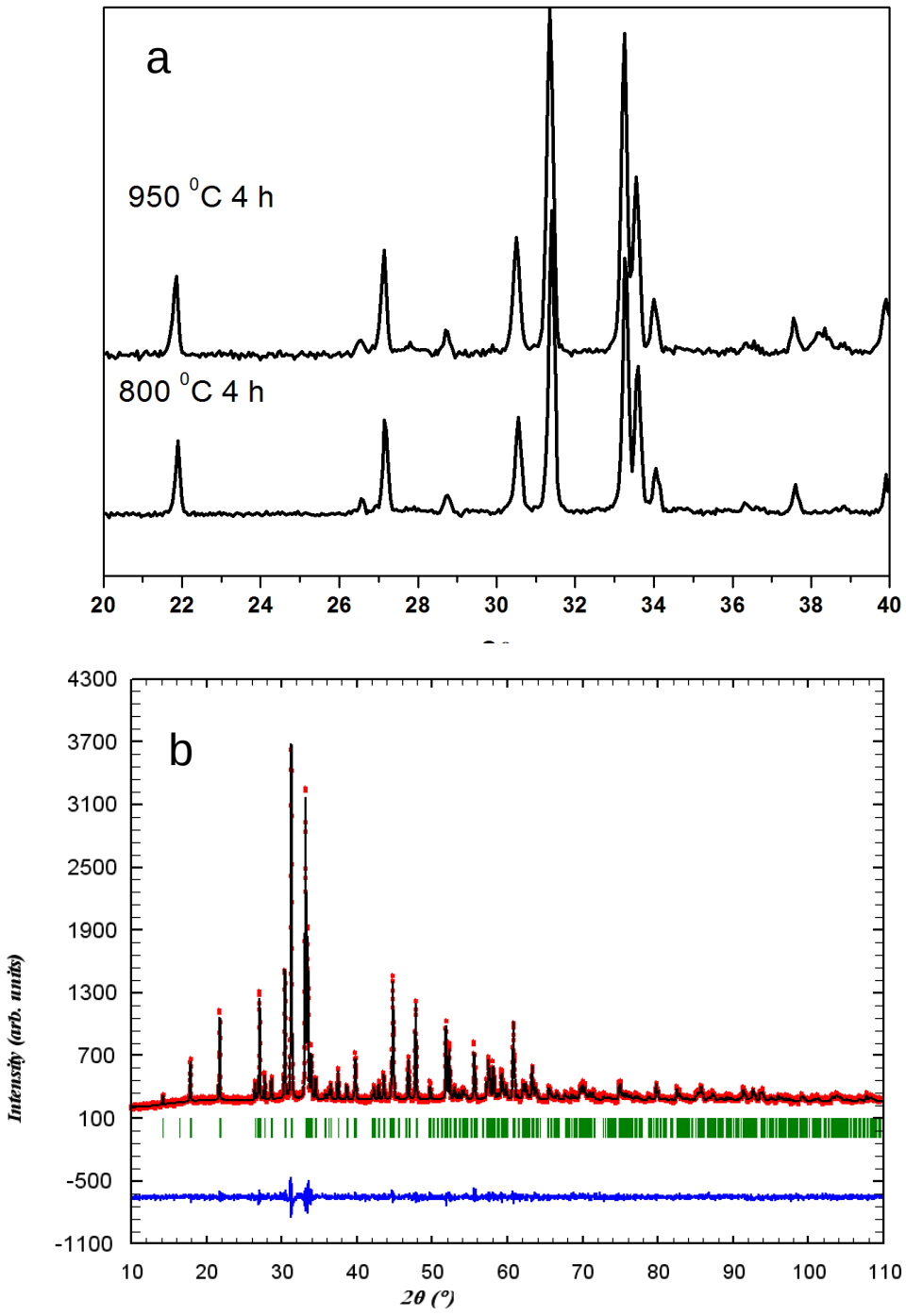

Figure 4.3. XRD analysis of the S3 sample prepared by SHS route: **(a)** low-angle XRD patterns taken at different stages of heat treatment. **(b)** The Rietveld refinement of the diffraction pattern taken from the final specimen after 12 h of annealing. The abbreviations have the same meaning as in Figure 4.1.

During the preparation of the S3 sample, the solution of metal nitrates and redox mixture in the molar ratio 1.01/0.28/1 (metal nitrates/glucose/KNO_3) was stirred for two hours at room temperature, and then continuously heated at 170 °C until the water completely evaporated and a paste-like residue was formed. This paste-like mass was formed into a cylindrical shape and ignited in normal atmospheric conditions (room temperature, air). The ignition initiated at one end of the cylinder launched a reaction which propagated towards the other end of the cylinder, leaving behind a dark-green powder. This powder was washed several times with distilled water, dried, and thereafter used as the precursor for further heat treatments in an oxygen flow: heating at 800 ^{0}C for 4 h, at 950 ^{0}C for 4 h and, finally, at 1050 ^{0}C for 4 h. Thus, the synthesis of $Y_2Cu_2O_5$ from the precursor obtained by the modified SHS took 12 h of sintering time.

4.2. Analysis of the crystal structure and magnetic properties

The Y/Cu ratio in the prepared samples was checked by the ICP-OES. In all samples the values of Cu and Y weight percentage were found to be within (24±0.4) w% and (34.2±0.6) w%, respectively, which corresponds to molar Cu/Y ratio of (1.01±0.03).

The crystallization process of $Y_2Cu_2O_5$ via three sintering routes was monitored by XRD (Figures 4.1a, 2a and 3a). In all samples the orthorhombic $Y_2Cu_2O_5$ phase was clearly formed after the initial heating at 800 ^{0}C, but a different content of other phases was also observed. The biggest issue in the preparation of the S1 sample by SSR was related to the presence of the Y_2O_3 phase, which was gradually reduced, albeit still present after 20 hours of sintering at 900 ^{0}C, and after additional 40 h at 950 ^{0}C. We found that the reduction rate of the Y_2O_3 content was appreciably slow in this case, and only after additional heating for 10 h at 1050 ^{0}C, the diffraction peaks of Y_2O_3 finally diminished below the XRD detection threshold. The difficulties in the Y_2O_3 removal are related to metallic oxides crystallization and their particle growth, which can run prior to, or concurrently with the solid state reaction, due to the low sintering temperature. The corresponding XRD pattern of the impurity-free sample was eventually used for the structure characterization by Rietveld refinement (Figure 4.1b).

The GN and SHS routes proved to be advantageous over SSR, since already after

the initial heating at 800 ^{0}C, no presence of Y_2O_3 could be detected (Figures 4.2a, 3a). Such an outcome may be understandable, knowing that both GN and SHS are fast combustion reactions, in which the processes of nitrates decomposition and compound formation run almost simultaneously. Thus, the subsequent thermal treatments, in case of these two methods, might be more accurately considered to be annealing processes, rather than being solid state reactions.

However, a careful inspection of the XRD patterns taken from the S2 and S3 samples during different stages of the annealing procedure revealed that, besides the absence of impurities, the $Y_2Cu_2O_5$ crystal structure (Figure 4.4a) showed an ability to "evolve" with temperature and annealing time. This was manifested through a gradual development of several low-intensity XRD peaks with annealing, which are otherwise absent in the patterns taken from the samples in an early stage of heat treatment, as indicated in Figure 4.2 (a). The changes in $Y_2Cu_2O_5$ XRD spectra, very much similar to our observations, were previously noticed by Horyn et al. [12], who were investigating the temperature and annealing duration influence on the occurrence of the magnetic anomaly at 6 K. They ascribed these subtle changes in the diffraction pattern to the occurrence of a specific type of Cu disorder within a $Y_2Cu_2O_5$ unit cell. Namely, besides the two non-equivalent Cu sites in a unit cell (Cu1 and Cu2, see Table 4.1 and Figure 4.4a), the existence of two additional Cu sites was proposed (Cu1' and Cu2', Figure 4.4b), with the assumed drift directions Cu1↔Cu1' and Cu2↔Cu2', both along ***b***-axis (by approximately 1/6 ***b***) [12]. It was postulated that random distribution of Cu ions over these positions could be the most probable cause of the absence of both the magnetic anomaly at 6 K and the mentioned low-intensity diffraction peaks [11, 12].

Although the magnitude of the proposed Cu ion displacement causes only slight changes in an XRD pattern, the oxygen coordination polyhedron changes substantially, from the original distorted square-planar tetrahedron to a trigonal bipyramid (Figure 4c) [11, 12]. Due to the complex pathways of the exchange mechanism in $Y_2Cu_2O_5$, it is reasonable to assume that the mentioned Cu displacement can have noticeable impact on its magnetic properties, thus making these properties dependent on the particular synthesis procedure applied.

Table 4.1. Crystal structure parameters for S1, S2 and S3 samples from Rietveld refinement

		S1	S2	S3
Y1	*x*	0.0462(6)	0.0459(8)	0.0438(9)
	y	0.227(1)	0.224(1)	0.220(1)
	z	0.3297(2)	0.3295(3)	0.3299(3)
Y2	*x*	0.2105(7)	0.2103(8)	0.209(1)
	y	0.224(2)	0.223(2)	0.224(1)
	z	0	0	0
Cu1	*x*	0.494(1)	0.492(1)	0.493(1)
	y	0.844(5)	0.836(5)	0.830(4)
	z	0.111(1)	0.114(2)	0.111(1)
	Occ.	**0.81(2)**	**0.90(2)**	**1.00(2)**
Cu1'	*x*	0.494(1)	0.492(1)	0.493(1)
	y	0.664(6)	0.651(6)	0.647(5)
	z	0.111(1)	0.114(2)	0.111(1)
	Occ.	**0.19(2)**	**0.10(2)**	**0**
Cu2	*x*	0.267(1)	0.264(1)	0.266(1)
	y	0.664(6)	0.651(6)	0.647(5)
	z	0.214(1)	0.218(1)	0.213(1)
	Occ.	**0.76(3)**	**0.81(3)**	**0.94(2)**
Cu2'	*x*	0.267(1)	0.264(1)	0.266(1)
	y	0.844(5)	0.836(5)	0.830(4)
	z	0.214(1)	0.218(1)	0.213(1)
	Occ.	**0.24(3)**	**0.19(3)**	**0.06(2)**
O1	*x*	0.161(3)	0.178(3)	0.166(4)
	y	0.731	0.731	0.731
	z	0.350(1)	0.351(1)	0.351(1)
O2	*x*	0.322(4)	0.328(4)	0.326(4)
	y	0.722	0.722	0.722
	z	0.066(1)	0.061(1)	0.064(1)
O3	*x*	0.126(6)	0.118(5)	0.119(5)
	y	0.331	0.331	0.331
	z	0.162	0.162	0.162
O4	*x*	0.432(4)	0.433(4)	0.431(5)
	y	0.780	0.780	0.780
	z	0.263	0.263	0.263
O5	*x*	0.426(3)	0.409(3)	0.432(4)
	y	0.227	0.227	0.227
	z	0.473	0.473	0.473

Table 4.2. Unit cell parameters for S1, S2 and S3 samples from Rietveld Refinement

		S1	S2	S3
Cell parameters (Å)	***a***	10.8036(3)	10.8106(4)	10.8068(3)
	b	3.4969(1)	3.4993(1)	3.4984(1)
	c	12.4588(4)	12.4625(4)	12.4607(4)
Cell volume ($Å^3$)		470.68(2)	471.45(3)	471.10(2)
Rp		3.52	3.69	3.75
Rwp		4.46	4.65	4.72
Rp*		3.85*	3.80*	3.75*
Rwp*		4.95*	4.76*	4.72*

(*) R-factors obtained by the standard structure model

The refined diffraction patterns of S1, S2 and S3 are shown in Figures 4.1b, 2b, and 3b, respectively, while the final results of the refinement are listed in Table 4.1. The starting parameter values were taken from [6], with the exception of the two additional Cu positions (Cu1' and Cu2') that were chosen in the manner introduced in [12]. Having in mind the similarities in evolution of our XRD pattern(s) with those observed in [12], and their correlation with the appearance of 6 K magnetic anomaly, the use of such structure model was physically the soundest choice. However, some points must be stressed regarding this model:

(i) it improves standard model only in a minor part of diffraction pattern by taking into account a limited set of low-intensity peaks,

(ii) it comprises a stringent constrain on Cu occupation numbers: occCu1 + occCu1' =1, and occCu2 + occCu2' =1.

Table 4.3. Bond lengths in Cu-O polyhedra and Cu-Cu distances.

	S1	S2	S3
Cu1 -O2	1.99(5)	1.91(4)	1.94(6)
-O3	2.81(4)	2.71(3)	2.71(4)
-O3	2.00(5)	1.89(4)	1.93(5)
-O4	2.02(2)	2.00(2)	2.00(3)
-O5	2.01(2)	2.03(2)	2.04(2)
Cu2 -O1	1.98(3)	1.94(3)	1.97(3)
-O2	1.96(3)	2.02(3)	1.98(3)
-O3	2.05(5)	2.10(4)	2.07(5)
-O3	2.80(4)	2.89(3)	2.92(4)
-O4	1.94(4)	1.98(4)	1.92(6)
Cu1'-O2	1.92(5)	1.87(4)	1.93(6)
-O3	2.33(5)	2.18(4)	2.22(5)
-O3	2.42(5)	2.35(3)	2.38(4)
-O4	2.05(2)	2.05(2)	2.05(3)
-O5	2.03(2)	2.07(2)	2.08(2)
Cu2'-O1	2.04(3)	1.98(3)	1.98(3)
-O2	2.03(3)	2.07(3)	2.00(3)
-O3	2.44(5)	2.50(3)	2.48(5)
-O3	2.32(5)	2.45(3)	2.44(5)
-O4	1.90(4)	1.93(4)	1.87(6)
Cu1 -Cu2	2.838(19)	2.843(19)	2.825(18)
Cu1'-Cu2	2.768(18)	2.766(18)	2.754(18)
Cu1'-Cu1	0.63(3)	0.66(3)	0.63(2)

The refined patterns showed very good agreement with the experimental data with profile reliability factors (R_{wp}) of less than 5 %. It can be seen from Table 1 that the values of the atomic coordinates and cell parameters of all samples are, within the error limits, close or equal, and in accordance with previously reported XRD analyses on both single crystal and powder specimens [1, 8, 9, 12]. Though in a much narrower range than reported in literature (467.93 - 472.88 $Å^3$), a small deviation in cell volumes of the three samples can

be observed (i.e. max. 0.8 $Å^3$, or 0.2%). This could be considered as a consequence of their different crystal densities (concentrations of defects and imperfections), due to the different dynamics of chemical reactions and the duration of thermal treatments.

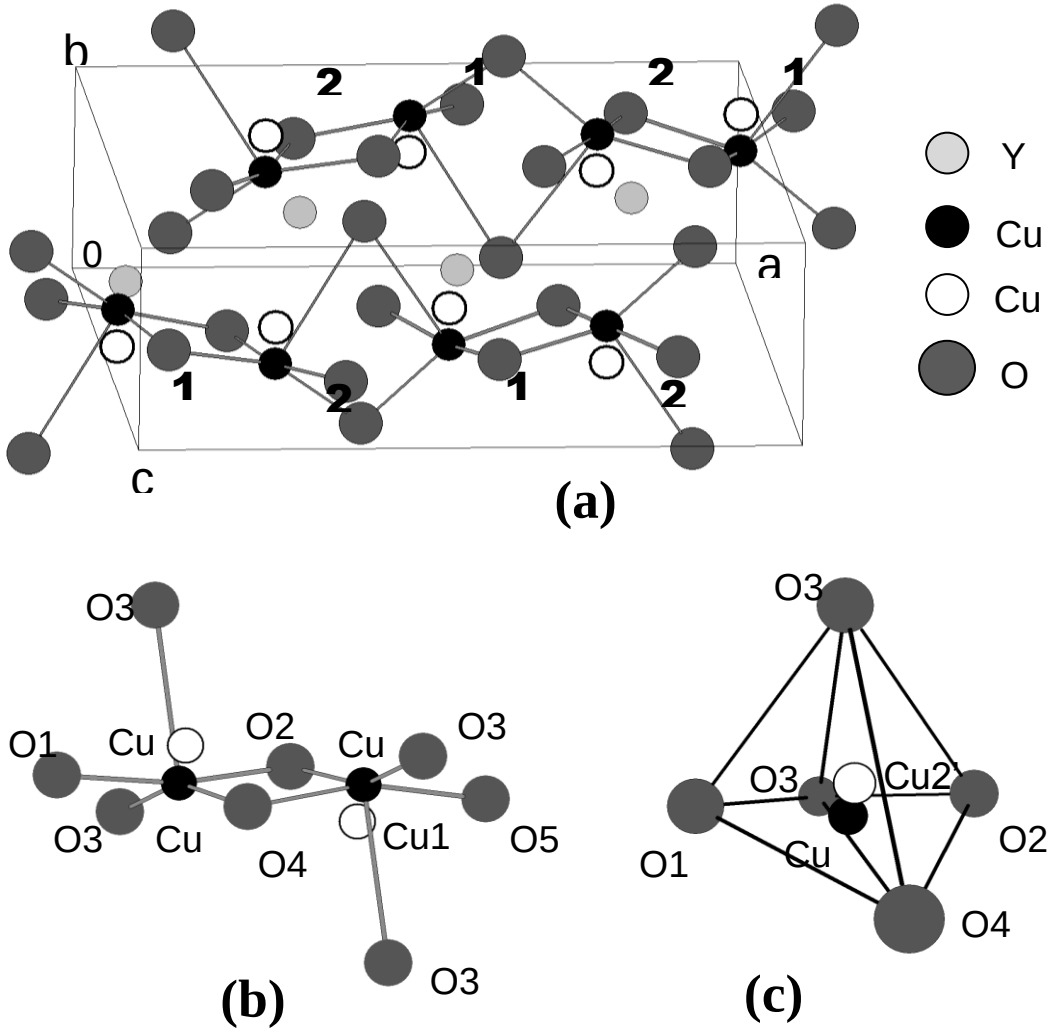

Figure 4.4. (a) $Y_2Cu_2O_5$ unit cell showing Cu-dimmer chains, (b) a detailed configuration of Cu-dimmer, and (c) Cu2-Cu2' coordination polyhedron as the trigonal bipyramid

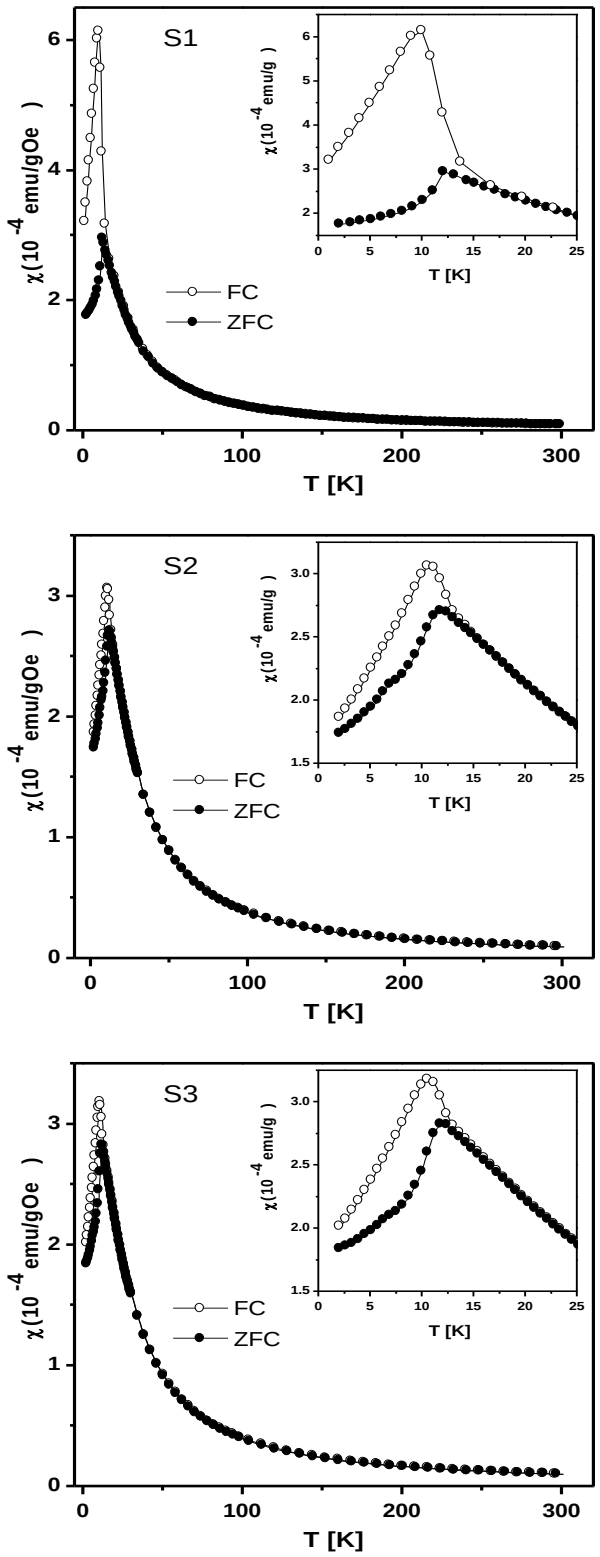

Figure 4.5. The ZFC and FC magnetic susceptibility dependence on temperatures between 2 K and 300 K. Insets: susceptibility behavior in the low-temperature region 2-25 K.

The coordination distances around Cu ions in all four positions are also calculated, and their values are summarized in Table 4.2 and Table 4.3. It should be noted, however, that some of the oxygen coordinates had to be fixed during the refinement, due to their large standard deviations (lower sensitivity of XRD to oxygen). This prevented us to accurately observe the exact changes in all Cu-O bond lengths and angles. However, the Cu coordinates and Cu distribution over the available positions Cu1, Cu2, Cu1', and Cu2' (i.e. their occupation numbers) were successfully determined for all samples. These results indicated a different degree of Cu disorder in three samples, despite the similarities in the XRD patterns.

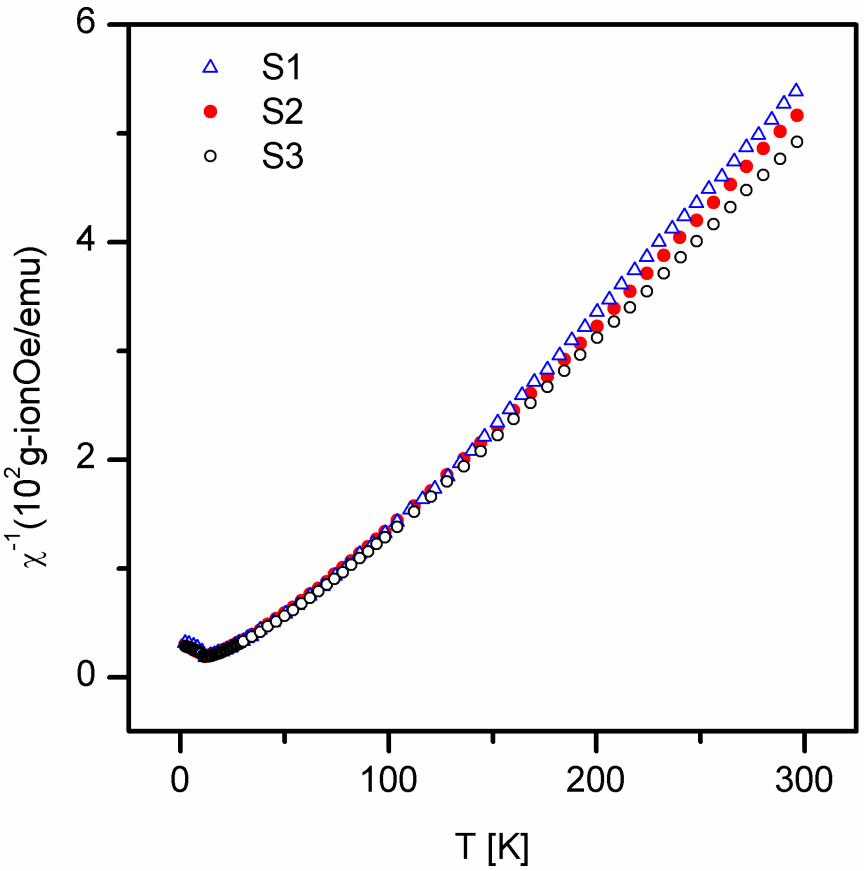

Figure 4.6. Inverse gram-ion magnetic susceptibility of the samples between 2 K and 300 K.

The biggest deviation from the nominal Cu1 and Cu2 site occupations was detected in the S1 sample. Based on the refinement results, this deviation was estimated to be around

20% in both positions (Table 4.1), while it was 10% in S2, and was almost completely absent in S3 sample. In this sample only a small fraction (about 5%) of copper ions from Cu2 was found in the Cu2' position, and in general, a somewhat higher tendency towards

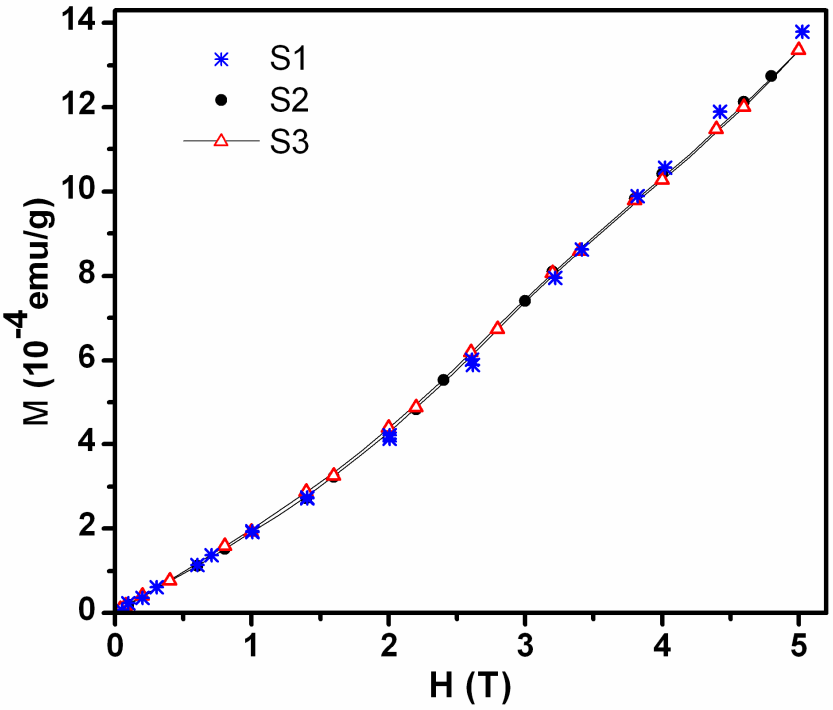

Figure 4.7. The dependence of isothermal magnetization on magnetic fields between 0 T and 5 T, at 5 K. The number of data points is reduced and the full line is added as a guide for an eye.

cationic disorder between the Cu2 and Cu2' positions was found in all samples.

In addition to the proposed structure model, we also refined the XRD data by the standard structure model for $Y_2Cu_2O_5$ [6] (i.e. without assuming the existence of Cu disorder). This approach resulted in no significant change of structure parameters and small increment in R-values (marked with asterisk in Table 4.2). Increased R-values were obtained in case of S1 (~10%) and S2 (~4%), while no difference in the R-values for the S3 sample was detected, since the absence of Cu disorder in S3 implies that two structure models are equivalent for that sample. The obtained differences in R-values were relatively small for all the samples, due to the above stressed properties of the "Cu-drift" model.

To check the influence of these structural factors on the magnetic properties of $Y_2Cu_2O_5$, we performed the magnetic characterization of all samples in a DC magnetic field, within 2-300 K temperature range. From previous reports, it is known that $Y_2Cu_2O_5$ shows anti-ferromagnetic transition at $T_N \approx 13$ K [22, 23]. It is also known that the relatively large and positive Curie-Weiss temperature of $\theta = 38.5$ K indicates a considerable contribution of ferromagnetic interaction [1-4, 10-12]. Moreover, below T_N, this compound exhibits two metamagnetic transitions in magnetic fields up to 5 T [1-4]. The results of the magnetic susceptibility measurements versus temperature are shown in Figure 4.5. The susceptibility was recorded after two cooling regimes: the ZFC (zero field-cooled) regime, when the sample was cooled down to 2 K without the presence of a magnetic field, and the FC (field-cooled) regime, when the sample was cooled in the presence of the measuring magnetic field. The magnetic anomaly at 6 K, which was previously reported to exist only in crystals with highly ordered Cu sublattice and in weak magnetic fields (up to 200 Oe) [11, 12], was detected in samples S2 and S3 (in the ZFC regime).

However, in this study, we were able to observe this anomaly in S2 and S3 in somewhat stronger measuring fields, up to 300 Oe (Figure 4.5b, c). At the same time, the anomaly was not detected in S1 even in a field of 100 Oe (Figure 4.5a). These results seem to correlate with the highest degree of Cu disorder found in S1 by the structure analysis, and support the conclusions in [12] that the absence of the 6 K anomaly is related to this type of disorder.

The analysis of the high-temperature part of the inversed susceptibility (Figure 4.6), between 160 K and 300 K, confirmed that it followed the Curie-Weiss law for all samples. The values of the Curie-Weiss temperature θ for S1, S2 and S3 were found to be close within the error limits, (37±2) K, (38±1) K and (35±1) K, indicating a similar degree of ferromagnetic contribution in all samples. The calculated values of Cu^{2+} effective magnetic moment were determined as (1.976±0.004) μ_B for S1, (2.001±0.003) μ_B for S2, and (2.066±0.003) μ_B for S3 (Figure 6). These values are rather high compared to the spin-only value of 1.73 μ_B, but are in accordance with previously reported results [22, 23]. Such enhancement of Cu magnetic moment in this material is consistent with the presence of ferromagnetic interaction within Cu-dimmers that persists at higher temperatures ($T > 35$

K) [22].

Besides the presence of the 6 K anomaly, the low-temperature magnetic susceptibility (Figure 4.4, insets) also pointed to additional differences between the investigated samples: (i) the separation of the ZFC and FC curves below antiferromagnetic transition at 12 K, and (ii) the discrepancy between the ZFC and FC antiferromagnetic transition temperatures, with the FC maximum being shifted down by approximately 1 K. Both of these features point to the already known sensitivity of $Y_2Cu_2O_5$ to magnetic field [1] but this, again, was most pronounced in the S1 sample. While the ZFC susceptibility values were very close in all the samples, the FC susceptibility in S1 was found to be approximately twice as large as in the other two samples, indicating a higher degree of spin canting during the FC. Such behavior of this sample suggests the presence of other structure factors that could influence its magnetic properties in addition to the described Cu disorder. Despite the fact that XRD showed no presence of impurity phases (Y_2O_3 or CuO), it could be suspected that the sintering time of about 3 days was too short for proper crystallization of S1 sample, which implies the presence of higher concentration of structure defects than in other two samples. These defects weaken local coupling of Cu moments and thus enable easier spin canting during the FC.

In contrast to the differences in low-intensity magnetic field, the isothermal magnetization dependence on the fields up to 5 T appears identical for all samples at 5 K (Figure 4.7). The magnetization curve is indicating two metamagnetic transitions with the change of slope that is, as expected, less pronounced than in case of a single crystal with an easy b-axis oriented parallel to the field [1-4]. The critical fields in our case could be estimated to be around 2.5 T and 4 T, which is somewhat lower than the values of 2.8 T and 4.7 T reported for single crystal in [1, 2].

References

1. S.W. Cheong, J.D. Thompson, Z. Fisk, K.A. Kubat-Martin, E. Garcia, Phys. Rev. B 38 (1988) 7013-7015.
2. Y. Matsuoka,Y. Nishimura, S. Mitsudo, H. Nojiri, H. Komatsu, M. Motokawa, K. Kakurai, K Nakajima, Y. Karasawa, N. Niimura, Journal of Magnetism and

Magnetic Materials 177-181 (1998) 729-730.

3. M. Motokawa, K. Kita, H. Shibazaki, H. Ohta, W. J. Jang, M. Hasegawa, H. Takei, Physica B, 211 (1995) 165-167.
4. R. Szymczak, H. Szymczak, M. Baran, R.Z. Levitin, B.V. Mill, Journal of Magnetism and Magnetic Materials, 157/158 (1996) 667-668.
5. U. Adem, G. Nenert, Arramel, N. Mufti, G.R. Blake, and T.T.M. Palstra, Eur. Phys. J. B, 71 (2009) 393-399.
6. H. Fjellvag, P. Karen and A. Kjekshus, Acta Chem. Scand. A, 42 (1988) 144-147.
7. J. L. Garcia- Munoz and J. Rodrguez-Carvajal, Journal of Solid State Chemistry, 115 (1995) 324-331.
8. R.D. Adams, J.A. Estrada, T. Datta, Journal of Superconductivity 5(1) (1992) 33-38.
9. R. Famery and F. Queyroux, Materials Research Bulletin, 24 (1989) 275-281.
10. I. V. Paukov, M.N. Popova, J Klamut, Physics Letters A, 189 (1994) 103-108.
11. R. Horyn, J. Klamut, M. Wolcyrz, A. Wojakowski, A. J. Zaleski, Journal of Magnetism and Magnetic Materials, 140-144 (1995) 1575-1576.
12. R. Horyn, J. Klamut, M.Wolcyrz. A. Wojakowski, A.J. Zaleski, Physica B, 205 (1995) 51-58.
13. Ahmed M. Gadalla and Paisan Kongkachuichay, J. Mater. Res., 6(3) (1991) 450-454.
14. A. J. S. Machado and R. F. Jardim, Materials Letters, 19 (1994) 177-183.
15. Atit Bhargava, Jose A. Alarco, Graeme J. Millar, Robert Bell, Toru Yamashita, Ian D. R, Mackinnon, Materials Letters, 26 (1996) 89-96.
16. L.A. Chick, L.R. Pederson, G.D. Maupin, J.L. Bates, L.E. Thomas, G.J. Exarhos, Material Letters, 10 (1990) 6-12.
17. Ana Mrakovic, Jovan Blanusa, Darinka Primc, Marija Perovic, Zvonko Jaglicic, Vladan Kusigerski, Vojislav Spasojevic, Ceramics Internationa, l 39 (2013) 3771-3777.
18. A.G. Merzhanov, Journal of Materials Chemistry, 14 (2004) 1779–1786.
19. A.G. Merzhanov, I.P. Borovinskaya, International Journal of Self-propagating

High-temperature Synthesis, 17 (2008) 242–265.
20. Juan Rodríguez-Carvajal, Physica B: Condensed Matter, 192 (1993) 55-69.
21. H. Fjellvag, P. Karen and A. Kjekshus, Acta Chem. Scand. A, 41 (1987) 283-293.
22. B.L Ramakrishna, E.W. Ong and Z. Iqbal, Solid State Communications, 68 (1988) 775-779.
23. R. Troc, Z. Bukovski, R. Horyn and J. Klamut, Phys. Lett. A, 125 (1987) 222-224.

5. Influence of Cu substitution on magnetic properties of $Y_2Cu_2O_5$

Due to a plethora of magnetic properties $Y_2Cu_2O_5$ represents a convenient system for investigation of ion substitution impact on the underlying magnetism. While several studies on the yttrium substitution in $Y_2Cu_2O_5$ have been reported [11-17], the Cu ion substitution was the subject of only one study so far [10], and its consideration was limited to temperatures above 75 K i.e. to the paramagnetic region. Consequently effects of Cu dilution on the $Y_2Cu_2O_5$ crystal structure and especially the impact on its low-temperature magnetic properties and metamagnetism have remained completely unknown.

In previous chapter, we have discussed about new approach to $Y_2Cu_2O_5$ synthesis which utilized a modified self-propagating high-temperature (SHS) reaction and on the influence of a subsequent heat treatment to copper sublattice disorder and magnetic properties of the pure material. In this chapter we will consider the use of the same preparation route for the synthesis of $Y_2Cu_2O_5$ in which Cu ions are partially substituted by nonmagnetic Mg ions, and on the structure and magnetic investigation on so-obtained samples. Quiang et al. [10] have shown that it is possible to obtain single phase solid solutions with magnesium concentrations up to 15 %, and here we present our study on $Y_2(Cu_{1-x}Mg_x)_2O_5$ solid solutions with x=0.0, 0.05, 0.15 in the 2-300 K temperature range.

5.1 Sample preparation and measurements

The polycrystalline samples of $Y_2Cu(_{1-x}Mg_x)_2O_5$ with magnesium concentration x = 0.0, 0.05, and 0.15 denoted as S0, S5 and S15 respectively, were synthesized by a modified SHS method, in accordance with results from our previous study on $Y_2Cu_2O_5$ preparation discussed in previous chapter and reported in [18]. Metal nitrates i.e. yttrium-nitrate $Y(NO_3)_3$, copper-nitrate $Cu(NO_3)_2$ and magnesium-nitrate $Mg(NO_3)_2$ served as a source of metal ions, while the energy for precursor formation is drawn from combustion of a redox mixture composed of $C_6H_{12}O_6$ and potassium nitrate.

All components were dissolved in distilled water. The solution of nitrates and redox mixture were dried at 120°C to form a gel. The dry gel was molded into a cylindrical shape while warm, cooled down and ignited at one end in air by means of an open flame. After the burning reaction has terminated at the other end of the cylinder, the combustion product in the form of a dark green powder was washed several times with distilled water to remove traces of K_2CO_3, and afterwards dried at 70 º C. The resulting powder was than grinded in an agate mortar, and so-obtained precursor powder was heated at 1050 ºC for 24 h.

The only difference regarding SHS procedure from the previous case is in prolonged annealing: the obtained precursor powder was heated at 1050 ºC for 24 h. The reason for this was to stay on the safe side; although we have shown that SHS procedure is capable of providing proper crystalline $Y_2Cu_2O_5$ sample in just 12 h, we have conducted 24 h annealing in order to ensure that final samples do not contain any Cu ion drifted from their standard crystallographic positions.

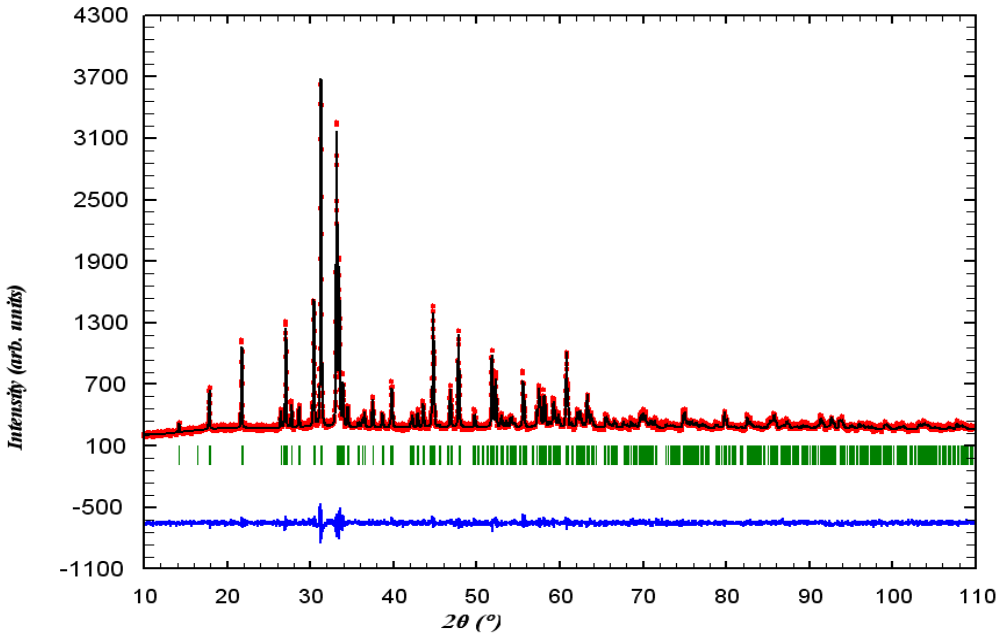

Figure 5.1: The refined diffraction pattern of S5 sample. Points represent the experimental data, full line corresponds to the Rietveld fit, the bottom line is the difference between the fit and experimental data, and the vertical bars correspond to reflection positions.

The patterns were recorded in the 15º-110º 2θ range with the 0.05 º step size and 15 s/step of exposure time. The obtained X-ray data were refined by the Rietveld full-profile method [19] with the application of the FULLPROF software package [20]. The temperature dependence of magnetization was measured in the temperature range 2-300 K and in the applied field of 300 Öe. The isothermal dependence of magnetization on external magnetic field was measured at 2K in the field range 0 T < H < 5 T.

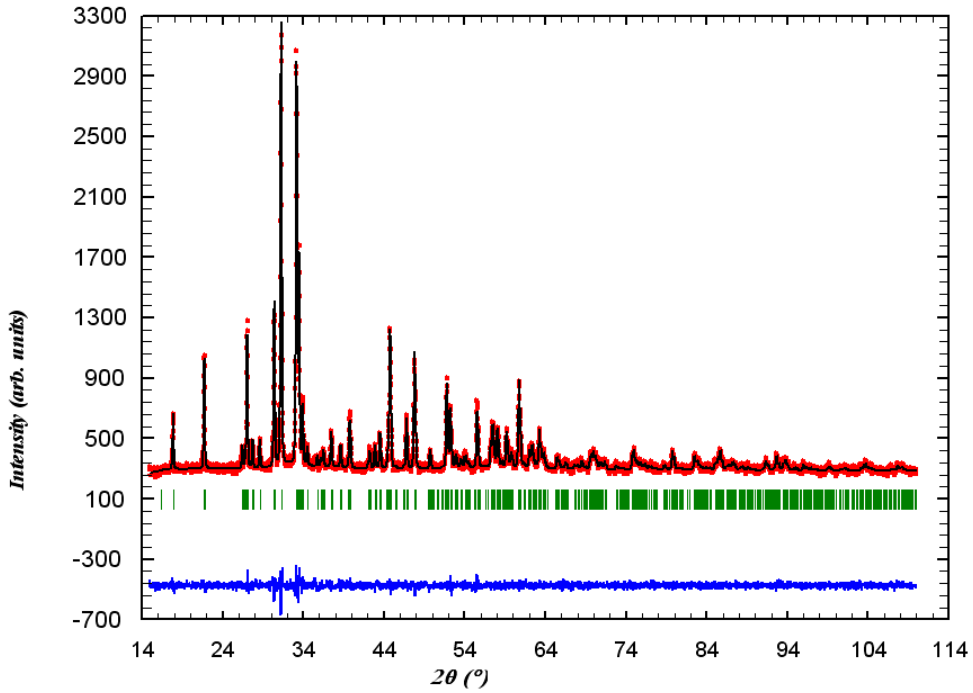

Figure 5.2: The refined diffraction pattern of S15 sample. Points represent the experimental data, full line corresponds to the Rietveld fit, the bottom line is the difference between the fit and experimental data, and the vertical bars correspond to reflection positions.

5.2. Results and discussion

We have already seen from the previous case of pure $Y_2Cu_2O_5$ study (chapter 4) that crystal structure properties play the key role in shaping its magnetic properties. The crystal

structure of pure $Y_2Cu_2O_5$ was comprehensively studied by other authors as well [5-8], despite the problems regarding slow crystal growth, crystal quality and consequential variations in structure parameters. This is quite expected, knowing that, the most characteristic feature of the crystal structure – the presence of infinite Cu-O chains along

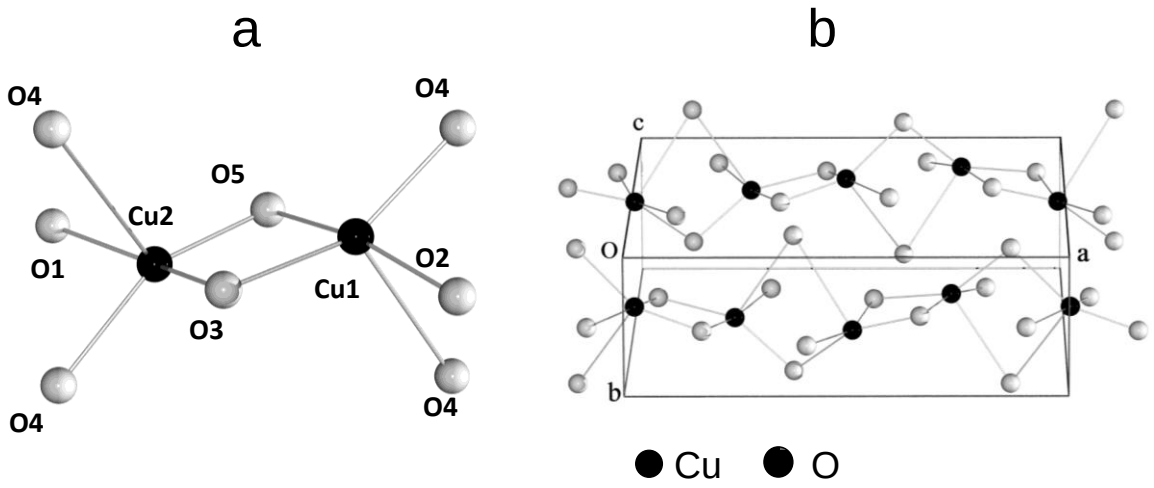

Figure 5.3: the detailed description of Cu dimmer unit in details (a), and Cu-O dimmer chains within the $Y_2Cu_2O_5$ unit cell (b).

the a-axis, forces intrachain ferromagnetic (FM) coupling of Cu^{2+} ions, while the interaction between neighboring chains is antiferromagnetic (AFM) [9]. What decides on final $Y_2Cu_2O_5$ magnetic behavior is the fact that despite considerably stronger FM intrachain interaction, it is the weak interchain interaction that eventually causes the emergence of 3D AFM ordering below 12 K. The complex balance between two type of interactions is found to be temperature dependant [9, 10], and finally results in metamagnetic behavior below 12 K.

One of the main goals of this study is to determine weather Cu substitution introduces changes in structure parameters and how those changes can be related to magnetic properties. Thus, special attention will be paid to any changes in the main interaction paths formed by Cu_2O_8 dimmers as shown in Fig. 2 (a). Through bridging oxygen ions (O4), dimmers form an infinite zig-zag Cu_2O_8 copper-oxygen chains, Fig. 2(b) [7]. Concerning magnetic interactions, it should be noted that the most favorable

superexchange paths are over the oxygen bridge formed by O3 and O5 ions, due to shortest Cu-O-Cu bond lengths in $Y_2Cu_2O_5$ structure and bond angles very close to 90º. According

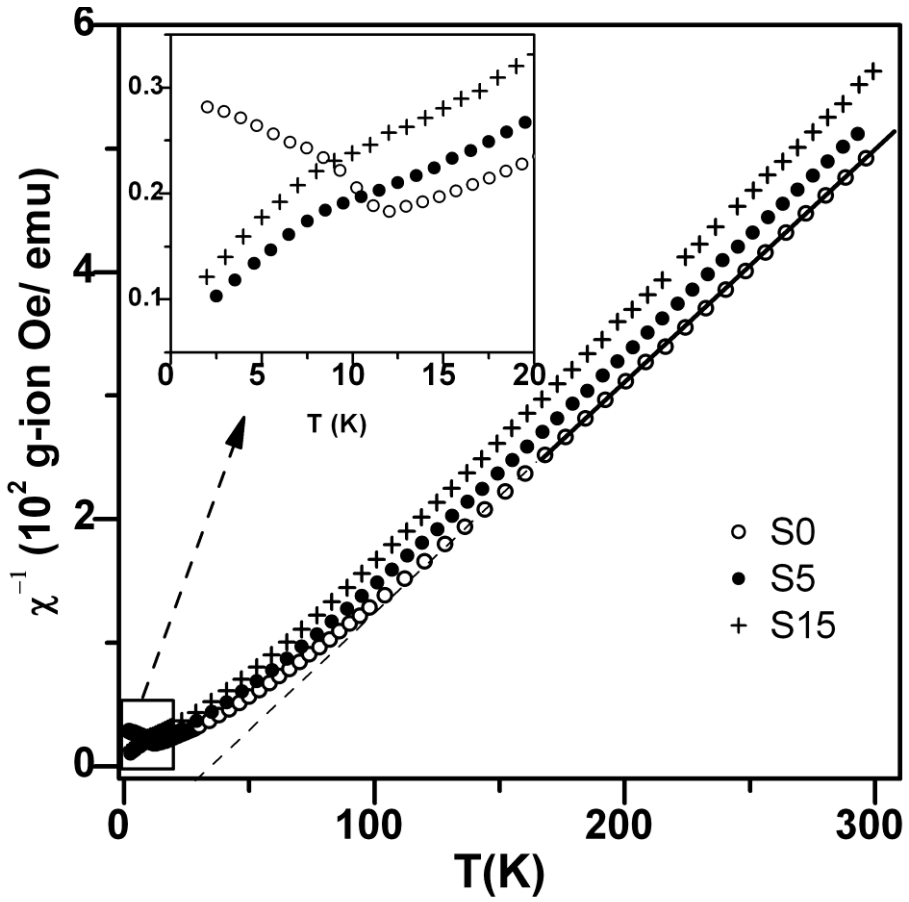

Figure 5.4. Inverse gram-ion magnetic susceptibility for S, S5 and S15 samples between 2 K and 300 K. All data show linear dependence above 150 K. Inset: the magnified part of the graph below 25 K.

to Goodenough-Kanamori rules [21] such arrangement leads to ferromagnetic interaction between Cu^{2+} ions. Oxygen bridges over O4 ions that connect Cu dimmers in infinite 1D chains also promote FM interactions but of the weaker strength due to longer bond lengths and angles deviating from ideal 90º.

The XRD diffraction patterns taken from all samples indicate a single phase orthorhombic $Y_2Cu_2O_5$, which was confirmed by detailed analysis of the crystal structure by Rietveld full profile method [19]. As an example, the refined diffraction patterns of S5 and S15 samples are shown in Figures 5.1 and 5.2, respectively.

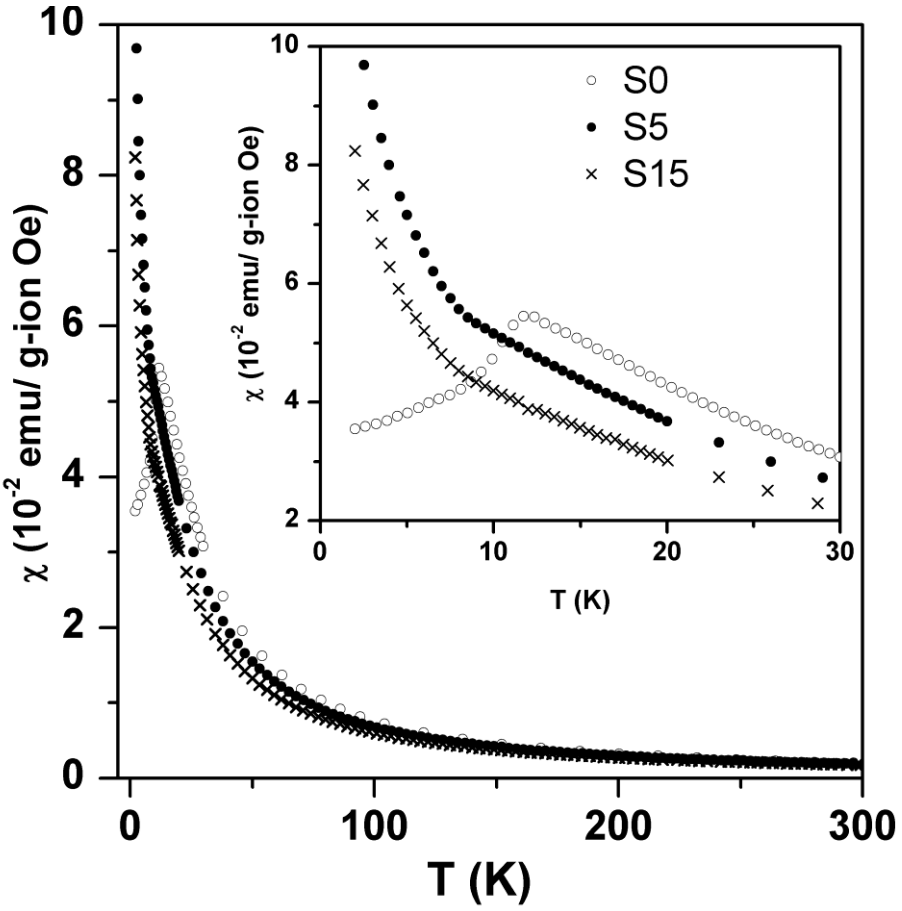

Figure 5.5 The ZFC gram-ion magnetic susceptibility dependence vs. temperature between 2 K and 300 K. Inset: the magnified part of the graph below 30 K.

The values of refined structure parameters including cell parameters, atomic coordinates and Cu site occupancies are shown in Tables 1 and 2. We have demonstrated previously [18] that Cu ordering in $Y_2Cu_2O_5$ can be very sensitive to annealing time so that complete ordering can not be achieved in less than 12 h of annealing at 1050 °C. In this study the samples were annealed at 1050 °C for 24 h, and the Rietveld analysis of the S0 sample comprising Cu drift model [18, 22] has shown that all Cu ions occupy their nominal crystallographic positions Cu1 and Cu2.

It is interesting to note (see Table 1) that, within the error limits, Mg has shown higher preference in occupation of Cu2 site. An inspection of Table 1 also shows that partial substitution of Cu^{2+} (0.7 Å radius) by somewhat smaller Mg^{2+} ion (0.65 Å) did not

cause a significant change in cell volume, although a very small (around 0.1%) decrease in cell volume was found for sample S15. However, it can be seen from both Tables 1 and 2 that magnesium substitution did cause some changes in average atomic positions and therefore in Cu-O bond lengths and angles. It is reasonable to assume that such changes can influence important superexchange paths, especially the two intra-dimmer paths over O3 and O5 ions (Figure 2a). Of these, the exchange path with longer Cu(1,2)-O3 distances remained almost unchanged by Mg substitution. However, the more dominant path with

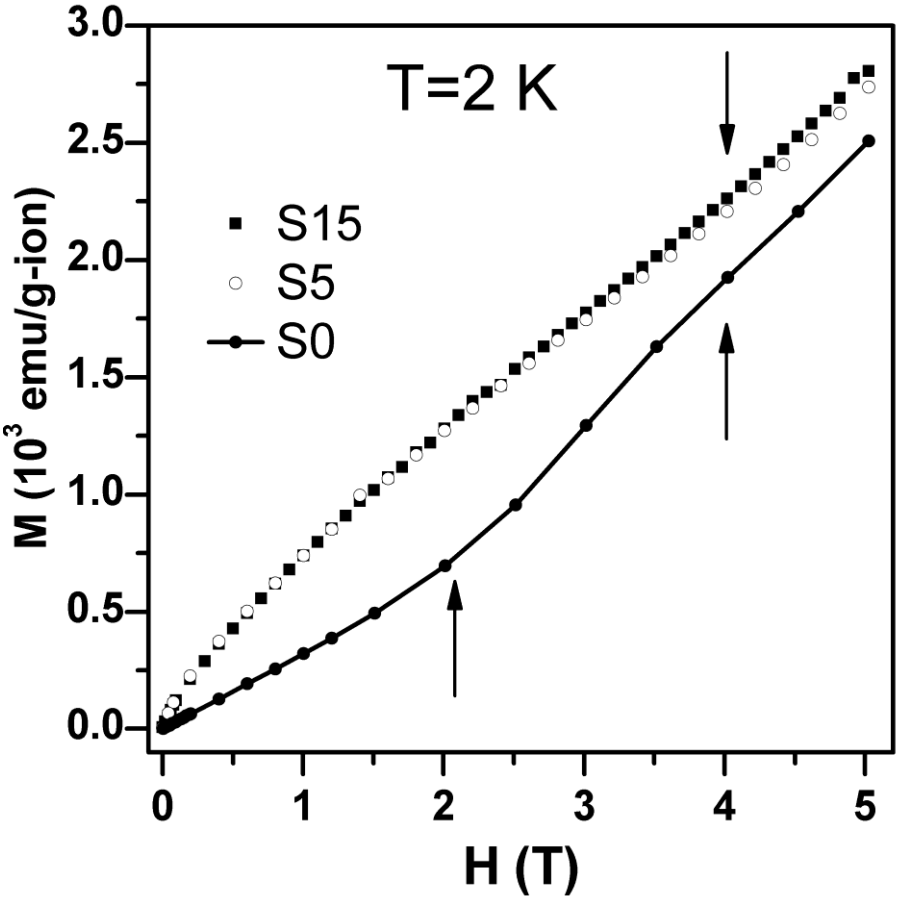

Figure 5.6.The dependence of isothermal magnetization at 2 K on magnetic fields between 0 T and 5 T. Arrows indicate metamagnetic transitions.

shorter Cu(1,2)-O5 distances is much more affected by Mg substitution, through the increase of the Cu1-O5-Cu2 bond angle away from ideal 90º, which may contribute to the weakening of the intradimmer ferromagnetic exchange.

We will first consider the effects of the magnetic ion dilution on the high temperature magnetic properties. The temperature dependence of the inverse gram-ion susceptibility χ^{-1} for all samples is depicted in Figure 5.4, in the whole temperature region 2-300 K. It turns out that above 150 K the magnetic susceptibility of all samples can be well described by the Curie–Weiss law with a positive Curie temperatures θ which is in agreement with the known paramagnetic behavior of pure $Y_2Cu_2O_5$ [9, 10, 23]. Values of θ decrease with increasing Mg concentration: 35 K (S0), 27 K (S5), and 18 K (S15), which indicates the weakening of ferromagnetic interactions. The obtained values of effective magnetic moment μ_{eff} per Cu^{2+} ion were 2.06 μ_B (S0), 2.04 μ_B (S5), and 2.0 μ_B (S15). μ_{eff} value for pure sample is considerably higher than the spin-only value of 1.7 μ_B, but it agrees with experimentally determined moment found in previous magnetic studies on $Y_2Cu_2O_5$ [9, 10, 23]. The cause of this increased effective moment originates from the intradimmer ferromagnetic correlations that persist even at elevated temperatures [24]. Decrease of μ_{eff} values for diluted samples is connected with the structural changes caused by Mg ions doping. As already explained above these changes affect intradimmer superexchange paths in a way that leads to decrease of ferromagnetic correlations.

Effects of Mg substitution for Cu should be more pronounced in the low temperature region due to 1D chain arrangement of Cu ions along the a-axis. Namely, Cu ions dilution leads to a breaking of infinite chains i.e. to their partial substitution by finite size chains. It has been shown that in a case of infinite magnetic chain breaking the finite-size chain effects lead to paramagnetic behavior [25, 26]. Indeed, effects of finite Cu chains can be observed at low temperatures as shown in Figs. 3 and 4. Pure $Y_2Cu_2O_5$ sample displays AF transition at $T_N \approx 12$ K which is in compliance with previous results [9, 23]. Contrary to this, both diluted samples instead of decrease show upturn of magnetic susceptibility at low temperatures (Figure 5.5, inset). Careful inspection of insets in Figs. 3 and 4 leads to a conclusion that low temperature peak in susceptibility is still present for both diluted samples but shifted to somewhat lower temperature of about 10 K. This might be a sign that 3D AFM ordering still persists in S5 and S15 samples but with lower T_N due to magnetic dilution.

Table 1: Crystal structure parameters for S0, S5 and S15 samples obtained by Rietveld refinement.

		S0	S5	S15
Y1	*x*	0.2087(1)	0.2046(8)	0.2037(6)
	y	0.7244(2)	0.77313(1)	0.7274(2)
	z	0.6667	0.6667	0.6590
Y2	*x*	0.0437(1)	0.0409(8)	0.0384(6)
	y	0.7205(1)	0.7278(1)	0.7222(2)
	z	-0.0034(3)	-0.0030 (3)	-0.0104(2)
Cu1	*x*	0.4924(1)	0.4911(1)	0.4891(1)
	y	0.3290(4)	0.3340(1)	0.3231(3)
	z	0.7777(1)	0.7782(2)	0.7739 (3)
	Occ.	**1.00**	**0.974(5)**	**0.992(4)**
Mg1	*x*	-	0.4911(1)	0.4891(1)
	y	-	0.3340(1)	0.3231(3)
	z	-	0.7782(2)	0.7739 (3)
	Occ.	**-**	**0.026(5)**	**0.008 (4)**
Cu2	*x*	0.2657(1)	0.2639(1)	0.2621(2)
	y	0.1470(5)	0.1609(1)	0.1520(3)
	z	0.8792(1)	0.8793(2)	0.8762(3)
	Occ.	**1.00**	**0.926(5)**	**0.752(4)**
Mg2	*x*	-	0.2639(1)	0.2621(2)
	y	-	0.1609(1)	0.1520(3)
	z	-	0.8793(2)	0.8762(3)
	Occ.	**-**	**0.074(5)**	**0.248(4)**
O1	*x*	0.1670(4)	0.1575(2)	0.1570(2)
	y	0.2310	0.2423	0.2423
	z	0.0182 (1)	0.0185	0.0185
O2	*x*	0.4300(2)	0.4312(2)	0.4401(2)
	y	0.7270	0.7106	0.7106
	z	0.1396	0.1418	0.1418
O3	*x*	0.3260(4)	0.3148(3)	0.3099 (3)
	y	0.2220	0.1992	0.1992
	z	0.7299(1)	0.7247(4)	0.7248
O4	*x*	0.1190(6)	0.1186	0.1406(4)
	y	0.8310	0.8069	0.8069
	z	0.8636(4)	0.8334	0.8334
O5	*x*	0.4310(5)	0.4215(3)	0.4085(2)
	y	0.2281	0.2730	0.2730
	z	-0.07033	-0.0710(4)	-0.0710

Table 5.2: Unit cell parameter

		P	M5	M15
Cell parameters (Å)	*a*	10.8068(3)	10.8080(3)	10.8009(4)
	b	3.4984(1)	3.4980(1)	3.4951(1)
	c	12.4607(4)	12.4661(3)	12.4699(5)
Cell volume ($Å^3$)		471.10(2)	471.300(2)	470.742(3)
Rp		3.75	3.68	3.80
Rwp		4.72	4.61	4.78

Table 2. Bond lengths in Y-O and Cu-O polyhedra (in Å), and the bond angles in the superexchange bridges within Cu dimmer (in degrees).

	S0	S5	S15
Y1 - O1	2.29(2)	2.37(2)	2.30(2)
-O2	2.32(2)	2.36(2)	2.46(3)
-O2	2.33 (2)	2.25(2)	2.23 (3)
-O3	2.30(1)	2.33(2)	2.32(2)
-O3	2.29(2)	2.15(3)	2.17(2)
-O4	2.27(2)	2.29 (4)	2.31(3)
Y2 - O1	2.18(1)	2.14 (1)	2.14(1)
-O1	2.24(4)	2.22(1)	2.26(1)
-O2	2.17 (2)	2.17 (1)	2.20(3)
-O4	2.27(2)	2.22(2)	2.27(2)
-O5	2.29(1)	2.34(3)	2.35(2)
-O5	2.17 (2)	2.33(3)	2.37(2)
Cu1-O2	1.92(1)	1.90(2)	1.81(4)
-O3	1.93(2)	2.07 (4)	2.08(3)
-O4	2.75(2)	2.72(3)	2.89(3)
-O4	1.92(2)	1.99 (1)	2.17(4)
-O5	2.01(2)	2.04 (5)	2.13(4)
Cu2-O1	2.05(1)	2.09(2)	2.12(3)
-O3	1.98(2)	2.01(5)	1.97(4)
-O4	2.03(2)	2.08(10)	1.82(4)
-O4	2.93(2)	2.81(8)	2.76(3)
-O5	1.95(1)	1.85(4)	1.77 (3)
Cu2-O3-Cu1	92.4(8)	88.7 (8)	89.5 (8)
Cu2-O5-Cu1	91.1 (7)	93.0 (8)	95.5 (6)

Similar conclusions can be drawn from the measurements of field dependence of magnetization recorded at 2 K temperature, shown in Fig. 5.6. It can be seen that pure $Y_2Cu_2O_5$ sample displays typical metamagnetic behavior with two observable field-induced transitions at approximately 2 T and 4 T which agrees with the literature data [1-3]. However, both diluted samples show departure from this behavior especially for the lower fields where M(H) dependence resembles behavior typical of paramagnetic-like system. At higher fields this behavior changes to a linear M vs. H dependence with the slight upturn at about 4 T that indicates the occurrence of metamagnetic transition at this field. It can be concluded that M(H) behavior of diluted samples S5 and S15 is dominated by paramagnetic contribution at lower fields that disables detection of magnetically ordered phase until higher fields value of above 4 T where ordered AF phase with metamagnetic properties becomes visible.

References

1. S.W. Cheong, J.D. Thompson, Z. Fisk, K.A. Kubat-Martin, E. Garcia, Phys. Rev. B 38 (1988) 7013-7015.
2. Y. Matsuoka,Y. Nishimura, S. Mitsudo, H. Nojiri, H. Komatsu, M. Motokawa, K. Kakurai, K Nakajima, Y. Karasawa, N. Niimura, J. Magn. Magn. Mater. 177-181 (1998) 729-730.
3. M. Motokawa, K. Kita, H. Shibazaki, H. Ohta, W. J. Jang, M. Hasegawa, H. Takei, Physica B 211 (1995) 165-167.
4. U. Adem, G. Nenert, Arramel, N. Mufti, G.R. Blake, and T.T.M. Palstra, Eur. Phys. J. B 71 (2009) 393-399.
5. R.D. Adams, J.A. Estrada, T. Datta, J. Supercond. 5 (1) (1992) 33–38.
6. R. Famery, F. Queyroux, Mater. Res. Bull. 24 (1989) 275–281.
7. H. Fjellvag, P. Karen and A. Kjekshus, Acta Chem. Scand. A 42 (1988) 144-147.
8. J. L. Garcia- Munoz and J. Rodrguez-Carvajal, J. Solid State Chem. 115 (1995) 324-331.
9. B. L. Ramakrishna, E. W. Ong and Z.Iqbal, Solid Stale Communication 68 (1988) 775-779.

10. Qiang Su, Xueqiang Cao and Hongyan Wang, J. Mater. Chem. 4 (1994) 417-420.
11. R. Horyn, J. Klamut, M. Wolcyrz, A. Wojakowski, A. J. Zaleski, J.Magn. Magn. Mater, 140-144 (1995) 1575-1576.
12. Typek and N. Guskos, Rev. Adv. Mater. Sci. 12 (2006) 106-111.
13. J. Typek, Phys. Stat. Sol. (b) 244 (2007) 1102-1108.
14. J. Typek, J. Kostrzewa, N. Guskos, Mat. Sci (Poland) 23 (2005) 929-938.
15. Qiang Su, Xueqiang Cao and Hongyan Wang, J. Solid State Chem. 111 (1994) 310-314.
16. J. Typek and N. Guskos, Mat. Sci, (Poland) 24 (2006) 901-912.
17. J. Typek, Journal of Alloys and Compounds 440 (2007) 26-29.
18. Z. Gebrel. J. Blanusa, V. Spasojevic, V. Kusigerki, A. Mrakovic, A. Alqat, M. Perovic, Journal of Alloys and Compounds 568 (2013) 55-59.
19. H.M. Rietveld, J. Appl. Crystallogr. 2 (1969) 65.
20. Juan Rodríguez-Carvajal, Physica B: Condensed Matter, 192 (1993) 55-69.
21. B. Goodenough, Magnetism and Chemical Bond, Krieger, New York 1976.
22. R. Horyn, J. Klamut, M.Wolcyrz. A. Wojakowski, A.J. Zaleski, Physica B. 205(1995) 51-58.
23. R. Troc, Z. Bukovski, R. Horyn, J. Klamut, Phys. Lett. A 125 (1987) 222–224.
24. I. V. Paukov, M. N. Popova, J. Klamut, Phys. Lett. A 189 (1994) 103-108.
25. J. C. Bonner and M. E. Fisher, Phys. Rev. 135 (1964) 640-658.
26. M. Winkelmann and H. A. Graf, Phys. Rev. B 49 (1994) 310-317.

6. Structure and magnetic properties of nanoparticle $YMnO_3$ obtained by SHS method

So far three yttrium-manganese oxides have been reported: $YMnO_3$, YMn_2O_5 and $Y_2Mn_2O_7$. As discussed in chapter 2, hexagonal $YMnO_3$ represents material of choice regarding investigations of multiferroic phenomenon, due to its unusual strong coupling between magnetic and dielectric ordering parameters. However, the particle size effects on its multiferroic properties became subject of interest only recently and are still mainly unexplored, requiring more experimental data.

The exact phase equilibrium in Mn-Y-O system until now has not been well investigated [1]. Of the two structure modifications, a hexagonal non-perovskite phase (h-$YMnO_3$) and an orthorhombic perovskite phase (o-$YMnO_3$), the h-$YMnO_3$ is found to be the stable one at normal atmospheric conditions and is known to be a so called ferroelectromagnetic material. Bertaut et al. discovered that it is both antiferromagnetic and ferroelectric [2].

Unlike h-$YMnO_3$, the o-$YMnO_3$ phase is metastable under normal synthesizing conditions, and it exhibits completely different physical behavior, typical of other perovskite manganites. This phase seems to be stabilized by presence of defects or additional strain introduced into the crystal lattice, which makes it possible to synthesize at low-temperature (soft chemistry) and high-pressure [2, 3, 4, 6], or via epitaxial thin film growth techniques [5]. It was demonstrated that upon annealing under high hydrostatic pressure, h-$YMnO_3$ can be converted to o-$YMnO_3$ [3]. For the orthorhombic phase, ferroelectricity also exists, but it is induced by long-range magnetic order that breaks the symmetry of the crystal and creates a polar axis. Neutron diffraction data and magnetization measurements have shown that o-$YMnO_3$ becomes magnetically ordered below T_N = 42K [7].

Considering h-YMnO3 preparation, $Y_2Mn_2O_7$ represents the less important Y–Mn–O compound since it is very unstable under normal synthesizing condition. Fujinaka et al. reported that $Y_2Mn_2O_7$ can be prepared at 1273-1373 K and high oxygen pressure of 3-4 GPa [8]. Shimakawa et al. [9] synthesized $Y_2Mn_2O_7$ by solid state reaction,

at 1273–1573 K and 40 MPa oxygen pressure (a mixture of 20% oxygen and 80% argon) in a hot-isostatic-press apparatus. Subramanian et al. [10] reported that $Y_2Mn_2O_7$ does not decompose in air up to 1073 K. However, after heating at 1173 K, it transforms into $YMnO_3$.

Another possible Y-Mn-O compound, YMn_2O_5, crystallizes in an orthorhombic structure with the space group *Pbam*, and shows antiferromagnetic phase transition at T_N = 45K [11]. In contrast to $Y_2Mn_2O_7$, this oxide is much more significant regarding $YMnO_3$ synthesis since, just like $YMnO_3$, it is stable under normal atmospheric conditions. Moreover, in presence of oxygen it is even more stable than $YMnO_3$ at elevated temperature [1, 12]. This compound is formed from Y_2O_3 and Mn_2O_3 mixture above 1073 K [1, 6]. At the same temperature $YMnO_3$ decomposes in air into YMn_2O_5 and Y_2O_3 [1]:

$$4YMnO_3 + 1/2O_2 = 2YMn_2O_5 + Y_2O_3$$

YMn_2O_5 cannot be found as contaminant in $YMnO_3$ preparation because it disintegrates below 1073 K, however, in that process it decomposes into the most frequently found Y_2O_3 impurity and, most probably, into Mn_2O_3 [1, 13, 14]. According to Fu et al. [15], YMn_2O_5 is thermally stable between 1073 K and 1373 K, but when heated at 1473 K in air, YMn_2O_5 decomposes again to give $YMnO_3$ as follows:

$$2YMn_2O_5 = 2YMnO_3 + Mn_2O_3 + 1/2O_2$$

Thus presence of oxygen can have double adverse effect in $YMnO_3$ preparation, considering that classical sintering procedure includes crossing of both forming and decomposing temperature for YMn_2O_5. The above reactions represent the most probable cause for a persistence of unreacted Y_2O_3 and corresponding manganese oxides, which are often found during long, high-temperature sintering in air [15, 16]. Our own attempts to synthesize pure h-$YMnO_3$ by sintering in air [17] were also unsuccessful, since detailed XRD measurements have confirmed the traces of Y_2O_3 phase that persist even after 100 hours of heating at 1300 ^{0}C and frequent powder re-grinding. As reported in [17], pure bulk h-$YMnO_3$ was possible to obtain only in the absence of oxygen, and even in that case, the hexagonal sample (completely free from the orthorhombic phase) could not be synthesized at temperature lower than 1300 ^{0}C. In the same study, we have shown that, in absence of

oxygen, metastable o-$YMnO_3$ phase is first to appear from amorphous precursor at temperature below 700 ^{0}C and remains as the major phase up to 900 °C, while a mixture of h-$YMnO_3$ and o-$YMnO_3$ phase (with hexagonal as a major phase) occurs at 900 ^{0}C–1000 ^{0}C. By increasing the temperature, the amount of orthorhombic phase decreases, but only at

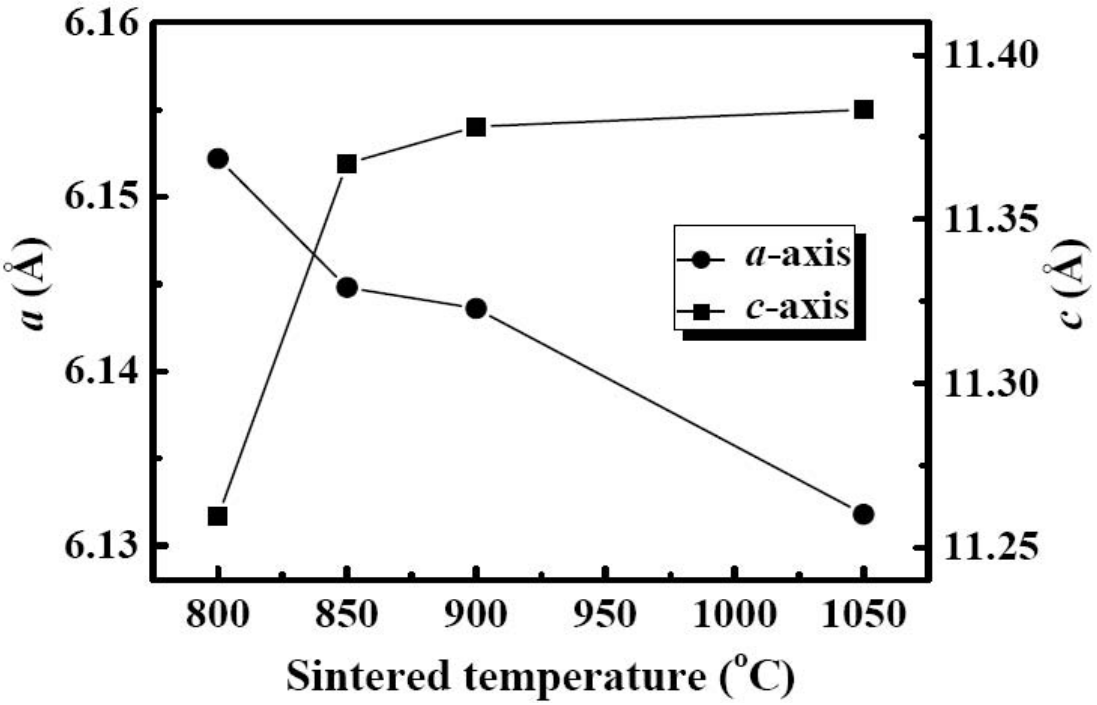

Figure 6.1: The evolution of lattice parameters for nanoparticle h-$YMnO_3$ annealed at different temperatures, taken from [21].

1300 ^{0}C pure and well crystallized h-$YMnO_3$ was finally obtained [17].

Above results regarding bulk material preparation illustrate the necessity of using high temperature (min. 1300 °C) over several hours of sintering. This is highly unacceptable in the usual nanoparticle preparation (low temperature, short reaction time). In fact, the conditions applied in soft chemistry as a standard practice in nanoparticle synthesis are much more favorable for the formation of orthorhombic phase. This certainly creates a strong challenge in the synthesis of nanoparticle hexagonal $YMnO_3$, so that it is not surprising at all that there were no attempts in preparation of nanoparticle h-$YMnO_3$ until two years ago (since 2011), when few reports on this subject appeared [18, 19, 20].

Nanoparticle h-$YMnO_3$ has been synthesized by S.F.Wang et al. in 2011, using modified polyacrylamide gel route, which gave $YMnO_3$ nanoparticles with different average sizes ranging from 85 to 45 nm. XRD analysis indicates that the as-prepared samples crystallize fully as $YMnO_3$, but besides major hexagonal phase small amount of minor orthorhombic phase was found [18]. In 2011, Bergum et al [19] reported about preparation of nanocrystalline $YMnO_3$ by wet chemical synthesis routes to obtain crystalline powder with particle sizes ranging from 20 nm to bulk material. They have shown that reducing synthesis conditions suppress formation of metastable orthorhombic phase, favoring pure h-$YMnO_3$. Pure h-$YMnO_3$ was obtained below 1000 ^{0}C and only with absence of nitrate reactants [19].

Also in 2011, another work on nanoparticle $YMnO_3$ synthesis was reported by Tai Chun et al. [21], who claimed the preparation of pure hexagonal $YMnO_3$ nanoparticles by a modified Pechini method. They have studied the grain size dependency of magnetic and electrical properties of obtained material, and found that samples annealed at 800°C, 850°C, 900°C, and 1050°C (corresponding to 25, 45, 95, and 200 nm) are all of hexagonal structure with different lattice parameters as shown in Figure 6.3. The magnetic characterization indicates that with increasing grain size, the anitferromagnetic transition temperature increases from 52 K to 74 K, without any indications of orthorhombic phase presence. However, the results obtained in this reference are in sharp contrast to all other reports, including our own experience with $YMnO_3$ synthesis.

In this work we present our results on the preparation of nanoparticle h-$YMnO_3$ via SHS combustion method. Considering the mentioned difficulties in the preparation of bulk and nanoparticle h-$YMnO_3$, there is a reasonable expectation that combustion routes may represent a perspective approach to this subject since they offer possibilities of generating high temperature reaction (necessary for h-$YMnO_3$ stabilization), combined with a very short reaction time (to prevent crystal growth). Regarding SHS and combustion methods in general, recent research activities worldwide has focused on usage of new organic fuels and oxidizers for the solution combustion synthesis in order to gain better control over the combustion process and particle size. One of the recent innovations in that direction is a modification of SHS process in which fuel and oxidizer are introduced independently into

the mixture of reacting components. It was already shown that, by using this approach, it was possible to obtain highly crystalline 20 nm $La_{0.7}Ca_{0.3}MnO_3$ nanoparticles in a single step process [22], or as we have demonstrated, to obtain $Y_2Cu_2O_5$ in appreciably shorter time than by usual solid state sintering route [23].

6.1 Experimental

Unlike the previous examples presented in chapters 4 and 5 about pure and substituted $Y_2Cu_2O_5$, the combustion route used for nanoparticle synthesis has to be a single step process in which the final material is completely formed both chemically and structurally. Thus, the nanoparticle samples of $YMnO_3$ were synthesized in a similar manner by a modified SHS method as described in previous chapters, but without subsequent sintering. In this case we have used nitrates as metal precursors: yttrium-nitrate $Y(NO_3)_3$ and manganese-nitrate $Mn(NO_3)_3$ in stoichiometric proportions (1:1 molar ratio) necessary to provide the future reaction between their corresponding oxides :

$Y_2O_3+Mn_2O_3 \rightarrow 2YMnO_3$

A redox mixture composed of sugar and potassium nitrate is again added to the nitrate solution, in the same manner as for the preparation of $Y_2Cu_2O_5$. However, since the temperature and the oxygen presence are proved to be extremely important in case of $YMnO_3$, we have conducted two different SHS reactions. In one, the molar ratio between sugar and potassium nitrate in the redox mixture ($C_6H_{12}O_6$: KNO_3) was kept at the standard 1:2 ratio. In another one, this ratio was shifted towards sugar excess (ratio between sugar and KNO_3 was adjusted to 1.3:2), with the main idea to reduce the reaction temperature, and at the same time to make conditions more reductive due to the lack of oxygen, thus preventing formation of orthorhombic structure. In both cases, the solution of nitrates and redox mixture was dried at 120°C to form a gel. The dried residue was formed into a shape while warm, cooled down and ignited locally at one point, (in air) by means of an external thermal source (i.e. a match or a lighter). After the ignited burning reaction has terminated at the other end of the shape the combustion product in the form of a dark blue-black, fluffy powder was washed several times with distilled water to remove traces of

K_2CO_3 and afterwards dried at 70 º C. The two obtained samples are denoted as S1 and S2. The part of S1 sample (due to the reasons explained later) was additionally annealed at 1000 °C for 3 h in an N_2 flow, and the resulting sample was denoted as S_{1000}.

All three samples were characterized by powder x-ray diffraction (XRD), and magnetic measurements. Powder XRD measurement at room temperature was carried out on the Phillips PW1050 diffractometer with Cu Kα radiation described in Chapter 3, as a standard technique for characterization of nanoparticles by X-ray diffraction, which is used both to identify the crystalline phases in a sample and to estimate the particle size.

6.2 Result and discussion

6.2.1 X-ray diffraction analysis

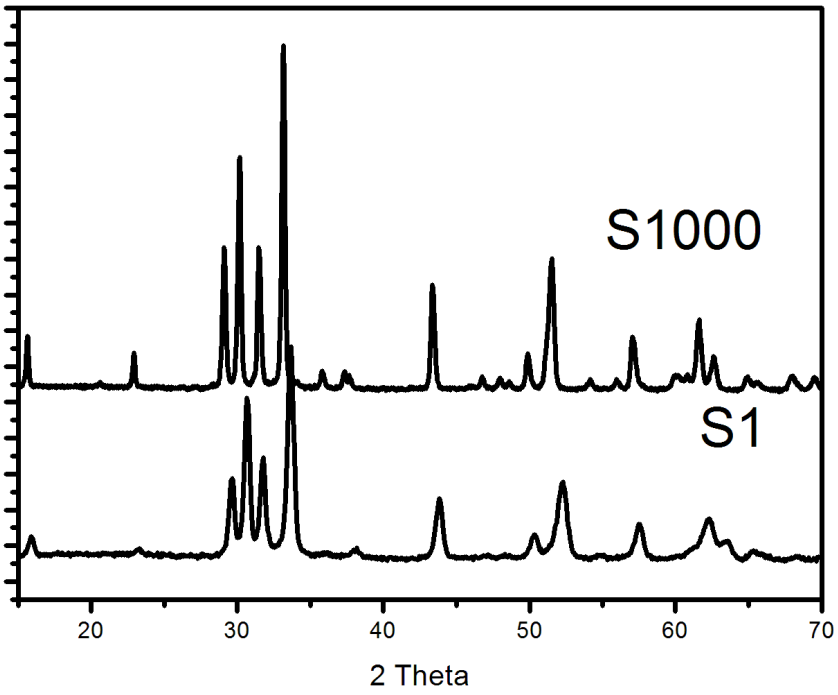

Figure 6.2. XRD patterns for S_1 (without heating), S_{1000} (after heatting at 1000 °C for 3 hours)

Due to the specifics of nanoparticle systems comprising structure and microstructure

properties, structural parameters in this case were refined in two ways: by Le Bail (profile matching mode) method [25] and by the Rietveld full-profile analysis with the application of the FULLPROF software package.

The profile matching is also a least square procedure, but it differs from Rietveld method in that it does not take into account atomic content (asymmetric unit) to calculate

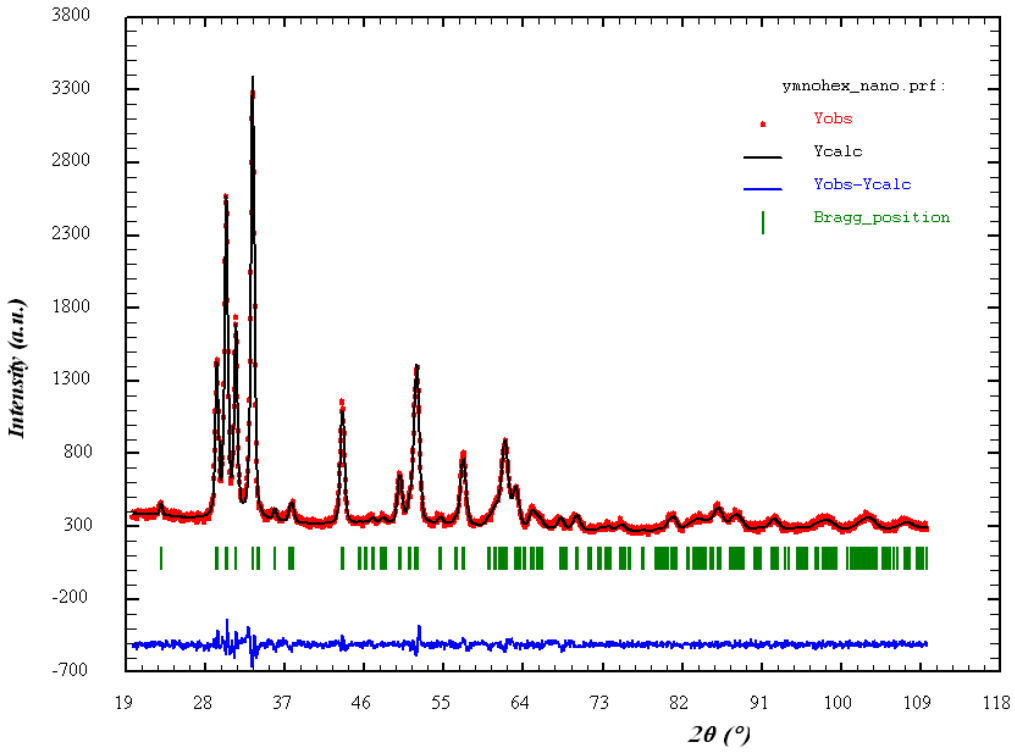

Figure 6.3: The Le Bail refinement of the diffraction pattern taken from S_1. The dots and the line represent the observed and calculated patterns, respectively. Vertical bars indicate the peak positions corresponding to the h-$YMnO_3$ structure, while the bottom line represents the difference between the observed and calculated patterns.

integral intensities. In general, this approach is not convenient for structure refinement since it gives only the geometry of the lattice without possibility to extract atomic coordinates. It is also less stable refinement sensitive to excessive peak overlapping. However, profile matching is considerably faster and useful for solving unknown structures from powder XRD data, but also for characterization of nanoparticles microstructure

(particle size and microstrain), since microstructure parameters depend entirely on peaks profile and are in no way related to atomic content.

An inspection of diffraction patterns and subsequent structure refinement revealed that S_1 can be regarded as a single phase sample, while in the other two samples both structure phases were found. For this reason, the as–prepared sample S_1 was refined by Le Bail method, while for S_2 and S_{1000} we have used Rietveld method in order to determine the phase content accurately.

The recorded XRD pattern of two $YMnO_3$ samples, S_1 (samples without additional heat treatment) and S_{1000} (S_1 annieled at 1000 ^{0}C for 3h) are shown in Figure 6.2. Apparently, the two sets of diffraction data correspond to hexagonal phase and seem to differ only in peak width and intensity, with the S_1 sample showing evidently larger peak broadening due to the smaller crystallite size. Subsequent refinements, however, have

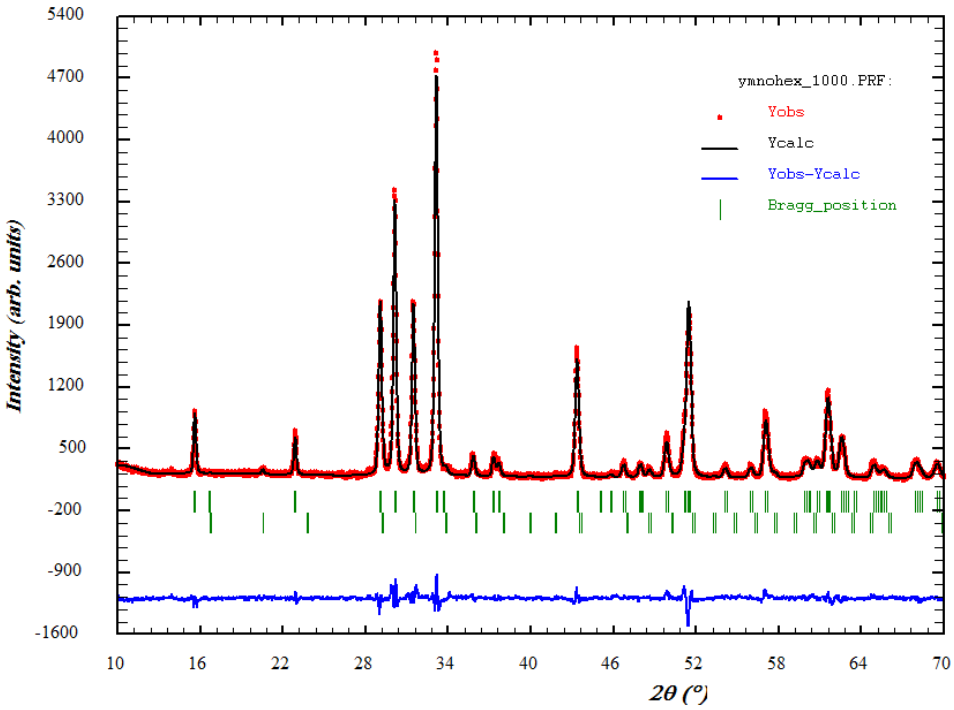

Figure 6.4: The Rietveld refinement of the diffraction pattern taken from S_{1000}. Vertical bars indicate peak positions corresponding to the h–$YMnO_3$ and o–$YMnO_3$.

shown that S_{1000} actually contains small amount of orthorhombic phase (detectable by XRD), and moreover, magnetic measurements (described in the next section) revealed the persistence of a small amount of orthorhombic $YMnO_3$ in *all* samples, including S_1.

The refinement resulted in that S_{1000} has about (91.67±0.52) weight % of the h-$YMnO_3$ phase and only (8.33±0.03) weight % of the o-$YMnO_3$ phase (Figure 6.4). S_1 was refined as single phase sample (Figure 6.3) in which the presence of orthorhombic phase was found to be below the detection limits (in case of XRD analysis, this is usually around 1%). The values of refined cell parameters obtained for S_1 and S_{1000} samples are listed in Table 6.1. It is interesting to note the decrease of cell parameters along ***a***–axis with annealing, which is in accordance with results reported in [21], but almost without any change along ***c***–axis. The average particle size was found to be 20 nm for S_1, very similar to particle size reported in our previous work about $LaMnO_3$ nanoparticles obtained by the

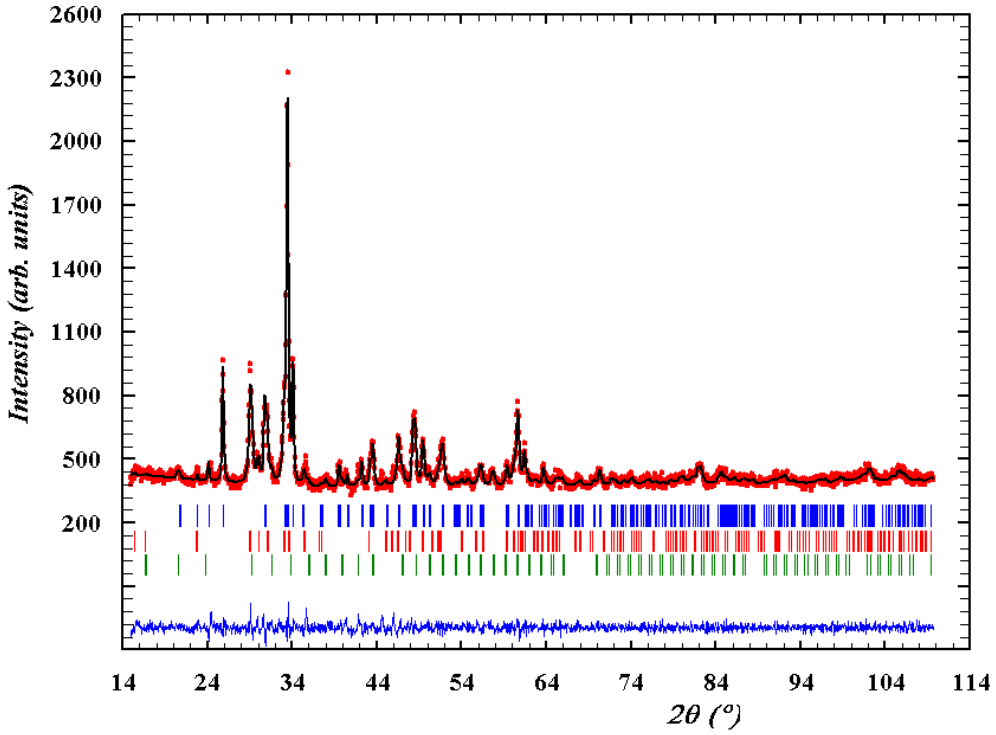

Figure 6.5: The Rietveld refinement of the diffraction pattern taken from S_2. Vertical bars indicate peak positions corresponding to three phases: the h-$YMnO_3$, o-YMnO3, and Y_2O_3.

same method [22].

While the results obtained for S_1 and S_{1000} fell in range of our expectations, for those related to S_2 sample holds completely opposite. The XRD refinement of S_2 is shown in Figure 6.5, and the refinement confirmed that the orthorhombic $YMnO_3$ is synthesized as the major phase with space group Pnma, together with a minor amount of hexagonal $YMnO_3$ phase and traces of Y_2O_3 contaminant. The analysis shows that S_2 has about (80.6±0.5) weight % of the o-YMnO3 phase, only (14.3±0.01) weight % of the h-$YMnO_3$ phase and (5.7±0.6) weight % of excess Y_2O_3. Such result calls into question our previous assumptions on oxygen presence or absence as a primary factor in phase stability for $YMnO_3$. On the contrary, based on this example one can conclude that lower reaction temperature and rate could be responsible for the preferential growth of orthorhombic phase, most probably through higher concentration of defects and strain within the surface area.

Table 6.1: Cell parameters and volumes obtained by Rietveld refinement of XRD data collected at room temperature, space group P_63cm

		S_1	S_{1000}
Cell parameters (Å)	***a***	6.1519(4)	6.0951(3)
	b	6.1519(4)	6.0951(3)
	c	11.3779(9)	11.3785(5)
Cell volume ($Å^3$)		372.92(3)	366.09(3)
Rp (%)		7.7	7.51
Rwp (%)		11	5.04

6.2.2 Magnetic measurements

Unlike structure data for h–$YMnO_3$, magnetic properties reported throughout the available literature data are not consistent. The magnetic impurity phases that can be found in h–$YMnO_3$ are Mn_3O_4 (orders FM with $T_C \approx 42$ K [24]), YMn_2O_5 (ordering at $T_C \approx 45$ K [11]), and orthorhombic $YMnO_3$ that shows AF ordering below $T_N = 41$ K [7]. Thus in order to monitor the phase evolution during the synthesis process as well as phase purity of

the obtained hexagonal $YMnO_3$ we have conducted magnetic measurements on the SQUID-based magnetometer in the temperature region 2 K-300 K that encompasses critical temperatures of all above listed magnetic phases.

The magnetic properties of the $YMnO_3$ samples and their correlation with the structure are investigated by measuring magnetization as a function of temperature *M(T)*. The temperature dependent magnetization measurements were carried out in magnetic field of 100 Oe under the conditions of zero-field-cooled (ZFC) and field-cooled-regime (FC).

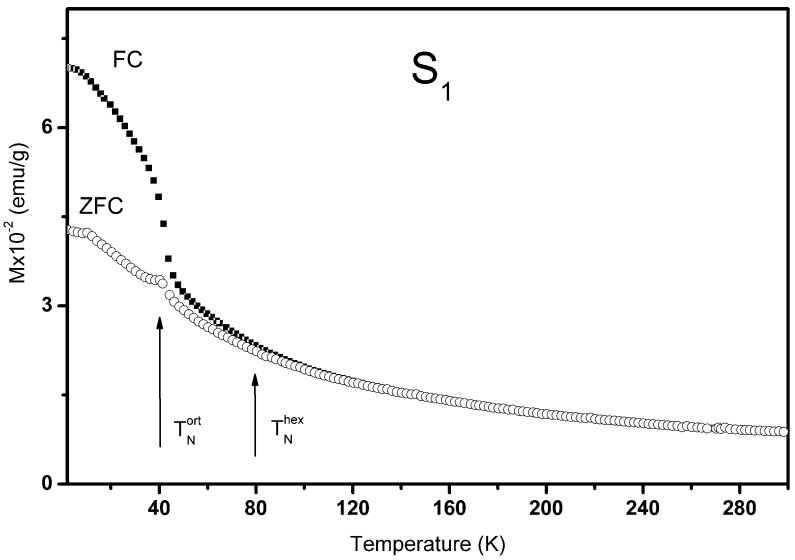

Figure 6.6: Temperature dependence of ZFC and FC magnetization for S_1 at magnetic field 100 Oe

Figure 6.6, Figure 6.7, and Figure 6.8 display the temperature dependence of magnetization for S_1, S_{1000}, and S_2 samples respectively. In these three cases, different dependences are obtained regarding curve characteristics and bifurcation between ZFC and FC branches. Nevertheless, some features are common, like the existence of peaks in ZFC magnetization at ≈ 42 K and 15 K, and significant difference between ZFC and FC magnetization that exists below 42 K.

Bifurcation among ZFC and FC magnetization is expected and takes place also in case of bulk material below T_N [17]. This is because h–$YMnO_3$ is known as "frustrated" antiferromagnetic, meaning that triangular geometrical arrangement of Mn ions does not

allow the complete AF ordering. Simply speaking, a system made of three magnetic ions placed in a triangle corners can not have linear AF ordering since one ion always stays

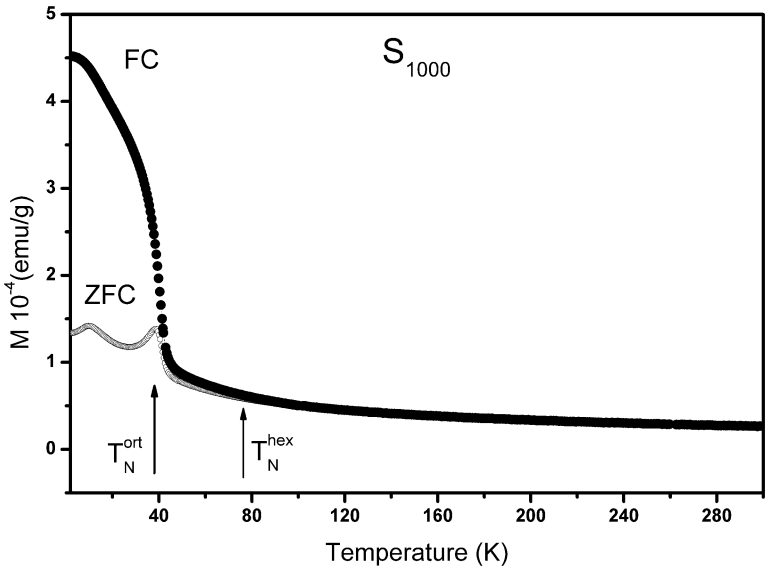

Figure 6.7: Temperature dependence of ZFC and FC magnetization for S_{1000} at magnetic field 100 Oe

"frustrated", which is the situation similar to what was commonly found in canonical spin–glasses. Thus, there is always a component of Mn^{3+} magnetic moment that is not completely correlated with the rest of AF ordered structure, and is therefore sensitive to the presence or absence of external magnetic field. This makes FC larger than ZFC magnetization below T_N and typically without saturation at decreasing temperature.

What is not typical of h–$YMnO_3$ behavior is the existence of two mentioned low–temperature transitions in ZFC branch (present in all samples). The first one that appears at 8–15 K is broad and paired with almost stagnant (saturated) FC dependence, which is in accordance with spin–glass like behavior. This kind of transition is frequently found in nanoparticle systems and originates from defective surface region of a particle (shell region), i.e. it resembles an influence of surface effects. The second transition that takes place at 42 K can be ascribed to the presence of either orthorhombic $YMnO_3$ phase or YMn_2O_5, or both. Our experience with gradual $YMnO_3$ crystallization starting from amorphous substrate [17] has shown that o–$YMnO_3$ is the most probable contaminant, and

in the case of S_{1000} and S_2 samples this is confirmed by XRD analysis. On the other hand, S_1 sample represents an interesting example in which XRD measurements can not be applied as a reliable tool for detection of small amounts of o–$YMnO_3$, due to the presence of excessive peak broadening. This brings magnetic characterization as a primary tool for nanoparticle $YMnO_3$ phase analysis, since even tiny amounts of any magnetic impurity phase may dominate the magnetization of an antiferromagnetic material, and so it can be used to detect the presence of (magnetic) impurity phase in amounts that are far below the resolution of XRD method.

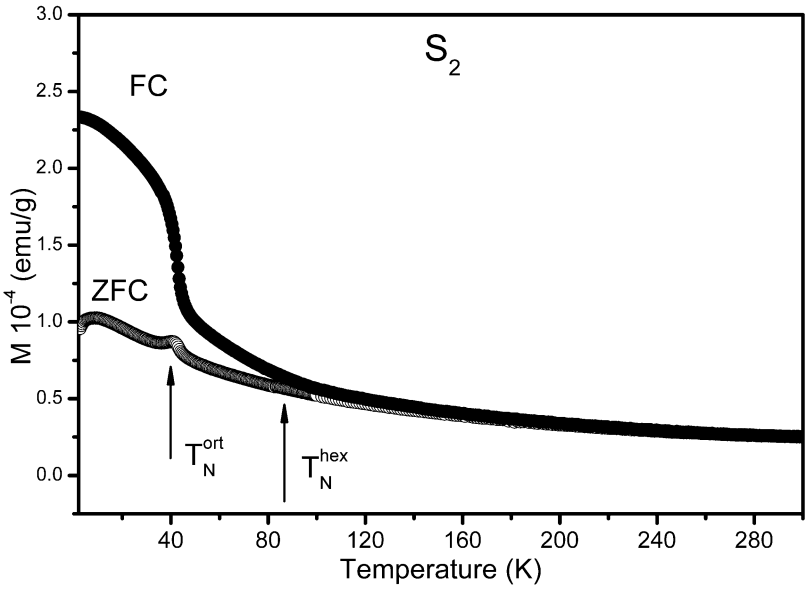

Figure 6.8: Temperature dependence of ZFC and FC magnetization for S2 at magnetic field 100 Oe

Though multiphase in composition, S_2 sample shows the most complex magnetization behavior that deserves further attention. The ZFC and FC magnetization branches for S_2 sample in the applied magnetic field of 100 Oe are depicted in Figure 6.8. As it can be seen, typical AFM to paramagnetic (PM) phase transition appears to take place at about 90 K where the bifurcation between ZFC and FC curves becomes notable. This is already above phase transition temperature reported for h–$YMnO_3$ (80 K), but the detailed insight into Figure 6.8 reveals that ZFC and FC curves actually start to completely overlap (within the resolution limits) only above 130 K. This proves that Mn ions are somehow

magnetically correlated in S_2 even at these relatively high temperatures, which are far above transition points of any common Mn–O or Y–Mn–O compound that can possibly be found as contaminant in $YMnO_3$.

Such result clearly demonstrates the significant role that surface effects can play in case of $YMnO_3$ nanoparticles. This one is particularly interesting since it points to the existence of a considerably strong interaction that would be rather expected in manganites with mixed valence states – the double exchange, which assumes the existence of mixed Mn^{3+}/Mn^{4+} state. Without possibility of Y substitution with divalent alkaline–earth elements (Ca^{2+}, Ba^{2+}), it is reasonable to assume that non–stoichiometric manganite formation of the $Y_{1-\delta}MnO_3$ type may occur (Y^{3+} vacancies), which is in accordance with XRD analysis showing 6% of excess Y_2O_3 without detection of corresponding excess of Mn–oxides (by either XRD or magnetic measurements).

References

1. Ming Chen, Bengt Hallstedt, Ludwig J. Gauckler, Journal of Alloys and Compounds, 393 (2005) 114-121.
2. S. C Abrahams, Acta cryst. B, 57 (2001) 485-490.
3. A. Waintal, J. Chenavas, C.R. Acad. Sci. Paris Ser. B, 264 (1967) 168–170.
4. H.W. Brinks, H. Fjellvag, A. Kjekshus, J. Solid State Chem., 129 (1997) 334–340.
5. P.A.Salvador, T.-D. Doan, B. Mercey, B. Raveau, Chem. Mater., 10 (1998) 2592–2595.
6. S.A. Prokudina, Y.S. Rubinchik, M.M. Pavlyuchenko, Inorg. Mater., 12 (1976) 598–603.
7. A. Munoz, J.A. Alonso, M.T. Casais, M.J. Martinez-Lope, J.L. Martinez, M.T. Fernandez-Diaz, J. Phys.: Condensed Matter, 14 (2002) 3285–3294.
8. H. Fujinaka, N. Kinomura, M. Koizumi, Y. Miyamoto, S. Kume, Mater. Res. Bull., 14 (1979) 1133–1137.
9. Y.Shimakawa, Y.Kubo, N. Hamda, J. D.Jorgernsen, Z.Hu, S. Short, M. Nohara, H. Takagi, Physs. Rev. B, 59 (1999) 1249-1254.

10. M.A. Subramanian, C.C. Torardi, D.C. Johnson, J. Pannetier, A.W. Sleight, J. Solid State Chem., 72 (1988) 24–30.
11. Kobayashi S.Osawa T, Kimura H, Noda Y, Kagomiya I and Kohn K Japan. J. Phys. Soc., 73 (2004) 1593.
12. Sheng-Hsu Liu, Jung-Chun-Anderw Huang, Xiaoding Qi, Wei-Jui, Yu-Jhan Siao, AIP Advances, 1 (2011) 173.
13. Hirohisa Satoh, Jun ichi Iwasaki, Kouji Kawase, Naoki Kamegashira, Journal of Alloys and Compounds, 268 (1998) 42-46.
14. M. Janoschek, B Roessli, L Keller, S N Gvasaliya, K Conder and E Pomjakushina, J. Phys: Condensed Matter, 17 (2005) 425-430.
15. B. Fu, Wayne Huebner, Mladen F, Trubelja and Vladimir S Stubican, J.Mater. Res., 9 (1994) 2645-2653.
16. W. R. Chen, F. C. Zhang, J. Miao, B. Xu, X.L. Dong, L.X. Cao, X. G. Qiu, B. R. Zhao, Pengcheng Dai, Applied Physics Letters, 87 (2005) 042508.
17. Aboalgasim Algat, Zohra Gebrel, Vladan Kusigerski, Vojislav Spasojevic, Marian Mihalik, Matus Mihalik, Jovan Blanusa, Ceramics International, 39 (2013) 3183-3188.
18. S. F. wang, H. Yang, T. Xian, X. Q. Liu, Catalysis Communications, 12 (2011) 625-628.
19. Kristin Bergum, Hiroshi Okamato, Helmer Fjllvag, Tor Grande, Mari-Ann Einarsrud and Seerre M. Selbach, Dalton Trans., 40 (2011) p.7583.
20. M. F.Zhang, J. M. Liu, Z. G Liu, Appl. Phys. A, 79 (2004) 1753-1756.
21. Tai Chun Han, Wei Lun Hsu, Wei Da Lee, Nanoscale Res. Lett. , 6 (2011) p.201.
22. Ana Mrakovic, Jovan Blanusa, Darinka Primc, Marija Perovic, Zvonko Jaglicic, Vladan Kusigerski, Vojislav Spasojevic, Ceramics International, 39 (2013) 3771-3777.
23. Z. Gebrel. J. Blanusa, V. Spasojevic, V. Kusigerki, A. Mrakovic, A. Alqat, M. Perovic, Journal of Alloys and Compounds, 568 (2013) 55-59.
24. K. Dwight and N. Menyyuk, Physical Review, 119 (1960) 1470-1479.
25. A. Le Bail, Powder Diffraction, 20 (2005) 316-326.

7. Conclusions

In this work we have studied synthesis and magnetic properties of pure $Y_2Cu_2O_5$, the effect of substitution of Mg in $Y_2Cu_2O_5$ at Cu site, as well as the preparation and magnetic properties of fine particle $YMnO_3$.

A new approach to $Y_2Cu_2O_5$ preparation using combustion methods is introduced with considerable success. Polycrystalline samples of $Y_2Cu_2O_5$ (S1, S2 and S3) were sintered from precursors obtained by three preparation methods: thermal decomposition of metal nitrates (S1), the glycine-nitrate method (S2), and a modified SHS route (S3). From these precursors, final single phase specimens were obtained after 74 h, 31 h, and 12 h of sintering, respectively. In all cases, it was demonstrated that the single phase samples could be obtained in appreciably shorter sintering time than in the case of the standard ceramic sintering from the mechanically homogenized mixture of metallic oxides. The analysis of the crystal structure and magnetic properties of the obtained samples showed that the modified SHS procedure enables the most efficient synthesis route, regarding both sintering time (only 12 h) and crystal structure definition.

However, the most interesting findings (besides new synthesis methods) are related to detected thermal drift of Cu ions from their standard crystallographic positions. Detailed structure characterization revealed a different degree of Cu ions drift: 20% in S1, 10% in S2 and the absence of such displacement in S3. The comparative study of magnetic properties and crystal structure gives a strong indication that Cu displacement has to be regarded as an important parameter in for $Y_2Cu_2O_5$ since it significantly influences magnetic behavior below Néel temperature. Thus, being dependent on temperature and/or sintering time, the degree of Cu displacement represents an important factor that has to be considered in the course of every $Y_2Cu_2O_5$ preparation. Since it is connected with only slight deviations in the diffraction pattern, the existence of Cu disorder could be easily overseen, especially when the impurity content is treated as the only indicator of a successful synthesis. However, we have shown that Cu disorder leads to a noticeable diversity in the low-temperature magnetic behavior of the samples obtained by different preparation methods.

The effects of Mg substitution for Cu on the crystal structure and magnetic properties of $Y_2(Cu_{1-x}\ Mg_x)_2O_5$ solid solutions for x=0, 0.05 and 0.15 have been studied on the samples obtained by modified SHS method, which was the natural matter of choice considering the success achieved with the pure compound. The detailed analysis of the structure by the Rietveld method shows that Mg doping does not introduce significant changes in unit cell geometry or atomic positions. While this is expected due to almost identical Cu and Mg ionic radii, we were still able to detect minor distortions in the two main intradimmer superexchange paths which lead to decrease of ferromagnetic correlations with Mg substitution. This is confirmed by the decrease of both effective magnetic moments μ_{eff} and paramagnetic temperatures θ with Mg concentration in the high temperature region where all the samples obey Curie-Weiss law.

Impact of Cu substitution is found to be even more pronounced on low temperature magnetism, due to the breaking of infinite chains formed by Cu atoms in pure $Y_2Cu_2O_5$. The formation of finite size chains introduce strong low temperature paramagnetic contribution that perturbs ground state AFM ordering so that antiferromagnetic phase transitions below 12 K were observable but heavily blurred by paramagnetic signal. In addition, metamagnetic transition at 2 T that is typical of $Y_2Cu_2O_5$ has been dimmed while transition at 4 T was still detectable. In overall, results of our measurements give a strong indication that, although emergence of finite size Cu chains introduce paramagnetic contribution in the low temperature region, the 3D AFM ordering as well as metamagnetism in this material may still persists up to the 15% of the Cu dilution.

The second part of the thesis deals with possibilities to apply the SHS combustion in preparation of yttrium base multiferroic - hexagonal $YMnO_3$, and with the investigation of size reduction influence on its magnetic properties. In two different experimental setups, samples with particle size down to 20 nm were successfully obtained, but with the variable ratio found between hexagonal and orthorhombic phase content. Both approaches were designed to favor growth of hexagonal phase by precautions based on our previous empiric experiences, as well as on others from available literature data. However, the results of our experiments were somewhat surprising, with the significantly larger orthorhombic phase content found in the sample prepared in more reducing conditions (85%), contrary to the

expectations. Such an outcome refers to surface effects (degree of disorder, strain), as the additional factor regarding hexagonal phase growth, rather than oxidative or reductive reaction conditions alone. This is supported by magnetic measurements, which show unusually high bifurcation between ZFC and FC curves (at around 120 K), as well as low-temperature deviations typical of spin-glass like systems, usually located within particle surface.

Another important conclusion related to nanoparticle $YMnO_3$ synthesis is that XRD technique can not be used as an ultimate test of its phase content. Our experience with the sample prepared at higher reaction rate shows that in this case magnetic measurements are more sensitive tool, enabling us to detect even a very small amounts of orthorhombic phase that passed undetected by XRD analysis.

Прилог 1.

Изјава о ауторству

Потписани-а Zohra Ali Gebrel

број индекса D7/2008

Изјављујем

да је докторска дисертација под насловом

Синтеза и магнетне особине чистих и допираних итријумових манганита и купрата

- резултат сопственог истраживачког рада,
- да предложена дисертација у целини ни у деловима није била предложена за добијање било које дипломе према студијским програмима других високошколских установа,
- да су резултати коректно наведени и
- да нисам кршио/ла ауторска права и користио интелектуалну својину других лица.

Потпис докторанда

У Београду, 24.04.2013. године

Прилог 2.

Изјава о истоветности штампане и електронске верзије докторског рада

Име и презиме аутора _____Zohra Ali Gebrel_____

Број индекса____D7/2008_____

Студијски програм ____Докторске студије физике_____

Наслов рада Синтеза и магнетне особине чистих и допираних итријумових манганита и купрата

Ментор ___др Јован Блануша, виши научни сарадник _____

Потписани/а _____Zohra Ali Gebrel_____

Изјављујем да је штампана верзија мог докторског рада истоветна електронској верзији коју сам предао/ла за објављивање на порталу **Дигиталног репозиторијума Универзитета у Београду.**

Дозвољавам да се објаве моји лични подаци везани за добијање академског звања доктора наука, као што су име и презиме, година и место рођења и датум одбране рада.

Ови лични подаци могу се објавити на мрежним страницама дигиталне библиотеке, у електронском каталогу и у публикацијама Универзитета у Београду.

Потпис докторанда

У Београду, 24.04.2013. године

_____

Прилог 3.

Изјава о коришћењу

Овлашћујем Универзитетску библиотеку „Светозар Марковић“ да у Дигитални репозиторијум Универзитета у Београду унесе моју докторску дисертацију под насловом:

Синтеза и магнетне особине чистих и допираних итријумових манганита и купрата

која је моје ауторско дело.

Дисертацију са свим прилозима предао/ла сам у електронском формату погодном за трајно архивирање.

Моју докторску дисертацију похрањену у Дигитални репозиторијум Универзитета у Београду могу да користе сви који поштују одредбе садржане у одабраном типу лиценце Креативне заједнице (Creative Commons) за коју сам се одлучио/ла.

1. Ауторство

2. Ауторство - некомерцијално

3. Ауторство – некомерцијално – без прераде

4. Ауторство – некомерцијално – делити под истим условима

5. Ауторство – без прераде

6. Ауторство – делити под истим условима

(Молимо да заокружите само једну од шест понуђених лиценци, кратак опис лиценци дат је на полеђини листа).

Потпис докторанда

У Београду, 24.04.2013. године.

_____